

METHODOLOGY AND APPLICATION OF HIGH PERFORMANCE ELECTROSTATIC FIELD  
SIMULATION IN THE KATRIN EXPERIMENT

Thomas Corona

A dissertation submitted to the faculty at the University of North Carolina at Chapel Hill in partial fulfillment of the requirements for the degree of Doctor of Philosophy in the Department of Physics.

Chapel Hill  
2014

Approved by:  
John Wilkerson  
Joseph Formaggio  
Reyco Henning  
Arthur Champagne  
Fabian Heitsch

© 2014  
Thomas Corona  
ALL RIGHTS RESERVED

## ABSTRACT

Thomas Corona: Methodology and Application of High Performance Electrostatic Field Simulation in the KATRIN Experiment  
(Under the direction of John Wilkerson)

The Karlsruhe Tritium Neutrino (KATRIN) experiment is a tritium beta decay experiment designed to make a direct, model independent measurement of the electron neutrino mass. The experimental apparatus employs strong ( $\mathcal{O}[T]$ ) magnetostatic and ( $\mathcal{O}[10^5 \frac{V}{m}]$ ) electrostatic fields in regions of ultra high ( $\mathcal{O}[10^{-11}$  mbar]) vacuum in order to obtain precise measurements of the electron energy spectrum near the endpoint of tritium  $\beta$ -decay. The electrostatic fields in KATRIN are formed by multiscale electrode geometries, necessitating the development of high performance field simulation software. To this end, we present a Boundary Element Method (BEM) with analytic boundary integral terms in conjunction with the Robin Hood linear algebraic solver, a nonstationary successive subspace correction (SSC) method. We describe an implementation of these techniques for high performance computing environments in the software `KEMField`, along with the geometry modeling and discretization software `KGeoBag`. We detail the application of `KEMField` and `KGeoBag` to KATRIN's spectrometer and detector sections, and demonstrate its use in furthering several of KATRIN's scientific goals. Finally, we present the results of a measurement designed to probe the electrostatic profile of KATRIN's main spectrometer in comparison to simulated results.

### **Acknowledgements**

I am extremely grateful to Dr. John Wilkerson for his guidance and support, and for helping me rediscover a love for physics. I am indebted to my colleagues both at home and abroad for their insight and perspective on KATRIN, physics, and life. I am very lucky to have found Kellie Beicker and her love, optimism and emotional support. Finally, I would like to thank my family, whose unconditional love is a constant source of strength and whose continual encouragement has enabled me to finally achieve one of my life's goals.

## TABLE OF CONTENTS

<b>LIST OF TABLES</b> . . . . .	<b>x</b>
<b>LIST OF FIGURES</b> . . . . .	<b>xi</b>
<b>LIST OF ABBREVIATIONS AND SYMBOLS</b> . . . . .	<b>xvi</b>
<b>1 Introduction</b> . . . . .	<b>1</b>
1.1 Motivation for measurement of the neutrino mass . . . . .	1
1.1.1 Evidence for neutrino mass from flavor oscillation . . . . .	1
1.1.2 Significance of neutrino mass . . . . .	2
1.1.3 Current limits on the neutrino mass scale . . . . .	2
1.2 The KATRIN experiment . . . . .	3
1.2.1 Kinematics of tritium $\beta$ decay . . . . .	3
1.2.2 Overview of the apparatus . . . . .	5
1.2.3 Measurement of the electron energy spectrum . . . . .	5
1.2.4 KATRIN signal and background rates . . . . .	8
1.2.5 Impact on neutrino physics theory . . . . .	8
1.3 Electromagnetic simulations in the KATRIN experiment . . . . .	9
1.3.1 Boundary Element Method . . . . .	9
1.3.2 Robin Hood linear algebraic solver . . . . .	9
1.3.3 Electromagnetic simulation software . . . . .	9
1.3.4 Application to the KATRIN experiment . . . . .	9
1.3.5 Shifted analyzing surfaces . . . . .	10
1.4 Summary . . . . .	10
<b>2 Boundary Element Method</b> . . . . .	<b>11</b>

2.1	Introduction . . . . .	11
2.2	Conversion of the Laplace Equation to a Fredholm integral equation . . . . .	12
2.2.1	Description of the Laplace Equation . . . . .	12
2.2.2	Integral Statement for the Interior Equation . . . . .	12
2.2.3	Resolving Singularities with Limiting Behaviors . . . . .	13
2.2.4	Final form of the Interior Equation . . . . .	16
2.2.5	Extension to the Exterior Equation . . . . .	16
2.2.6	Composing a Global Solution . . . . .	17
2.2.7	Application of Boundary Conditions . . . . .	18
2.2.8	Extension to Multiple Regions and Disjoint Boundaries . . . . .	19
2.3	Discretization of Fredholm Integrals for Numeric Computation . . . . .	20
2.3.1	Dirichlet Boundaries . . . . .	20
2.3.2	Neumann Boundaries . . . . .	23
2.4	Application of the Boundary Element Method to Laplace Integral Equations . . . . .	24
2.5	Conclusion . . . . .	25
<b>3</b>	<b>Robin Hood Iterative Linear Algebraic Solver . . . . .</b>	<b>26</b>
3.1	Introduction . . . . .	26
3.2	Iterative Methods . . . . .	26
3.3	Stationary Iterative Methods . . . . .	27
3.3.1	Jacobi Method . . . . .	27
3.3.2	Gauss-Seidel Method . . . . .	28
3.4	Nonstationary Methods . . . . .	28
3.5	Reinterpretation of the Gauss-Seidel Method . . . . .	29
3.6	Generalization of the Gauss-Seidel method to a Successive Subspace Correction Method . . . . .	30
3.7	Robin Hood method . . . . .	31
3.8	Comparison of Robin Hood to Krylov Methods . . . . .	33
3.9	Comparison of Matrix Solving Methods applied to the Spherical Capacitor . . . . .	34

3.10	Conclusion . . . . .	35
<b>4</b>	<b>Simulation Software . . . . .</b>	<b>40</b>
4.1	KEMFIELD: a Boundary Element Method implementation in C++ . . . . .	40
4.1.1	Surfaces . . . . .	40
4.1.2	Boundary Integrals . . . . .	41
4.1.3	Linear Algebra . . . . .	44
4.1.4	Serialization . . . . .	45
4.1.5	Field Solvers . . . . .	46
4.1.6	External Fields . . . . .	46
4.1.7	Plugins . . . . .	46
4.1.8	Validation . . . . .	47
4.2	KGEOBAG: C++ geometry modeling software . . . . .	52
4.2.1	Motivation . . . . .	52
4.2.2	Overview . . . . .	52
4.3	Conclusion . . . . .	53
<b>5</b>	<b>Development and Application of Simulation Software for the KATRIN Experiment . .</b>	<b>54</b>
5.1	Introduction . . . . .	54
5.2	KATRIN detector region . . . . .	54
5.2.1	Overview of Electromagnetic Components . . . . .	54
5.2.2	Electrostatic & Magnetostatic Simulation . . . . .	56
5.2.3	Penning Trap Search . . . . .	56
5.3	KATRIN main spectrometer . . . . .	62
5.3.1	Overview of Electromagnetic Components . . . . .	62
5.3.2	Electrostatic & Magnetostatic Simulation . . . . .	65
5.3.3	Electrical Short Circuit Studies . . . . .	67
5.3.4	Vessel Deformation Studies . . . . .	73

5.4	Conclusion . . . . .	78
<b>6</b>	<b>Transmission Function Measurements in the KATRIN Main Spectrometer with Shifted Analyzing surfaces . . . . .</b>	<b>80</b>
6.1	Introduction . . . . .	80
6.2	Experimental setup . . . . .	81
6.2.1	Electron gun . . . . .	81
6.2.2	Electrostatic configuration . . . . .	82
6.2.3	Run settings . . . . .	84
6.3	Simulation of transmission functions . . . . .	84
6.3.1	Determination of the transmission probability . . . . .	85
6.3.2	Determination of the occurrence probability . . . . .	90
6.3.3	Numerical Calculation of Transmission Function . . . . .	92
6.4	Comparison of experimental data to simulation . . . . .	92
6.4.1	Parametrized fits for measured and simulated data . . . . .	92
6.4.2	Comparison of the transmission edge parameter . . . . .	94
6.4.3	Mapping the analyzing surfaces . . . . .	94
6.4.4	Fitting for the optimal gun position . . . . .	95
6.5	Conclusion . . . . .	97
<b>7</b>	<b>Conclusion and Outlook . . . . .</b>	<b>99</b>
<b>A</b>	<b>Analytic Integral Evaluation of Green's Functions over a Triangular Surface . . . . .</b>	<b>101</b>
A.1	Definition of Initial Parameters . . . . .	101
A.2	Dirichlet Boundary Condition . . . . .	102
A.2.1	Integral $I_1(a, b, u)$ . . . . .	103
A.2.2	Integral $\tilde{I}_3(a, b, u)$ . . . . .	104
A.2.3	Integral $\tilde{I}_4(a, b, u)$ . . . . .	105
A.2.4	$\tilde{I}_4(a, b, u_2) - \tilde{I}_4(a, b, u_1)$ . . . . .	107



A.2.5	Integral $I_2(x, u)$ . . . . .	108
A.2.6	Limiting Case: $z = 0$ . . . . .	109
A.3	Extension to Non-Right triangles . . . . .	109
A.4	Neumann Boundary Condition . . . . .	111
<b>B</b>	<b>Analytic Integral Evaluation of Green's Functions over a Rectangular Surface . . . . .</b>	<b>114</b>
B.1	Definition of Initial Parameters . . . . .	114
B.2	Dirichlet Boundary Condition . . . . .	115
B.3	Neumann Boundary Condition . . . . .	115
<b>C</b>	<b>Pseudocode for Single-Element and Multi-Element Robin Hood . . . . .</b>	<b>117</b>
C.1	Single-Element Robin Hood . . . . .	117
C.2	Multiple-Element Robin Hood . . . . .	117
<b>D</b>	<b>Numeric Integration of Scalar and Vector Fields . . . . .</b>	<b>119</b>
D.1	Numeric Integration by Riemann Sum . . . . .	119
D.2	Error Estimates . . . . .	119
D.3	Adaptive Integration . . . . .	120
<b>E</b>	<b>Measured and simulated transmission function plots . . . . .</b>	<b>121</b>
	<b>REFERENCES . . . . .</b>	<b>128</b>

## LIST OF TABLES

1.1	Current best fit values and $3\sigma$ ranges for neutrino oscillation parameters from global $3\nu$ oscillation analysis, taken from (1). In this table, $\Delta m^2$ is defined as $m_3^2 - (m_1^2 + m_2^2)/2$ , $\delta m^2$ is defined as $m_2^2 - m_1^2$ , and an inverted neutrino mass hierarchy is assumed. . . . .	2
5.1	Computation times for the charge density calculation of KATRIN's detector section on the Killdevil cluster at UNC, the Hopper supercomputer at the National Energy Research Scientific Computing Center (NERSC), and on two local GPU-enabled workstations (Jolokia and Scorpion). On both the Killdevil and Hopper systems, MPI-parallel algorithms were used. On Jolokia and Scorpion, OpenCL-parallel algorithms were used. . . . .	56
5.2	Computation times for the charge density calculation of KATRIN's main spectrometer on the GPU-enabled nodes of the Killdevil cluster at UNC, and on a local GPU-enabled workstation. On the Killdevil system, a hybrid MPI & GPU-parallel algorithm was used. On Scorpion, OpenCL-parallel algorithms were used. . . . .	67
6.1	Electron gun parameters. . . . .	82
6.2	Run configurations for the shifted analyzing plane measurement. . . . .	85
6.3	Fitted electron gun parameters from Configurations I and II. . . . .	96

## LIST OF FIGURES

1.1	The (A) total and (B) endpoint of the electron energy spectrum of tritium $\beta$ decay for $m_\nu = 0$ eV and $m_\nu = 1$ eV. The shaded region denotes the measurable difference between the massive and massless neutrino spectra (representing only $2 \times 10^{-13}$ of the total $\beta$ spectrum). Images taken from (2). . . . .	4
1.2	A pictorial representation of the Karlsruhe Tritium Neutrino (KATRIN) experiment (2). The KATRIN beam line is $\sim 70$ m long. . . . .	6
1.3	General setup of a MAC-E-Filter. (Top) experimental configuration and (bottom) the adiabatic momentum transformation of charged particle through the filter. Image taken from (3) . . . . .	7
2.1	A graphical depiction of the region $\Sigma$ and observation point $\mathbf{x}$ with dimensionality $d = 2$ . . . . .	12
2.2	By excluding a small $E_{\mathbf{x}}(\epsilon)$ , we are able to avoid the divergence in Eq. 2.5 when $\mathbf{x} = \mathbf{x}'$ , and $\mathbf{x} \in \Sigma$ . Taking the limit as $\epsilon \rightarrow 0$ , we recover our original domain. . . . .	13
2.3	When $\mathbf{x} = \mathbf{x}'$ , $\mathbf{x} \in \partial\Sigma$ , we exclude a partial sphere $E_{\mathbf{x}}(\epsilon)$ with interior solid angle $\Omega_{\mathbf{x}}$ to eliminate the divergence in Eq. 2.5. Taking the limit as $\epsilon \rightarrow 0$ , we recover our original domain. . . . .	15
2.4	A graphical depiction of $\tilde{\Sigma}$ in 2 dimensions. . . . .	16
2.5	A disjoint boundary $\Gamma$ (solid black line), and a constructed space $\Sigma$ partially bound by $\Gamma$ . The remaining boundary $\partial\Sigma \setminus \Gamma$ (dashed black line) can be assigned the <i>null</i> boundary condition defined in Eq. 2.36, allowing us to apply our formalism on a closed contour. . . . .	20
3.1	(a) A diagram of a spherical capacitor, and (b) its boundaries discretized into 4112 triangles, colored for clarity. . . . .	34
3.2	Comparison of (a) analytic (blue) to computed (green) electric potential and electric field magnitude and (b) their residuals (boundaries have been discretized into 4112 triangles). While the associated charge density profile was computed using the Robin Hood method, the solutions from all solvers display similar results; the error in the computed values is dominated by discretization artifacts. . . . .	36
3.3	Computation time of the spherical capacitor vs dimension for several computation methods, where the elements of $A$ are recomputed each time they were accessed. The single- and 2-element Robin Hood methods overlap with the fastest convergence times. . . . .	37
3.4	Computation time of the spherical capacitor vs dimension for several computation methods, in the case that the elements of $A$ are precomputed prior to the solve. . . . .	38
3.5	Computation time of the spherical capacitor vs dimension for different Robin Hood subspace dimensions. . . . .	39
4.1	Diagram of <code>KSurface</code> basis policies. . . . .	41
4.2	Diagram of <code>KSurface</code> boundary policies. . . . .	42

4.3	Diagram of <code>KSurface</code> shape policies. . . . .	43
4.4	Diagram of <code>KSurface</code> . . . . .	43
4.5	Computed error of the capacitance of the unit cube relative to Hwang et al. with discretized boundary elements that are (a) equal in measure, and (b) scaled according to a power of two near the edges of the cube. Error estimates on the electric field in (b) are omitted for length scales $< 0.01$ due to memory overflow problems related to convergence with the adaptive integrator, but trends in the global and local error of the electric field are still identifiable. . . . .	49
4.6	Absolute Error of the electrostatic potential and electric field for the unit cube with discretized boundary elements that are (a) equal in measure, and (b) scaled according to a power of two near the edges of the cube. . . . .	49
4.7	Error analysis of (a) the computed charge and (b) electrostatic potential and electric field for the spherical capacitor. Error estimates on the electric field in (b) are omitted for length scales $< 0.02$ due to memory overflow problems related to convergence with the adaptive integrator, but trends in the global and local error of the electric field are still identifiable. . . . .	51
5.1	A side-by-side comparison of a photograph looking downstream inside KATRIN's main spectrometer (left) and its representation in <code>KGEOBAG</code> (right). . . . .	54
5.2	A CAD representation of the KATRIN FPD system, with the flux tube in green (4). In this orientation, the direction of the beam line is up and to the right. For a length scale, the pinch magnet (upstream) casing is 711 mm, and the detector magnet (downstream) casing is 910 mm. . . . .	55
5.3	(a) A <code>KGEOBAG</code> representation of the KATRIN FPD system, and (b) an area measure of its discretization, colored by area. The model consists of 444,821 elements. . . . .	57
5.4	(a) The computed charge density (scaled to accentuate small deviations from zero) and (b) electrostatic potential (color scale) and magnetic field lines (white) in the KATRIN FPD system. . . . .	58
5.5	Diagrammatic representation of a Penning trap search simulation. . . . .	60
5.6	(a) Sampling points for a full (green) and focused (blue) Penning trap searches in the KATRIN FPD system, and (b) the field lines corresponding to these sampling points. . . . .	61
5.7	Result of a Penning trap search in the KATRIN FPD system. In this image, sampling points are assigned values according to the depth of the Penning trap at the sampling point (labeled $G$ in Table 5.5 (i)). . . . .	62
5.8	A diagram of KATRIN's main spectrometer, with superconducting magnets (green) at its entrance and exit. . . . .	63
5.9	(a) A schematic of the use of wire arrays to improve background rejection in the main spectrometer (in the cylinder section of the main spectrometer: $d_1 = 0.3$ mm, $d_2 = 0.2$ mm, $l_1 = 150$ mm, $l_2 = 220$ mm, $s = 25$ mm, $\delta U_1 = 100$ V, $\delta U_2 = 200$ V). Image from (5). (b) A photograph of one of the 248 wire modules that tile the inside of KATRIN's main spectrometer. . . . .	63
5.10	A cross-section of a wire module ring in the cylindrical section of the main spectrometer. The teeth of the wire module combs are capped by a long, narrow metal strip, labeled in this image as <i>caps</i> . . . . .	64

5.11	A diagram of the wire module placements (rings 2 – 16) in KATRIN’s main spectrometer. . .	64
5.12	A diagram of KATRIN’s main spectrometer with the air coil system. The green air coils represent the low field correction system (LFCS), and the blue, red and orange air coils denote the elements that comprise the Earth magnetic field compensation system (EMCS). Image from (6). . . . .	65
5.13	KATRIN’s main spectrometer, generated using KGEOBAG. To reproduce the effects of the electrodes immediately upstream and downstream from the spectrometer, additional cylinders held at ground have been added to the entrance and exit of the spectrometer. Surface elements are colored by $\log_{10}(\text{area})$ . . . . .	66
5.14	(a) A potential configuration and (b) the corresponding charge density profile for KATRIN’s main spectrometer (scaled to accentuate small deviations from zero). . . . .	68
5.15	Diagram of the short circuits that resulted from bake-out. Image from (7). . . . .	69
5.16	KGEOBAG representations of the (a) full metal, (b) steep cone, (c) small flat cone, (d) middle flat cone, (e) large flat cone and (f) cylinder wire modules. . . . .	70
5.17	Potential profile of the main spectrometer for (a) the nominal condition, and (b) with short circuits. Figure (a) shows a $\Delta U$ between the inner and outer wire electrodes of 100 V, while in Figure (b) $\Delta U = 0$ V. . . . .	72
5.18	(a) Pictorial representation of the electrostatic potential at the analyzing plane near the wire modules for the nominal condition. For scale, the distance between the teeth of the wire module combs is 25 mm. (b) Azimuthal dependence of the electrostatic potential at the analyzing plane of the main spectrometer at different fixed radii for the nominal condition. The plotted values are the differences between the potential at a field point and the potential of the inner wire electrode system. Image from (8). . . . .	73
5.19	(a) Pictorial representation of the electrostatic potential at the analyzing plane near the wire modules for the shorted condition. For scale, the distance between the teeth of the wire module combs is 25 mm. (b) Azimuthal dependence of the electrostatic potential at the analyzing plane of the main spectrometer at different fixed radii for the shorted condition. The plotted values are the differences between the potential at a field point and the potential of the inner wire electrode system. Image from (8). . . . .	74
5.20	Electrostatic potential along magnetic field lines for a magnet configuration optimized for the nominal condition (a) in the intended nominal case, and (b) with short circuits. Magnetic field lines are colored from blue to red by increasing radius within the flux tube region. In (a), the more positive wire combs result in an increase in the electrostatic potential at $z \approx \pm 0.9$ , even when partially offset by the wire comb caps. In (b), the wire combs and caps produce the opposite effect, creating two separate minima for larger radii that are no longer aligned with the minimum of the magnetic field. Images from (8). . . . .	74
5.21	Measured values for the center of the spectrometer vessel prior to wire installation. For reference, the design value for the radius of the middle of the spectrometer is 4.9 m. Images from (9). . . . .	75
5.22	Two-dimensional interpolated vessel deformation profile. Measured values are represented by black dots. . . . .	76

5.23	(a) East and (b) West sides of the main spectrometer model, with vessel deformation effects included (coloring only applies to the spectrometer vessel, not the ports). . . . .	77
5.24	Simulated potential values for the main spectrometer at $z = 0$ , $r = 3, 4$ m with the deformed vessel held at ground, and the wire system held at 1 kV. For this plot, $\theta = 0$ corresponds to the West direction, $\theta = \frac{\pi}{2}$ corresponds to the positive vertical direction, $\theta = \pi$ corresponds to the East direction, and $\theta = \frac{3\pi}{2}$ corresponds to the negative vertical direction. At $r = 4$ m (blue), both the effects from vessel deformation and the C-profiles of the wire modules can be observed. For $r = 3$ m (green), the effects from individual C-profiles has diminished, and the effects from vessel deformation become the dominant perturbative effect. . . . .	78
6.1	(a) CAD representation of the electron gun (with the beam axis from right to left). The cylinder on the right (grey) houses the gun's cathode and anode, and the curved section (pink) depicts the angular selection mechanism. The gun is mounted to the main spectrometer entrance magnet (aqua). Image from (10). (b) Description of electron gun parameters ( $\alpha_v, \alpha_h$ ) and the parameters used in analysis ( $\rho_{gun}, \theta_{gun}$ ), with origin at $\mathbf{x}_m$ . . . . .	81
6.2	Simulation comparing the electron gun's user-selected angle to the resultant pitch angle of ejected particles at the spectrometer's entrance, for $\Phi_{anode} - \Phi_{cathode} = 50$ V. Calculated for electron starting energies which are Gaussian distributed around 0.2 eV with a sigma of 0.2 eV. Image courtesy of M. Zacher (personal communication, June 26, 2014). . . . .	82
6.3	Electrostatic configurations for shifted analyzing plane measurements. Configurations I through V have a single downstream wire module ring (rings 12 through 16, respectively) held at $-1$ kV, with the remaining rings held at $-900$ V. For all measurements, the spectrometer vessel was held at ground. . . . .	83
6.4	Measured (black) and simulated (red) transmission function profiles for Run 6176. Prior to simulation, the electron gun's position was fit to minimize the difference in the measured and simulated energy edge for measurements corresponding to Configurations I and II (see Sec. 6.2.3). . . . .	93
6.5	A comparison of the measured and simulated edge fit values with respect to $\theta_{gun}$ , the angle between the electron gun's manipulator arm and the beam axis. Simulations were performed with the electron gun parameters described in Table 6.1. . . . .	94
6.6	Simulated transmission surfaces from left to right: Configuration V (blue), I (green), II (magenta), III (cyan), IV (red). . . . .	95
6.7	Starting positions for fixed threshold and $\theta_{gun}$ for each run. The average position of Configurations I and II is represented by a black star. . . . .	96
6.8	A comparison of the measured and simulated edge fit values with respect to $\theta_{gun}$ , the angle between the electron gun's manipulator arm and the beam axis. Simulations were performed with the electron gun parameters described in Table 6.3. . . . .	97
A.1	A right triangular sub-element defined by the position of the corner opposite the hypotenuse $\mathbf{p}_0$ , the lengths of the sides $a$ and $b$ , and the unit vectors in the directions of sides $a$ and $b$ , labeled $\mathbf{n}_1$ and $\mathbf{n}_2$ . The field point is defined as $\mathbf{p}$ , with local coordinates $(0, 0, z)$ . The corners of the triangle are recast into local coordinates to facilitate integration. . . . .	101

- A.2 A non-right triangular sub-element defined by a corner  $\mathbf{p}_0$ , the length of the longest side  $a$  and corresponding height  $b$ , and the unit vectors in the directions of the sides connected to  $\mathbf{p}_0$ , labeled  $\mathbf{n}_1$  and  $\mathbf{n}_2$  ( $\mathbf{n}_1$  always points in the direction of  $a$ ). The field point is defined as  $\mathbf{p}$ , with local coordinates  $(0, 0, z)$ . The corners of the triangle are recast into local coordinates to facilitate integration. . . . . 110
- B.1 A rectangular sub-element defined by the position of the corner opposite the hypotenuse  $\mathbf{p}_0$ , the lengths of the sides  $a$  and  $b$ , and the unit vectors in the directions of sides  $a$  and  $b$ , labeled  $\mathbf{n}_1$  and  $\mathbf{n}_2$ . The field point is defined as  $\mathbf{p}$ , with local coordinates  $(0, 0, z)$ . The corners of the triangle are recast into local coordinates to facilitate integration. . . . . 114

## LIST OF ABBREVIATIONS AND SYMBOLS

AMD	Advanced Micro Devices
BEM	Boundary Element Method
BiCGStab method	stabilized biconjugate gradient method
CAD	Computer-Aided Design
CGAL	Computational Geometry Algorithms Library
C.L.	Confidence Level
CPU	Central Processing Unit
DXF	Drawing Exchange Format
EMCS	Earth magnetic field compensation system
FPD	Focal Plane Detector
GPU	Graphical Processing Unit
KATRIN experiment	Karlsruhe Tritium Neutrino experiment
LED	Light Emitting Diode
LFCS	low field correction system
MAC-E-Filter	Magnetostatic Adiabatic Collimation followed by a Electrostatic Filter
MNS matrix	Maki-Nakagawa-Sakata matrix
MPI	Message Passing Interface
NERSC	National Energy Research Scientific Computing Center
PDE	Partial Differential Equation
PETSc	Portable, Extensible Toolkit for Scientific Computation
SI	International System of Units



SSC method	Successive Subspace Correction method
STL	Standard Template Library
UNC	University of North Carolina
UV	Ultraviolet
VTK	Visualization Toolkit
XML	Extensible Markup Language

## CHAPTER 1: Introduction

### Section 1.1: Motivation for measurement of the neutrino mass

#### 1.1.1: Evidence for neutrino mass from flavor oscillation

The canonical Standard Model of particle physics, a theory that has successfully predicted the experimental results of almost all particle physics experiments in the past forty years, presupposes the neutrino to be massless. In the past 20 years, several experiments measuring neutrinos from the sun and from interactions in our atmosphere have uncovered compelling evidence to the contrary, linking the mass of the neutrino to an observable phenomenon known as *flavor oscillation* (11). In the commonly accepted 3-neutrino model of flavor oscillations, a neutrino interacts according to its flavor eigenstates ( $|\nu_\alpha\rangle$ ,  $\alpha = e, \mu, \tau$ ) and propagates through space according to its mass eigenstates ( $|\nu_i\rangle$ ,  $i = 1, 2, 3$ ). The mass and flavor eigenstates of a neutrino are related by the unitary Maki-Nakagawa-Sakata (MNS) matrix  $U_{\alpha i}$  (12):

$$|\nu_i\rangle = \sum_{\alpha} U_{\alpha i} |\nu_\alpha\rangle. \quad (1.1)$$

When a neutrino is created, it is in a flavor eigenstate ( $|\nu_\alpha\rangle$ ). As it propagates through space, it becomes a time-varying superposition of the three flavor eigenstates ( $|\nu(t)\rangle = \sum_{\alpha} C_{\alpha}(t) |\nu_\alpha\rangle$ ) whose amplitudes  $C_{\alpha}(t)$  are determined by components of the MNS matrix, the time of propagation, the momentum of the neutrino and the mass squared differences between neutrino mass eigenstates. Upon *charged-current* weak interaction\*, the neutrino wave function interacts as one of the three flavor eigenstates with the probability  $P(\nu_\alpha)(t) = |C_{\alpha}(t)|^2$ .

In the case of two-flavor<sup>†</sup> oscillations,  $U_{\alpha i}$  can be represented as a simple rotation matrix dependent upon a single mixing angle  $\theta$ , and the probability of neutrino oscillation is expressed as

$$P(\nu_\alpha \rightarrow \nu_\beta) = \sin^2(2\theta) \times \sin^2\left(\frac{1.27\Delta m_{12}^2 L}{E}\right), \quad (1.2)$$

---

\*an interaction mediated by a  $W^\pm$  boson

<sup>†</sup>Though there are three neutrino flavors, the two-flavor model of neutrino oscillation is useful since neutrino oscillation experiments are usually only sensitive to one baseline.

where  $\Delta m_{12}^2 = m_1^2 - m_2^2$  is the mass squared difference of the mass eigenstates in  $\text{eV}^2$ ,  $L = c \cdot t$  is the distance from the neutrino's creation to detection in kilometers, and  $E$  is the neutrino energy in GeV (13). For three-flavor oscillations for Dirac neutrinos, there are six parameters intrinsic to the neutrino that determine its oscillatory properties: two mass squared differences ( $\Delta m_{21}^2 \simeq \Delta m_{\odot}^2$ ,  $\Delta m_{32}^2 \simeq \Delta m_{atm}^2$ ), three mixing angles ( $\theta_{12}$ ,  $\theta_{23}$ , and  $\theta_{13}$ ), and a CP violating phase ( $\delta$ ). The current best fit values and  $3\sigma$  ranges for the neutrino oscillation parameters are provided in (1), and are reproduced in Table 1.1:

Parameter	Best fit	$3\sigma$ range
$\delta m^2/10^{-5} \text{ eV}^2$	7.54	6.99 - 8.18
$\sin^2\theta_{12}/10^{-1}$	3.08	2.59 - 3.59
$\Delta m^2/10^{-3} \text{ eV}^2$	2.38	2.19 - 2.56
$\sin^2\theta_{13}/10^{-2}$	2.40	1.78 - 2.98
$\sin^2\theta_{23}/10^{-1}$	4.55	3.80 - 6.41
$\delta/\pi$	1.31	0.98 - 1.60 ( $1\sigma$ range)

Table 1.1: Current best fit values and  $3\sigma$  ranges for neutrino oscillation parameters from global  $3\nu$  oscillation analysis, taken from (1). In this table,  $\Delta m^2$  is defined as  $m_3^2 - (m_1^2 + m_2^2)/2$ ,  $\delta m^2$  is defined as  $m_2^2 - m_1^2$ , and an inverted neutrino mass hierarchy is assumed.

### 1.1.2: Significance of neutrino mass

By measuring nonzero splittings between the mass eigenstates, neutrino oscillation implies that at least two of the three neutrinos are not massless. The evidence of massive neutrinos has given rise to several interesting questions in neutrino physics theory. The three most prominent questions related to neutrino mass are:

- are neutrinos *Dirac* ( $\nu$  and  $\bar{\nu}$  are distinct) or *Majorana* ( $\nu = \bar{\nu}$ ) particles,
- what is the ordering of the mass eigenstates, and
- what is the overall scale of the neutrino masses?

While there are several different experiments currently underway whose primary focus is to answer one of these three questions, it should be noted that the physics motivating these questions is largely interrelated, and that information about any one of these three questions will invariably shed light on the other two. As such, the Karlsruhe Tritium Neutrino (KATRIN) experiment is specifically designed to measure the overall scale of the neutrino masses, and its result will also complement the results of other neutrino experiments.

### 1.1.3: Current limits on the neutrino mass scale

There are several experimental techniques that can be used to determine the neutrino mass scale. Measured anisotropies in the cosmic microwave background, in conjunction with other measured astronomical

parameters, set the sum of the three neutrino masses to be  $\sum m_\nu < 0.23$  eV (14). This constraint is dependent upon the assumptions made in the cosmological model to which these parameters are fit, however. Experiments designed to measure a process known as neutrinoless double-beta decay, a process whose half-life is associated with a *Majorana mass term* ( $m_{\beta\beta}$ , an incoherent sum of the electron neutrino mass states), have set a limit on  $m_{\beta\beta}$  to be less than 140 – 380 meV (15). This constraint is also model-dependent, and would necessarily equal zero if neutrinos are Dirac particles. Finally, the current best limit on the mass of the neutrino via tritium beta decay ( $m_\beta$ , discussed further in Sec. 1.2.1) has been set in 2005 by the Mainz experiment to be  $m_\beta < 2.3$  eV (95% C.L.) (16) and more recently by the Troitsk experiment in 2012 to be  $m_\beta < 2.05$  eV (95% C.L.) (17). Measurements of this type are referred to as *direct* searches, since the value to be measured is independent of any physics model.

## Section 1.2: The KATRIN experiment

The Karlsruhe Tritium Neutrino (KATRIN) experiment is a tritium beta decay experiment designed to make a direct, model independent measurement of neutrino mass with a sensitivity of  $m_\beta = 0.2$  eV (90% C.L.), an order of magnitude lower than the current limit, with a 5 sigma discovery level of 0.35 eV. To extract a neutrino mass from KATRIN one needs to understand the generation of an electron energy spectrum via tritium  $\beta$  decay, and the subsequent transport and measurement of this energy spectrum.

### 1.2.1: Kinematics of tritium $\beta$ decay

Tritium  $\beta$  decay is described by the following reaction:



Noting that  $\bar{\nu}_e$  is a superposition of the three mass eigenstates, the energy spectrum of the outgoing electron in this process is

$$\frac{dN}{dE} = C \times F(Z, E) p(E + m_e c^2) (E_0 - E) \sum_i |U_{ei}|^2 [(E_0 - E)^2 - m_i^2]^{\frac{1}{2}} \Theta(E_0 - E - m_i), \quad (1.4)$$

where  $E$  is the electron energy,  $m_e$  is the mass of the electron,  $p$  is the electron momentum,  $E_0$  represents the maximum electron energy (setting  $m_\nu = 0$ ),  $F(Z, E)$  is the Fermi function (accounting for the Coulomb interaction between the outgoing electron and the  ${}^3\text{He}^+$  nucleus),  $\Theta(E_0 - E - m_\nu)$  is the Heaviside step

function (to ensure energy conservation), and

$$C = \frac{G_F^2}{2\pi^3} \cos^2 \theta_C |M|^2, \quad (1.5)$$

where  $G_F$  is the Fermi constant,  $\theta_C$  is the Cabibbo angle and  $M$  is the nuclear matrix element (18). Three properties of Equation 1.4 are particularly worthy of note: first, the measurement of the  $\beta$  energy spectrum is independent of whether the neutrino is Majorana or Dirac. Second, if the energy resolution of the experiment is less than the splittings between the mass eigenstates of the neutrino (as is the case for KATRIN), the mass  $m_\nu$  can be treated as a weighted average of the neutrino mass eigenstates that comprise  $\bar{\nu}_e$  (19). In other words, we can rewrite Equation 1.4 with

$$m_\beta^2 = \sum_i |U_{ei}|^2 m_i^2 \quad (1.6)$$

as

$$\frac{dN}{dE} = C \times F(Z, E) p(E + m_e c^2) (E_0 - E) [(E_0 - E)^2 - m_\beta^2]^{\frac{1}{2}} \Theta(E_0 - E - m_\beta), \quad (1.7)$$

producing a single observable in experiment that is dependent upon all three neutrino mass eigenstates. Finally, the count rate of electrons near the end-point energy can be determined by Equation 1.4 to be proportional to  $(E_0 - E)^3$ , which quickly approaches zero at the endpoint.

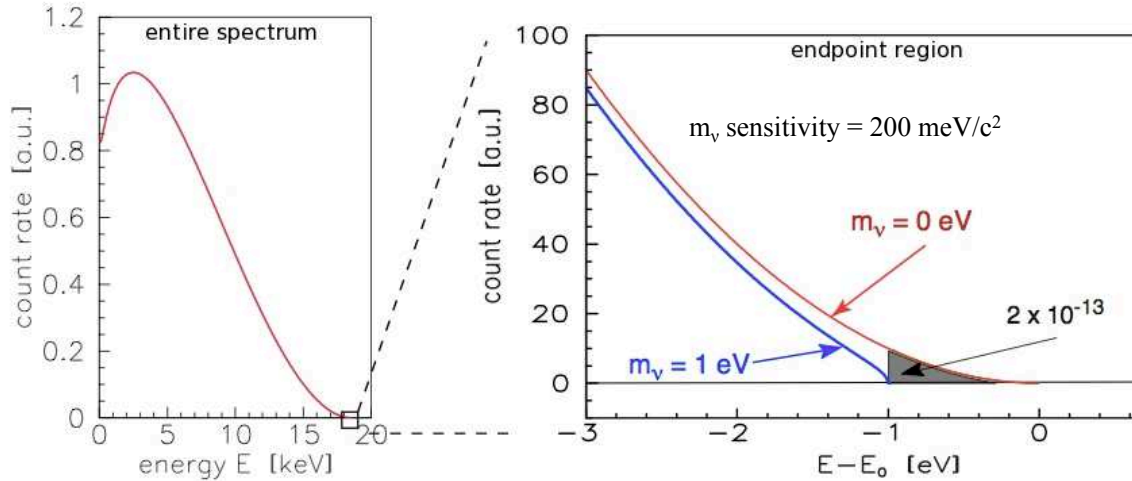


Figure 1.1: The (A) total and (B) endpoint of the electron energy spectrum of tritium  $\beta$  decay for  $m_\nu = 0$  eV and  $m_\nu = 1$  eV. The shaded region denotes the measurable difference between the massive and massless neutrino spectra (representing only  $2 \times 10^{-13}$  of the total  $\beta$  spectrum). Images taken from (2).

Using Equation 1.4, tritium  $\beta$  decay experiments measure the neutrino mass by measuring the variance of the shape of the endpoint of the electron energy spectrum from the  $m_\nu = 0$  spectrum. As depicted in

Figure 1.1, the fraction of events in the region of sensitivity to a massive  $\bar{\nu}_e$  is very small: for example, only  $2 \times 10^{-13}$  of the emitted  $\beta$  decays account for the last 1 eV of the spectrum. The ability to accurately obtain a signal for a significantly small neutrino mass is therefore strongly dependent upon the luminosity of the tritium source, as well as the ability to precisely filter the emitted electrons below a given energy threshold<sup>‡</sup>. (3).

### 1.2.2: Overview of the apparatus

The KATRIN apparatus is depicted in Figure 1.2. In the Windowless Gaseous Tritium Source (WGTS), Tritium molecules  $\beta$  decay with an endpoint energy of 18.6 keV within a solenoidal magnetic field, producing an electron beam with a luminosity of  $4.25 \times 10^{10} \frac{\beta}{s}$ . This electron beam is transported along magnetic field lines through the differential and cryogenic pumping sections (DPS and CPS, respectively), where the residual gas molecules from the WGTS are removed, resulting in a tritium reduction factor of  $10^{11}$ . The beam then passes through a rough ( $\sim 100$  eV resolution) and fine ( $\sim 1$  eV resolution) integrating energy filter, respectively named the pre-spectrometer and main spectrometer (see Sec. 1.2.3 for a description of this filter type). Finally, the beam is deposited on a silicon pin diode detector in the detector section, designed to obtain a count rate of the  $\beta$  beam with a background rate  $\leq 1$  mHz (2)(3).

### 1.2.3: Measurement of the electron energy spectrum

In order to resolve the shape near the endpoint energy of the resultant electron spectrum with sufficient resolution to extract the neutrino mass, KATRIN employs an integral spectrometer known as a Magnetic Adiabatic Collimation followed by an Electrostatic Filter (MAC-E-Filter, see Fig. 1.3) (20)(21)(22). The filter is designed to adiabatically transfer a charged particle's transverse momentum into longitudinal momentum using magnetostatic fields of different strengths, and then to perform an energy rejection using electrostatic fields. For a magnetic field that varies from  $B_{max}$  to  $B_{min}$  and an electric potential at the analyzing plane of  $U_0$ , the transmission function of a MAC-E-Filter rises from 0 to 1 for an electron with kinetic energy  $T_0$  as

$$qU_0 \leq T_0 \leq qU_0 \left( 1 + \frac{B_{min}}{B_{max}} \right), \quad (1.8)$$

corresponding to a resolving power of

$$\frac{T_0}{\Delta T} = \frac{U_0}{\Delta U} = \frac{B_{max}}{B_{min}}. \quad (1.9)$$

---

<sup>‡</sup>Additional corrections to the spectrum shape due to the nuclear recoil and final state distributions of molecular tritium contribute as subdominant limitations on KATRIN's ability to measure a signal (2).

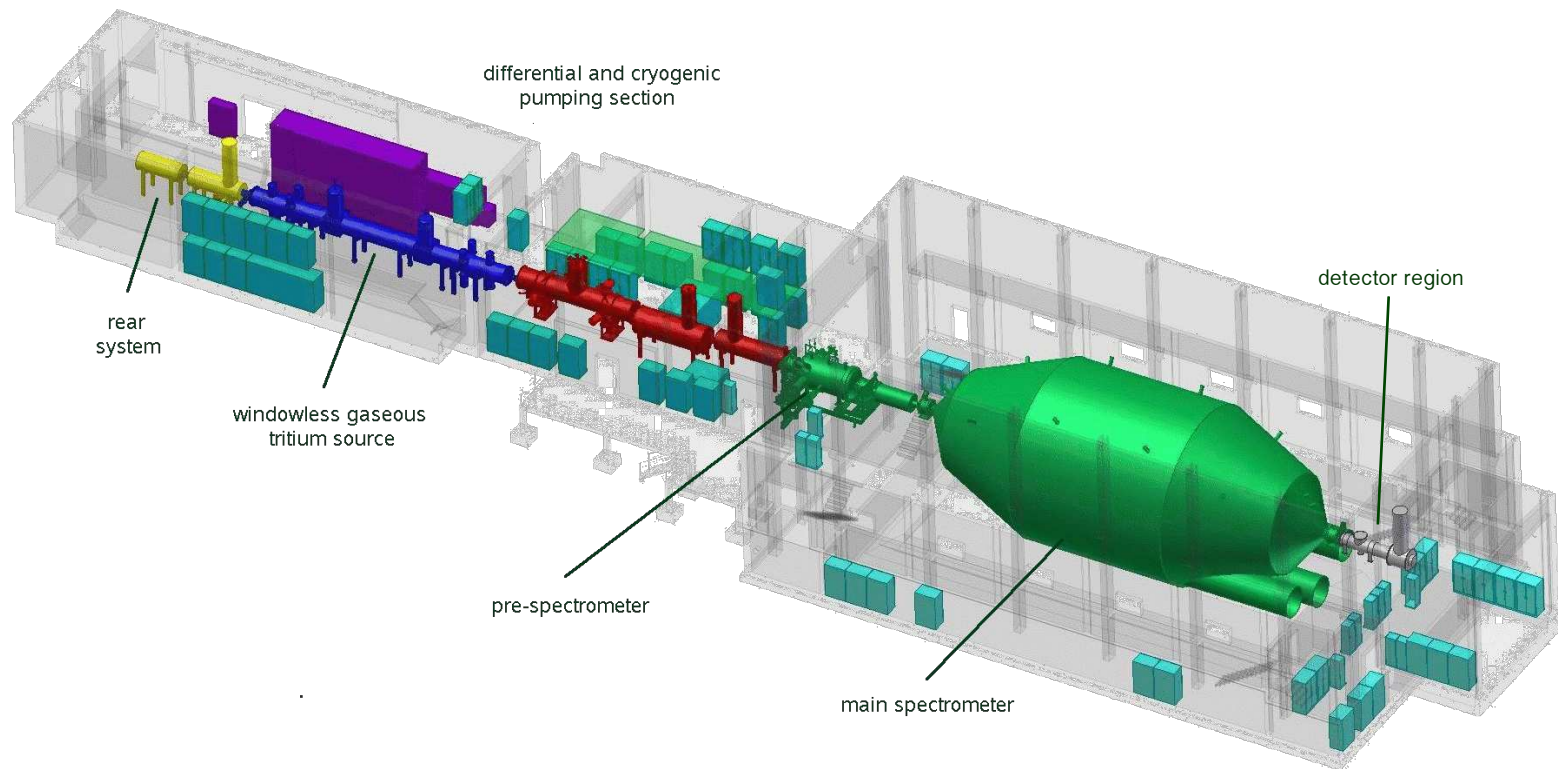


Figure 1.2: A pictorial representation of the Karlsruhe Tritium Neutrino (KATRIN) experiment (2). The KATRIN beam line is  $\sim 70$  m long.

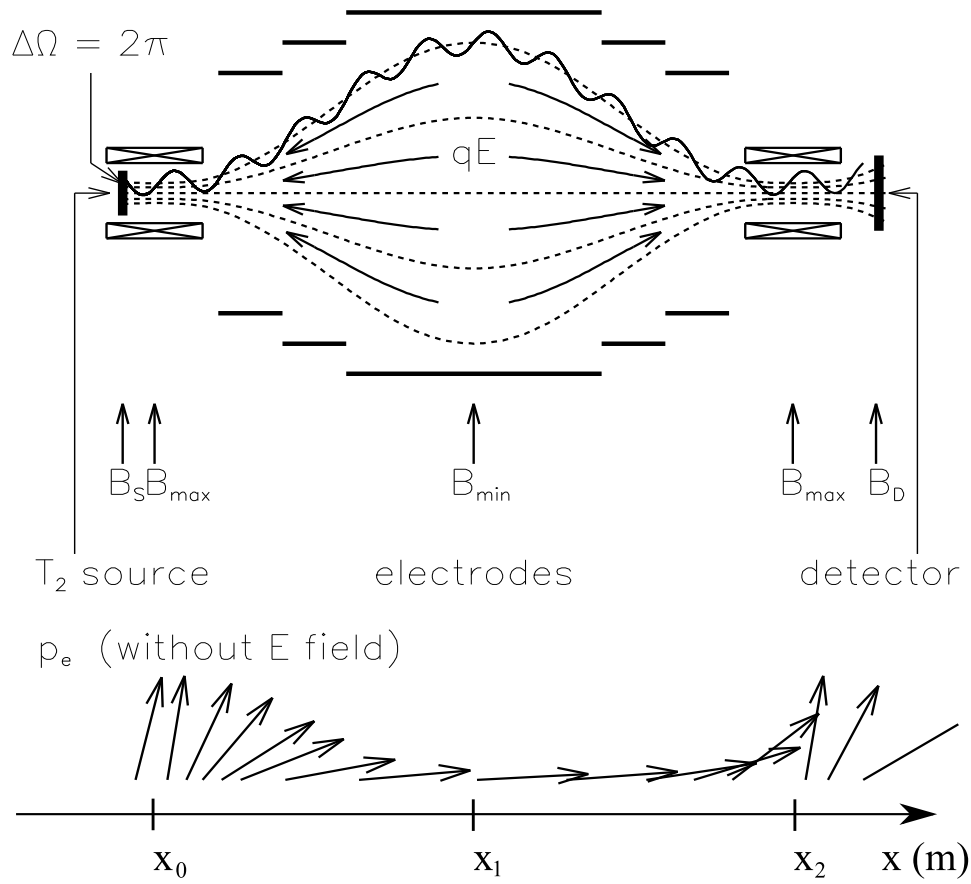


Figure 1.3: General setup of a MAC-E-Filter. (Top) experimental configuration and (bottom) the adiabatic momentum transformation of charged particle through the filter. Image taken from (3)



The relationship between  $B_{max}$  and  $B_{min}$  determines the volume of the MAC-E-Filter (or, in the case of KATRIN, the volume is also constrained by the size of the streets from the river Rhine to the experimental hall!). For the purposes of simulation, this fact is critical because it determines the large macroscopic scale intrinsic to electrostatic modeling for the KATRIN experiment. Once the filtered particles exit the spectrometer, they are collected using a silicon semiconductor detector.

#### 1.2.4: KATRIN signal and background rates

As mentioned in 1.2.1, the integrated region of the tritium  $\beta$  spectrum that is used to fit for the neutrino mass represents a very small fraction of the entire spectrum. As a result, KATRIN requires a very intense source in order to achieve a  $m_\nu$  sensitivity of 0.2 eV. To this end, KATRIN's gaseous tritium source is designed to transport  $4.25 \times 10^{10}$   $\beta$  per second to the entrance of the spectrometers. This rate corresponds to a rate of  $\sim 10^{-2}$   $\beta$  per second within the last eV of the energy spectrum (the shaded region in Fig. 1.1).

Another requirement for attaining KATRIN's desired sensitivity is a relatively small background. The primary source of background in KATRIN is expected to come from particles generated within the main spectrometer, and is mitigated by a complex electrode system (see Chapter 5) and ultra-high vacuum within the vessel. With these preventative measures in place, the main spectrometer is designed to contribute backgrounds at or below 10 mHz at the tritium endpoint energy. Finally, to achieve a sufficient reduction of statistical error, the experiment is expected to take data by scanning over the endpoint of the energy spectrum, with interlaced calibration runs to monitor the stability of the apparatus, for  $\sim 3$  years (23).

#### 1.2.5: Impact on neutrino physics theory

Given the expected range of sensitivities attainable by KATRIN, either an upper limit or a definitive measurement of the neutrino mass will yield important results to determining the nature of neutrino mass. If a value for the mass  $m_\nu$  can be determined, we will be able to fix the absolute mass spectrum of the mass eigenstates. Because the splittings of the mass eigenstates are an order of magnitude smaller than the expected sensitivity of KATRIN, the reconstructed neutrino mass will be a weighted average of the three mass eigenstates according to Equation 1.6 and, while not sensitive to mass ordering, would determine that the neutrino masses are nearly degenerate. Such a measurement could also be used in tandem with  $0\nu\beta\beta$  experiments to determine whether neutrinos are Majorana particles. The absence of a signal would result in the most competitive direct limit on the absolute neutrino mass scale to date, and additionally constrain cosmological parameters by providing external prior knowledge of the neutrino mass range for parametrized cosmological fits (24).

## Section 1.3: Electromagnetic simulations in the KATRIN experiment

### 1.3.1: Boundary Element Method

To characterize the properties of its particle transport and filtering apparatus, an accurate simulation of KATRIN's electromagnetic fields is required. To achieve this goal, we have developed a Boundary Element Method (BEM) for converting three-dimensional boundary value problems in potential theory into a numerically soluble linear algebraic form. A description of this technique is given in Chapter 2.

### 1.3.2: Robin Hood linear algebraic solver

As a result of the large range of length scales inherent in KATRIN's transport and spectrometer system, the linear algebraic equations generated by our BEM can quickly become very large (resulting in dense square matrices with rank  $\sim 10^6$ ). To solve these systems of equations, we have employed a novel quasi-stationary Robin Hood linear algebraic solver, and adapted it to perform in high-performance computing environments. The Robin Hood linear algebraic solver is described in greater detail in Chapter 3.

### 1.3.3: Electromagnetic simulation software

Following the theoretical description of the BEM and Robin Hood solver, Chapter 4 provides a description of their implementation in the `KEMField` software. We also briefly present `KGeoBag`, software designed to describe the complex geometries inherent in the KATRIN experiment. In some respects, `KGeoBag` has been designed to operate as a front-end to `KEMField`: `KGeoBag` accepts user-defined descriptions of macroscopic geometry elements and provides navigation, discretization and visualization routines for them. These elements are then passed into `KEMField`, whose primary focus is the high-performance computation of the BEM and subsequent field queries.

### 1.3.4: Application to the KATRIN experiment

With the aforementioned software tools in place, Chapter 5 exhibits the application of `KGeoBag` and `KEMField` to KATRIN's spectrometer and detector section (SDS). We present a description of the three-dimensional models prepared for the detector section and main spectrometer, and the results of the application of the BEM to these geometries. Additionally, we describe several analyses that were performed using these models.

### 1.3.5: Shifted analyzing surfaces

Finally, to validate our model of KATRIN's main spectrometer, in Chapter 6 we present an analysis of measurements taken during KATRIN's spectrometer commissioning, where the electrostatic configuration of the main spectrometer was adjusted to shift its analyzing surface away from the center of the vessel. To do this, we first present a technique for simulating the transmission function from a point-like electron gun source. We then compare the results of simulation to their empirical counterparts.

## **Section 1.4: Summary**

In the past 20 years we have been witness to a complete paradigm shift in our understanding of neutrinos. The confirmation of the theory of neutrino oscillation has raised as many questions as it has answered, as the task of accommodating massive neutrinos in the Standard Model that fit experimental measurements is a nontrivial task. At present, the questions of the Majorana versus Dirac nature of neutrinos, the ordering of the neutrino mass hierarchy and the absolute neutrino mass scale comprise some of the central questions to be answered in neutrino physics. The KATRIN tritium  $\beta$  decay experiment is currently the most sensitive method for probing the absolute neutrino mass scale. To this end, the characterization of the transport and filtering sections is a critical task within the KATRIN experiment. To handle the complexity of KATRIN's apparatus and the level of accuracy required for characterization, large-scale simulations that employ high-performance computation techniques have been developed. The following chapters describe these methods, as well as their implementation in software and application to the KATRIN experiment.

## CHAPTER 2: Boundary Element Method

### Section 2.1: Introduction

The Boundary Element Method (BEM) is a technique for numerically solving linear partial differential equations (PDEs) that can be represented as an integral over the domain boundary. Compared to other popular methods like the Finite Element and Finite Difference Methods, the BEM requires that all source terms reside on the system's boundaries, rather than its interior (25). This restricts the applicability of the technique to a subset of PDEs, but also reduces the dimensionality of the problem and facilitates the calculation of fields for regions that extend out to infinity (rather than restricting computation to a finite region) (26). These two features make the BEM more favorable than competing methods when it is applicable.

The method involves taking an integral equation that describes a field as a function of its boundaries, and feeding the boundary conditions into the equation in order to construct a profile for the unknown function in the integrand. Typically, the integral equation is a Fredholm integral equation of the first or second type, defined respectively as

$$f(x) = \int_{\Gamma} K(x, x') \varphi(x') dx' \quad (2.1)$$

and

$$\varphi(x) = f(x) + \lambda \int_{\Gamma} K(x, x') \varphi(x') dx', \quad (2.2)$$

where  $K(x, x')$  (known as the *Fredholm kernel*) and  $f(x)$  are known, square-integrable functions,  $\lambda$  is a constant,  $\Gamma$  is the system's boundary and  $\varphi(x)$  is the function for which we are trying to solve (27).

Many variants of the BEM exist. The version described here is known as an *indirect Boundary Element Method*, as the technique emphasizes matching the solution function's values or derivatives across domains that share a common boundary. This is in contrast to *direct Boundary Element Methods*, which use the complete specification of the boundary of a single region to obtain a description of the function in that region\*.

---

\*The term *direct* refers to the act of directly solving for a function's boundary derivative values from the function's boundary values, or vice versa.

## Section 2.2: Conversion of the Laplace Equation to a Fredholm integral equation

### 2.2.1: Description of the Laplace Equation

The governing partial differential equation for electrostatic systems is the Laplace equation:

$$\nabla^2 \phi = 0. \quad (2.3)$$

The Laplace equation admits a unique solution when  $\phi$  is defined on all boundary surfaces (*Dirichlet* boundary conditions),  $\frac{\partial \phi}{\partial n}$  is defined on all boundary surfaces (*Neumann* boundary conditions)<sup>†</sup>, or an admixture of  $\phi$  and  $\frac{\partial \phi}{\partial n}$  are defined along the entire boundary (*mixed* boundary conditions).

To apply the BEM to electrostatics we will convert Equation 2.3 into a Fredholm integral equation of the first type (see Eq. 2.1). We must also ensure that the resulting Fredholm kernel is square-integrable. The following technique is derived from the methods described in (28)(29)(30)(31)(32)(33), and is described in 3 dimensions (with 2-dimensional accompanying images).

### 2.2.2: Integral Statement for the Interior Equation

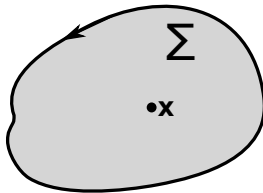


Figure 2.1: A graphical depiction of the region  $\Sigma$  and observation point  $\mathbf{x}$  with dimensionality  $d = 2$ .

We begin by defining a volume  $\Sigma$ , bounded by a piecewise smooth closed and positively oriented contour (see Fig. 2.1). We apply Green's second identity to  $\Sigma$ :

$$\int_{\Sigma} (u \nabla^2 w + w \nabla^2 u) dV = \int_{\partial \Sigma} \left( u \frac{\partial w}{\partial n} - w \frac{\partial u}{\partial n} \right) dS, \quad (2.4)$$

where  $u, w : \mathbb{R}^3 \rightarrow \mathbb{R}$  are  $C^2$  continuous in  $\Sigma$  and on its boundaries  $\partial \Sigma$ , and  $\frac{\partial w}{\partial n}$  is the magnitude of the gradient of  $w$  in the direction of the outward pointing normal  $\mathbf{n}$  to the surface element  $dS$ <sup>‡</sup>. We let  $u$  be the

---

<sup>†</sup>Neumann boundary conditions uniquely specify a solution up to an additive constant.

<sup>‡</sup>We define  $C^2$  continuity for a function  $f(\mathbf{x})$  on  $V \cup \partial V$  in the limiting sense:  $\forall \mathbf{x} \in V \cup \partial V, \mathbf{y} \in V, \lim_{\mathbf{y} \rightarrow \mathbf{x}} f(\mathbf{x})$  and  $\lim_{\mathbf{y} \rightarrow \mathbf{x}} \frac{\partial f(\mathbf{x})}{\partial n}$  are well-defined.

solution to Equation 2.3, eliminating one of the terms on the left-hand side of Equation 2.4 and leaving us with

$$\int_{\Sigma} \phi \nabla^2 w \, dV = \int_{\partial\Sigma} \left( \phi \frac{\partial w}{\partial n} - w \frac{\partial \phi}{\partial n} \right) dS. \quad (2.5)$$

Next, we choose a suitable  $w$  to eliminate the remaining domain integral on the left-hand side of Equation 2.5, so that only calculations around the boundaries of  $\Sigma$  remain. This is done by casting the left-hand side as a singular integral whose kernel is the fundamental solution of the Laplace equation,  $G : \mathbb{R}^3 \times \mathbb{R}^3 \rightarrow \mathbb{R}$ , defined by the property

$$\nabla'^2 G(\mathbf{x}, \mathbf{x}') = \delta(\mathbf{x} - \mathbf{x}'), \quad (2.6)$$

and one of whose arguments is an (often implied) *observation point*  $\mathbf{x} \in \mathbb{R}^3$ . In 3 dimensions, the fundamental solution to the Laplace equation is

$$G(\mathbf{x}, \mathbf{x}') = \frac{1}{4\pi|\mathbf{x} - \mathbf{x}'|}. \quad (2.7)$$

Immediately, it can be seen that our choice of  $w$  has introduced singularities that could potentially prevent our final Fredholm kernel from being square integrable. It is therefore necessary to address the singularities in Equation 2.5 when  $\mathbf{x} = \mathbf{x}'$ , both in  $\Sigma$  and on its boundaries.

### 2.2.3: Resolving Singularities with Limiting Behaviors

Our approach to dealing with singularities in Equation 2.5 is to excise a parametrized volume containing our observation point (hereafter referred to as  $E_{\mathbf{x}}(\epsilon)$ ) from our domain,  $\Sigma$ , so our equations become integrable. We then observe the behavior of our equations in the limit that the parametrized volume vanishes. We begin by dealing with the singularity that occurs when  $\mathbf{x} = \mathbf{x}'$ , and  $\mathbf{x} \in \Sigma$ . For this condition, we excise

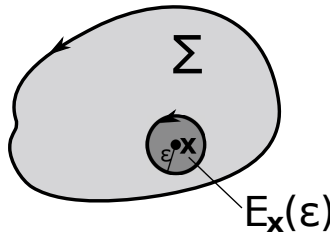


Figure 2.2: By excluding a small  $E_{\mathbf{x}}(\epsilon)$ , we are able to avoid the divergence in Eq. 2.5 when  $\mathbf{x} = \mathbf{x}'$ , and  $\mathbf{x} \in \Sigma$ . Taking the limit as  $\epsilon \rightarrow 0$ , we recover our original domain.

from our domain  $\Sigma$  a parameterized spherical volume  $E_{\mathbf{x}}(\epsilon)$ , centered on our observation point  $\mathbf{x}$  with radius

$\epsilon > 0$  (see Fig. 2.2). This results in a modification of Equation 2.5 to

$$\int_{\Sigma \setminus E_{\mathbf{x}}(\epsilon)} \phi \nabla^2 G \, dV = \int_{\partial \Sigma} \left( \phi \frac{\partial G}{\partial n} - G \frac{\partial \phi}{\partial n} \right) dS - \int_{\partial E_{\mathbf{x}}(\epsilon)} \left( \phi \frac{\partial G}{\partial n} - G \frac{\partial \phi}{\partial n} \right) dS. \quad (2.8)$$

The left-hand side of this equation is then trivially zero (since  $\forall \mathbf{x}' \in \Sigma \setminus E_{\mathbf{x}}(\epsilon) \Rightarrow \nabla'^2 G(\mathbf{x}, \mathbf{x}') = 0$ ), and Equation 2.8 reduces to

$$\int_{\partial \Sigma} \left( \phi \frac{\partial G}{\partial n} - G \frac{\partial \phi}{\partial n} \right) dS = \int_{\partial E_{\mathbf{x}}(\epsilon)} \left( \phi \frac{\partial G}{\partial n} - G \frac{\partial \phi}{\partial n} \right) dS. \quad (2.9)$$

To evaluate the right-hand side of Equation 2.9, we convert into a local spherical coordinate system centered on our observation point:

$$\begin{aligned} \mathbf{x}' - \mathbf{x} &\equiv \boldsymbol{\rho}(\rho, \theta, \varphi), \\ \mathbf{n} &= \frac{\boldsymbol{\rho}}{|\boldsymbol{\rho}|}, \\ dS &= \epsilon^2 d\Omega. \end{aligned} \quad (2.10)$$

We evaluate the first term on the right-hand side to be

$$\begin{aligned} \int_{\partial E_{\mathbf{x}}(\epsilon)} \phi(\mathbf{x}') \frac{\partial}{\partial n} G(\mathbf{x}, \mathbf{x}') \cdot dS &= \int_{\partial E_{\mathbf{x}}(\epsilon)} \phi(\mathbf{x} + \boldsymbol{\rho}) \cdot \frac{\partial}{\partial \rho} \left( \frac{1}{4\pi\rho} \right) \cdot dS = \\ &= \int_{\Omega} d\Omega \cdot \epsilon^2 \cdot \phi(\mathbf{x} + \boldsymbol{\rho}) \cdot \left( -\frac{1}{4\pi\epsilon^2} \right) = \\ &= -\frac{1}{4\pi} \int_{\Omega} d\Omega \cdot \phi(\mathbf{x} + \boldsymbol{\rho}), \end{aligned} \quad (2.11)$$

which, as  $\epsilon \rightarrow 0$ , approaches  $-\phi(\mathbf{x})$ . The second term on the right-hand side of Equation 2.9 becomes

$$\begin{aligned} \int_{\partial E_{\mathbf{x}}(\epsilon)} G(\mathbf{x}, \mathbf{x}') \frac{\partial}{\partial n} \phi(\mathbf{x}') \cdot dS &= \int_{\partial E_{\mathbf{x}}(\epsilon)} \left( \frac{1}{4\pi\rho} \right) \cdot \frac{\partial}{\partial \rho} \phi(\mathbf{x} + \boldsymbol{\rho}) \cdot dS \\ &= \frac{\epsilon}{4\pi} \int_{\Omega} d\Omega \cdot \frac{\partial}{\partial \rho} (\phi(\mathbf{x} + \boldsymbol{\rho}))|_{\rho=\epsilon}, \end{aligned} \quad (2.12)$$

which approaches 0 as  $\epsilon \rightarrow 0$ , since we are guaranteed that  $\frac{\partial}{\partial \rho} \phi(\mathbf{x} + \boldsymbol{\rho})$  is well-behaved by the earlier requirement that  $\forall \mathbf{x}' \in \Sigma : \phi(\mathbf{x}')$  be twice continuously differentiable. We therefore determine that the right-hand side of Equation 2.5 converges to  $\phi(\mathbf{x})$  when  $\mathbf{x} = \mathbf{x}', \mathbf{x} \in \Sigma$ .

Next, we deal with the singularity that occurs for  $\mathbf{x} = \mathbf{x}', \mathbf{x} \in \partial \Sigma$ . In this condition, we excise a partial sphere  $E_{\mathbf{x}}(\epsilon)$  centered on  $\mathbf{x}$  with radius  $\epsilon$  and internal solid angle  $\Omega_{\mathbf{x}}$ . Further, we will define  $S_{\mathbf{x}}^{\Omega}(\epsilon)$  to be the

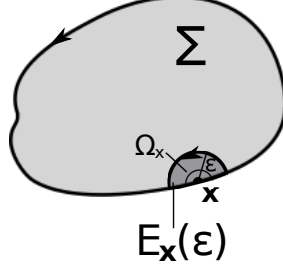


Figure 2.3: When  $\mathbf{x} = \mathbf{x}'$ ,  $\mathbf{x} \in \partial\Sigma$ , we exclude a partial sphere  $E_{\mathbf{x}}(\epsilon)$  with interior solid angle  $\Omega_{\mathbf{x}}$  to eliminate the divergence in Eq. 2.5. Taking the limit as  $\epsilon \rightarrow 0$ , we recover our original domain.

spherical portion of  $\partial E_{\mathbf{x}}(\epsilon)$ , and  $S_{\mathbf{x}}^{\Sigma}(\epsilon)$  to be the portion of  $\partial E_{\mathbf{x}}(\epsilon)$  along  $\partial\Sigma$  (see Fig. 2.3)<sup>§</sup>. This excision changes Equation 2.5 to be

$$\int_{\Sigma \setminus E_{\mathbf{x}}(\epsilon)} \phi \nabla^2 G \, dV = \int_{\partial\Sigma \setminus S_{\mathbf{x}}^{\Sigma}(\epsilon)} \left( \phi \frac{\partial G}{\partial n} - G \frac{\partial \phi}{\partial n} \right) dS - \int_{S_{\mathbf{x}}^{\Omega}(\epsilon)} \left( \phi \frac{\partial G}{\partial n} - G \frac{\partial \phi}{\partial n} \right) dS. \quad (2.13)$$

Once again, the left-hand side of Equation 2.13 evaluates to 0, leaving us with

$$\int_{\partial\Sigma \setminus S_{\mathbf{x}}^{\Sigma}(\epsilon)} \left( \phi \frac{\partial G}{\partial n} - G \frac{\partial \phi}{\partial n} \right) dS = \int_{S_{\mathbf{x}}^{\Omega}(\epsilon)} \left( \phi \frac{\partial G}{\partial n} - G \frac{\partial \phi}{\partial n} \right) dS. \quad (2.14)$$

We convert to a local spherical coordinate system as prescribed in Equation 2.10 and evaluate the first term on the right-hand side of Equation 2.15 to be

$$\begin{aligned} \int_{S_{\mathbf{x}}^{\Omega}(\epsilon)} \phi(\mathbf{x}') \frac{\partial}{\partial n} G(\mathbf{x}, \mathbf{x}') \cdot dS &= \int_{S_{\mathbf{x}}^{\Omega}(\epsilon)} \phi(\mathbf{x} + \boldsymbol{\rho}) \cdot \frac{\partial}{\partial \rho} \left( \frac{1}{4\pi\rho} \right) \cdot dS = \\ &= \epsilon^2 \int_{\Omega_{\mathbf{x}}} d\Omega \cdot \phi(\mathbf{x} + \boldsymbol{\rho}) \cdot \left( -\frac{1}{4\pi\epsilon^2} \right) = \\ &= -\frac{1}{4\pi} \int_{\Omega_{\mathbf{x}}} d\Omega \cdot \phi(\mathbf{x} + \boldsymbol{\rho}), \end{aligned} \quad (2.15)$$

which, as  $\epsilon \rightarrow 0$ , approaches  $-\frac{\Omega_{\mathbf{x}}}{4\pi} \cdot \phi(\mathbf{x})$ . The second term on the right-hand side of Equation 2.13 becomes

$$\begin{aligned} \int_{S_{\mathbf{x}}^{\Omega}(\epsilon)} G(\mathbf{x}, \mathbf{x}') \frac{\partial}{\partial n} \phi(\mathbf{x}') \cdot dS &= \int_{S_{\mathbf{x}}^{\Omega}(\epsilon)} \left( \frac{1}{4\pi\rho} \right) \cdot \frac{\partial}{\partial \rho} \phi(\mathbf{x} + \boldsymbol{\rho}) \cdot dS \\ &= \frac{\epsilon}{4\pi} \int_{\Omega_{\mathbf{x}}} d\Omega \cdot \frac{\partial}{\partial \rho} (\phi(\mathbf{x} + \boldsymbol{\rho}))|_{\rho=\epsilon}, \end{aligned} \quad (2.16)$$

which tends to 0 as  $\epsilon \rightarrow 0$ , since since we are once again guaranteed that  $\frac{\partial}{\partial \rho} \phi(\mathbf{x} + \boldsymbol{\rho})$  is well-behaved by

---

<sup>§</sup>If  $\mathbf{x}$  is on a smooth contour,  $\Omega_{\mathbf{x}} = 2\pi$ . Otherwise,  $\Omega_{\mathbf{x}}$  is dependent upon the  $C^1$  discontinuity of the piecewise-continuous boundary segments that comprise  $\partial\Sigma$ .



the earlier requirement that  $\phi(\mathbf{x})$  be twice continuously differentiable. We have therefore shown that, when  $\mathbf{x} = \mathbf{x}'$ ,  $\mathbf{x} \in \partial\Sigma$ , the right-hand side of Equation 2.5 converges to  $\frac{\Omega_{\mathbf{x}}}{4\pi} \cdot \phi(\mathbf{x})$ .

#### 2.2.4: Final form of the Interior Equation

Having demonstrated that  $G(\mathbf{x}, \mathbf{x}')$  is square-integrable  $\forall \mathbf{x} \in \mathbb{R}^3$ , we now formulate an expression for the solution to the Laplace equation in  $\Sigma$  as an integral equation:

$$c(\mathbf{x}) \cdot \phi(\mathbf{x}) = \int_{\partial\Sigma} \left( \phi(\mathbf{x}') \frac{\partial G(\mathbf{x}, \mathbf{x}')}{\partial n} - G(\mathbf{x}, \mathbf{x}') \frac{\partial \phi(\mathbf{x}')}{\partial n} \right) \cdot dS, \quad (2.17)$$

$$c(\mathbf{x}) = \begin{cases} 1 & \mathbf{x} \in \Sigma \\ \frac{\Omega_{\mathbf{x}}}{4\pi} & \mathbf{x} \in \partial\Sigma \\ 0 & \mathbf{x} \notin \Sigma \end{cases} . \quad (2.18)$$

Up to this point, our derivation has held valid for the treatment for both the direct and indirect Boundary Element Methods. To proceed with a direct formalism, Equation 2.17 would be used to compute source terms given appropriate boundary conditions, and an equation would be obtained that is valid  $\forall \mathbf{x} \in \Sigma$ . With a little more manipulation, however, the indirect approach yields a much more general solution that is valid  $\forall \mathbf{x} \in \mathbb{R}^3$ .

#### 2.2.5: Extension to the Exterior Equation

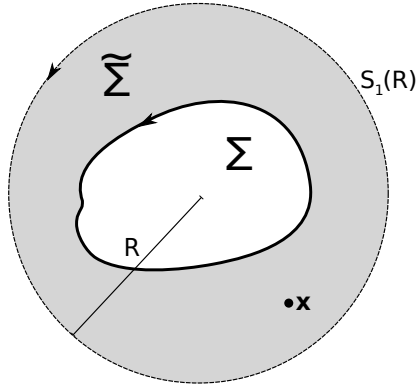


Figure 2.4: A graphical depiction of  $\tilde{\Sigma}$  in 2 dimensions.

We next apply the same formalism as in Section 2.2.2 to a region  $\tilde{\Sigma}$ , bound externally by a closed spherical shell of radius  $R$  (referred to as  $S_2(R)$ ) and internally by  $\partial\Sigma$  (see Fig. 2.4), yielding a relation analogous to

Equation 2.5 for  $\tilde{\Sigma}$ :

$$\int_{\tilde{\Sigma}} \tilde{\phi} \nabla^2 G \, dV = \int_{\partial\tilde{\Sigma}} \left( \tilde{\phi} \frac{\partial G}{\partial n} - G \frac{\partial \tilde{\phi}}{\partial n} \right) dS. \quad (2.19)$$

It is important to note that, as a consequence of the choice of boundary orientation, we have defined  $\partial\tilde{\Sigma} = S_2(R) \cup (-\partial\Sigma)$ . By requiring that

$$\lim_{|\mathbf{x}'| \rightarrow \infty} \tilde{\phi}(\mathbf{x}') = \lim_{|\mathbf{x}'| \rightarrow \infty} \left. \frac{\partial \tilde{\phi}}{\partial n} \right|_{\mathbf{x}'} = 0, \quad (2.20)$$

we can impose the condition that  $S_2(R)$  have no contribution to the right-hand side of Equation 2.19 by extending  $R \rightarrow \infty$ . Subsequent application of the procedure described in Section 2.2.3 yields the following integral equation:

$$\tilde{c}(\mathbf{x}) \cdot \tilde{\phi}(\mathbf{x}) = \int_{\partial\tilde{\Sigma}} \left( \tilde{\phi}(\mathbf{x}') \frac{\partial G(\mathbf{x}, \mathbf{x}')}{\partial n} - G(\mathbf{x}, \mathbf{x}') \frac{\partial \tilde{\phi}(\mathbf{x}')}{\partial n} \right) \cdot dS, \quad (2.21)$$

$$\tilde{c}(\mathbf{x}) = \begin{cases} 1 & \mathbf{x} \in \tilde{\Sigma} \\ 1 - \frac{\Omega_{\mathbf{x}}}{4\pi} & \mathbf{x} \in \partial\tilde{\Sigma} \setminus S_2(R) \\ 0 & \mathbf{x} \notin \tilde{\Sigma} \end{cases}, \quad (2.22)$$

and the subtended solid angle  $\Omega_{\mathbf{x}}$  has been defined earlier (see Fig. 2.3). With care to preserve the correct boundary orientations, we can rewrite Equation 2.21 in terms of our original region  $\Sigma$  and its boundary:

$$\tilde{c}(\mathbf{x}) \cdot \tilde{\phi}(\mathbf{x}) = - \int_{\partial\Sigma} \left( \tilde{\phi}(\mathbf{x}') \frac{\partial G(\mathbf{x}, \mathbf{x}')}{\partial(n)} + G(\mathbf{x}, \mathbf{x}') \frac{\partial \tilde{\phi}(\mathbf{x}')}{\partial(-n)} \right) \cdot dS \quad (2.23)$$

$$\tilde{c}(\mathbf{x}) = \begin{cases} 0 & \mathbf{x} \in \Sigma \\ 1 - \frac{\Omega_{\mathbf{x}}}{4\pi} & \mathbf{x} \in \partial\Sigma \\ 1 & \mathbf{x} \notin \Sigma \end{cases}. \quad (2.24)$$

## 2.2.6: Composing a Global Solution

We now have two distinct regions  $(\Sigma, \tilde{\Sigma})$  that share a common boundary, each with a solution function  $(\phi, \tilde{\phi})$  dependent on the properties of the boundaries of our system. With this, We can compose a global solution function  $\Phi$  that spans both regions by enforcing a boundary matching condition between our solutions. Our two choices are to enforce a relationship between  $\phi$  and  $\tilde{\phi}$  and solve for a source term  $\sigma$  defined by the discontinuities between  $\frac{\partial \phi}{\partial n}$  and  $\frac{\partial \tilde{\phi}}{\partial(-n)}$ , or to enforce a requirement on the derivatives and solve for a source term  $\mu$  defined by a discontinuity between  $\phi$  and  $\tilde{\phi}$ . The two choices result in a *single-layer potential* and *double-layer potential* formalism, respectively. We use the former prescription, since it yields a result

that extends more naturally to a physical description within the field of electrostatics.

By enforcing a  $C^0$  continuity condition between  $\phi$  and  $\tilde{\phi}$  along  $\partial\Sigma$ :

$$\phi(\mathbf{x}) = \tilde{\phi}(\mathbf{x}) \quad \forall \mathbf{x} \in \partial\Sigma, \quad (2.25)$$

and defining our globally defined composite function  $\Phi$  as

$$\Phi(\mathbf{x}) = \begin{cases} \phi(\mathbf{x}) & \mathbf{x} \in \Sigma \cup \partial\Sigma \\ \tilde{\phi}(\mathbf{x}) & \mathbf{x} \notin \Sigma \end{cases}, \quad (2.26)$$

we can add Equations 2.17 and 2.23 to obtain a global integral equation:

$$\Phi(\mathbf{x}) = - \int_{\partial\Sigma} G(\mathbf{x}, \mathbf{x}') \left( \frac{\partial\phi(\mathbf{x}')}{\partial n} + \frac{\partial\tilde{\phi}(\mathbf{x}')}{\partial(-n)} \right) \cdot dS. \quad (2.27)$$

Since we are treating the discontinuity of the derivatives at the boundary as an independent function, we can define  $\sigma(\mathbf{x}), \mathbf{x} \in \partial\Sigma$  as

$$\sigma(\mathbf{x}) = - \left( \frac{\partial\phi(\mathbf{x})}{\partial n} + \frac{\partial\tilde{\phi}(\mathbf{x})}{\partial(-n)} \right), \quad (2.28)$$

and rewrite Equation 2.27 as

$$\Phi(\mathbf{x}) = \int_{\partial\Sigma} G(\mathbf{x}, \mathbf{x}') \cdot \sigma(\mathbf{x}') \cdot dS. \quad (2.29)$$

Now that we have Equation 2.29, we need to incorporate the boundary conditions that uniquely define our solution function  $\Phi$ .

### 2.2.7: Application of Boundary Conditions

As mentioned in Section 2.2.1, our solution function  $\Phi$  is uniquely described by imposing Dirichlet, Neumann or mixed boundary conditions on the boundaries of our system. To apply a Dirichlet boundary condition, we simply restrict the domain of Equation 2.29 to our boundary:

$$\forall \mathbf{x} \in \partial\Sigma : \Phi(\mathbf{x}) = \int_{\partial\Sigma} G(\mathbf{x}, \mathbf{x}') \cdot \sigma(\mathbf{x}') \cdot dS \quad (2.30)$$

and, with  $\Phi(\mathbf{x})$  as a known function  $\forall \mathbf{x} \in \partial\Sigma$ , apply Equation 2.30 as a Fredholm equation of the first kind.

For the Neumann boundary condition, we once again restrict the domain of Equation 2.29 to our boundary, and additionally differentiate both sides with respect to the unit boundary normal at  $\mathbf{x}$ . However, we must be careful how we differentiate  $\Phi(\mathbf{x})$  on the boundary, since it is a composition of two functions defined

to have discontinuous derivatives at the boundary. Using our convention of defining the function as a limit to the boundary, we therefore obtain two different formulae for this derivative as we approach from within  $\Sigma$  or without:

$$\forall \mathbf{x} \in \partial\Sigma, \mathbf{y}^+ \in \Sigma: \left. \frac{\partial\Phi(\mathbf{x})}{\partial n} \right|_+ = \lim_{\mathbf{y}^+ \rightarrow \mathbf{x}} \frac{\partial\Phi(\mathbf{y}^+)}{\partial n} = \int_{\partial\Sigma \setminus \mathbf{x}} \frac{\partial G(\mathbf{x}, \mathbf{x}')}{\partial n} \cdot \sigma(\mathbf{x}') \cdot dS - \frac{\Omega_{\mathbf{x}}}{4\pi} \cdot \sigma(\mathbf{x}), \quad (2.31)$$

$$\forall \mathbf{x} \in \partial\Sigma, \mathbf{y}^- \notin \Sigma: \left. \frac{\partial\Phi(\mathbf{x})}{\partial n} \right|_- = \lim_{\mathbf{y}^- \rightarrow \mathbf{x}} \frac{\partial\Phi(\mathbf{y}^-)}{\partial n} = \int_{\partial\Sigma \setminus \mathbf{x}} \frac{\partial G(\mathbf{x}, \mathbf{x}')}{\partial n} \cdot \sigma(\mathbf{x}') \cdot dS + \left(1 - \frac{\Omega_{\mathbf{x}}}{4\pi}\right) \cdot \sigma(\mathbf{x}), \quad (2.32)$$

where we have adopted the convention of  $\pm$  being the limit taken along or away from the boundary normal, respectively.

With Equations 2.31 and 2.32, we can enforce a relationship between the derivatives at either side of the boundary. For example, the condition

$$\epsilon_+ \cdot \left. \frac{\partial\Phi(\mathbf{x})}{\partial n} \right|_+ = \epsilon_- \cdot \left. \frac{\partial\Phi(\mathbf{x})}{\partial n} \right|_- \quad (2.33)$$

yields the following integral equation:

$$\sigma(\mathbf{x}) = \int_{\partial\Sigma \setminus \mathbf{x}} \left( \frac{\epsilon_+ - \epsilon_-}{\frac{\Omega_{\mathbf{x}}}{4\pi} \epsilon_+ + \left(1 - \frac{\Omega_{\mathbf{x}}}{4\pi}\right) \epsilon_-} \right) \cdot \frac{\partial G(\mathbf{x}, \mathbf{x}')}{\partial n} \cdot \sigma(\mathbf{x}') \cdot dS, \quad (2.34)$$

which is a Fredholm equation of the second kind.

A mixed boundary condition is simply the discrete combination of Dirichlet and Neumann boundary conditions along  $\partial\Sigma$ . As such, we can solve problems of this type by applying Equations 2.30 and 2.34 to the Dirichlet and Neumann sections of the boundary, respectively. This is explained in more detail in Section 2.4.

### 2.2.8: Extension to Multiple Regions and Disjoint Boundaries

Although we have derived our integral equations using a single boundary enclosing a volume, this method is immediately extensible to the partitioning of space into multiple regions that share boundaries. Doing so would simply result in an integral equation for each region of space, with the requirement that the solution function be a composite of these solutions that is  $C^0$  continuous across each boundary. The final integral equations used to solve for the single-layer source terms are identical to those in the single boundary case, with an extension of our domain to include all boundaries. For example, the Dirichlet boundary integral

equation is given as

$$\forall \mathbf{x} \in \bigcup_j \partial \Sigma_j : \Phi(\mathbf{x}) = \sum_j \int_{\partial \Sigma_j} G(\mathbf{x}, \mathbf{x}') \cdot \sigma(\mathbf{x}') \cdot dS. \quad (2.35)$$

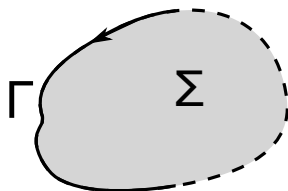


Figure 2.5: A disjoint boundary  $\Gamma$  (solid black line), and a constructed space  $\Sigma$  partially bound by  $\Gamma$ . The remaining boundary  $\partial \Sigma \setminus \Gamma$  (dashed black line) can be assigned the *null* boundary condition defined in Eq. 2.36, allowing us to apply our formalism on a closed contour.

The resulting derivation can be extended to accommodate systems with disjoint boundaries as well. To demonstrate this, we can connect disjoint boundaries with an artificial boundary that enforces a continuity of the derivatives on either side of a boundary segment:

$$\left. \frac{\partial \Phi(\mathbf{x})}{\partial n} \right|_+ = \left. \frac{\partial \Phi(\mathbf{x})}{\partial n} \right|_- . \quad (2.36)$$

It can be seen from Equations 2.31 and 2.32 that the application of this *null* condition to a boundary segment enforces that  $\sigma(\mathbf{x}) = 0$  in this region. To apply our formalism to a disjoint boundary, we can construct a space that is partially bound by a disjoint boundary, and define the remainder of its boundary to have this null boundary condition (see Fig. 2.5). In practice this is obviously not necessary; we can apply our boundary integral equations to these disjoint boundaries without any extra work.

## Section 2.3: Discretization of Fredholm Integrals for Numeric Computation

Now that we have constructed Fredholm integrals to represent the Laplace equation with both Dirichlet boundaries (Equation 2.30) and Neumann boundaries (Equation 2.34), we describe a technique for solving these equations.

### 2.3.1: Dirichlet Boundaries

We begin with a system containing only Dirichlet boundaries, represented by a Fredholm integral equation of the first kind (Equation 2.1). With no loss in generality, we can subdivide the integration interval of

Equation 2.1 so that  $\Gamma = \sum_j \Delta\Gamma_j$ , and then recast the equation as

$$f(\mathbf{x}) = \sum_j \int_{\Delta\Gamma_j} K(\mathbf{x}, \mathbf{x}') \cdot \varphi(\mathbf{x}') \cdot dS. \quad (2.37)$$

### Applying a Collocation Scheme

We approximate a solution for  $\varphi$  to second order accuracy with respect to the length scale of  $\Delta\Gamma_j$  using a *zeroth-order collocation scheme*, which approximates  $\varphi$  as a piecewise-constant function defined on our boundaries. To do this, we first use the fact that the average of a smooth function  $f(\mathbf{x})$  over a surface  $\Gamma$  is approximated to the second order of the length scale of  $\Gamma$  by its evaluation at the geometric mean of the surface (34):

$$\langle f(\mathbf{x}) \rangle_{\Gamma} \equiv \frac{1}{|\Gamma|} \cdot \int_{\Gamma} f(\mathbf{x}') \cdot dS = f(\mathbf{x}_0) + \mathcal{O}(|\Gamma|), \quad (2.38)$$

where  $|\Gamma|$  is the area measure of the surface  $\Gamma$ ,

$$\mathbf{x}_0 \equiv \frac{\int_{\Gamma} \mathbf{x}' dS}{|\Gamma|} \quad (2.39)$$

is the centroid of  $\Gamma$ , and the truncation error  $\mathcal{O}(|\Gamma|)$  scales with the square of the maximal distance of a point  $\mathbf{x} \in \Gamma$  from  $\mathbf{x}_0$ :

$$\mathcal{O}(|\Gamma|) \equiv \mathcal{O}(|\mathbf{x} - \mathbf{x}_0|^2). \quad (2.40)$$

We also note that the product of the average of two functions is equal to the average of the product of the functions to second order, since

$$\begin{aligned} \langle f(\mathbf{x}) \rangle_{\Gamma} \cdot \langle g(\mathbf{x}) \rangle_{\Gamma} &= (f(\mathbf{x}_0) + \mathcal{O}(|\Gamma|)) \cdot (g(\mathbf{x}_0) + \mathcal{O}(|\Gamma|)) = \\ &= f(\mathbf{x}_0) \cdot g(\mathbf{x}_0) + \mathcal{O}(|\Gamma|) = \\ &= \langle f(\mathbf{x}) \cdot g(\mathbf{x}) \rangle_{\Gamma} + \mathcal{O}(|\Gamma|). \end{aligned} \quad (2.41)$$

To affect our collocation scheme, we first convert the integral over  $\mathbf{x}'$  in Equation 2.37 into an average over  $\Delta\Gamma_j$ :

$$f(\mathbf{x}) = \sum_j |\Delta\Gamma_j| \cdot \langle K(\mathbf{x}, \mathbf{x}') \cdot \varphi(\mathbf{x}') \rangle_{\Delta\Gamma_j}. \quad (2.42)$$

We then expand the averaged term in Equation 2.42 using Equation 2.41:

$$\begin{aligned} f(\mathbf{x}) &= \sum_j |\Delta\Gamma_j| \cdot \left( \langle K(\mathbf{x}, \mathbf{x}') \rangle_{\Delta\Gamma_j} \cdot \langle \varphi(\mathbf{x}') \rangle_{\Delta\Gamma_j} + \mathcal{O}(|\Delta\Gamma_j|) \right) = \\ &= \sum_j |\Delta\Gamma_j| \cdot \langle K(\mathbf{x}, \mathbf{x}') \rangle_{\Delta\Gamma_j} \cdot \langle \varphi(\mathbf{x}') \rangle_{\Delta\Gamma_j} + \mathcal{O}(|\Delta\Gamma_j|^2). \end{aligned} \quad (2.43)$$

Next, we substitute an approximation to  $\langle \varphi(\mathbf{x}') \rangle_{\Delta\Gamma_j}$  as defined in Equation 2.38:

$$\begin{aligned} f(\mathbf{x}) &= \sum_j |\Delta\Gamma_j| \cdot \langle K(\mathbf{x}, \mathbf{x}') \rangle_{\Delta\Gamma_j} \cdot (\varphi(\mathbf{x}_j) + \mathcal{O}(|\Delta\Gamma_j|)) + \mathcal{O}(|\Delta\Gamma_j|^2) = \\ &= \sum_j |\Delta\Gamma_j| \cdot \langle K(\mathbf{x}, \mathbf{x}') \rangle_{\Delta\Gamma_j} \cdot \varphi(\mathbf{x}_j) + \mathcal{O}(|\Delta\Gamma_j|^2), \end{aligned} \quad (2.44)$$

where  $\mathbf{x}_j$  is the centroid of  $\Delta\Gamma_j$  as defined by Equation 2.39. Converting  $\langle K(\mathbf{x}, \mathbf{x}') \rangle_{\Delta\Gamma_j}$  back into integral form, we arrive at our collocated equation:

$$f(\mathbf{x}) = \sum_j \left( \int_{\Delta\Gamma_j} K(\mathbf{x}, \mathbf{x}') \cdot dS \right) \cdot \varphi(\mathbf{x}_j) + \mathcal{O}(|\Delta\Gamma_j|^2). \quad (2.45)$$

If we assume that,  $\forall j$ ,  $|\Delta\Gamma_j| \approx \epsilon^2$  (where  $\epsilon$  is the average length scale of our surfaces), the summation of the error terms in Equation 2.45 results in an overall collocation error of  $\mathcal{O}(\epsilon^2)$ :

$$f(\mathbf{x}) = \left[ \sum_j \left( \int_{\Delta\Gamma_j} K(\mathbf{x}, \mathbf{x}') \cdot dS \right) \cdot \varphi(\mathbf{x}_j) \right] + \mathcal{O}(\epsilon^2). \quad (2.46)$$

## Discretizing the Boundary

Equation 2.46 provides us with a means to compute field values given a piecewise-constant solution for  $\varphi$ , but we still must solve for  $\varphi$ . This is accomplished by converting Equation 2.46 into a discrete set of soluble equations, using known values of  $f(\mathbf{x})$ . The natural choice for these known field values are the centroids of  $\Delta\Gamma_i$ :

$$f(\mathbf{x}_i) = \sum_j \left( \int_{\Delta\Gamma_j} K(\mathbf{x}_i, \mathbf{x}') \cdot dS \right) \cdot \varphi(\mathbf{x}_j), \quad (2.47)$$

where the error estimate has been omitted for the sake of clarity. By affecting the following change in notation:

$$f(\mathbf{x}_i) \rightarrow f_i, \quad (2.48)$$

$$\int_{\Delta\Gamma_j} K(\mathbf{x}_i, \mathbf{x}') dS \rightarrow K_{ij}, \quad (2.49)$$

$$\varphi(\mathbf{x}_j) \rightarrow \varphi_j, \quad (2.50)$$

to Equation 2.47, we arrive at the following relation:

$$f_i = \sum K_{ij} \varphi_j, \quad (2.51)$$

in which  $\varphi_j$  can be solved using one of many computational linear algebraic techniques.

### 2.3.2: Neumann Boundaries

The procedure for the Neumann condition is analogous to that for the Dirichlet condition, applied to the Fredholm integral equation of the second kind (Equation 2.2). We discretize our region of integration:

$$\varphi(\mathbf{x}) = f(\mathbf{x}) + \lambda \sum_j \int_{\Delta\Gamma_j} K(\mathbf{x}, \mathbf{x}') \varphi(\mathbf{x}') dS, \quad (2.52)$$

apply our collocation scheme and discretize our boundary<sup>¶</sup>:

$$\varphi(\mathbf{x}_i) = f(\mathbf{x}_i) + \lambda \sum_j \left( \int_{\Delta\Gamma_j} K(\mathbf{x}_i, \mathbf{x}') \cdot dS \right) \cdot \varphi(\mathbf{x}_j), \quad (2.53)$$

and recast into a linear algebraic equation:

$$f_i = \sum K_{ij} \varphi_j, \quad (2.54)$$

where

$$\begin{aligned} f_i &= f(\mathbf{x}_i), \\ K_{ij} &= -\lambda \cdot \int_{\Delta\Gamma_j} K(\mathbf{x}_i, \mathbf{x}') dS + \delta_{ij}, \\ \varphi_j &= \varphi(\mathbf{x}_j). \end{aligned} \quad (2.55)$$

---

<sup>¶</sup>By applying the same technique as outlined in 2.3.1, it can be shown that Equation 2.53 is accurate to  $\mathcal{O}(\epsilon^2)$ .



## Section 2.4: Application of the Boundary Element Method to Laplace Integral Equations

We now have in place all of the tools required to construct the linear algebraic equation necessary to solve the Laplace equation subject to mixed boundary conditions. All that remains is to apply the technique outlined in Section 2.3 to our boundary integrals derived in Section 2.2. As before, we define the  $i$ -th discretized boundary element  $\Delta\partial\Sigma_i$  with centroid  $\mathbf{x}_i$ . Additionally, we define the set of our Dirichlet boundaries as  $\mathcal{D}$ , and the set of our Neumann boundaries as  $\mathcal{N}$ . Our final equation is then

$$f_i = \sum K_{ij}\varphi_j, \quad (2.56)$$

where

$$f_i = \begin{cases} \Phi(\mathbf{x}_i) & \Delta\partial\Sigma_i \in \mathcal{D} \\ 0 & \Delta\partial\Sigma_i \in \mathcal{N} \end{cases}, \quad (2.57)$$

$$K_{ij} = \begin{cases} \int_{\Delta\partial\Sigma_j} G(\mathbf{x}_i, \mathbf{x}') \cdot dS & \Delta\partial\Sigma_i \in \mathcal{D} \\ \left( \frac{\epsilon_+ - \epsilon_-}{\frac{\Omega_{\mathbf{x}_i}}{4\pi}\epsilon_+ + \left(1 - \frac{\Omega_{\mathbf{x}_i}}{4\pi}\right)\epsilon_-} \right) \cdot \int_{\Delta\partial\Sigma_j} \frac{\partial G(\mathbf{x}_i, \mathbf{x}')}{\partial n} \cdot dS & \Delta\partial\Sigma_i \in \mathcal{N}, i \neq j \\ 1 & \Delta\partial\Sigma_i \in \mathcal{N}, i = j \end{cases}, \quad (2.58)$$

and

$$\varphi_i = \sigma(\mathbf{x}_i). \quad (2.59)$$

Once determined, the source values  $\varphi_i$  can be inserted back into Equation 2.29 to compute field values in all space. In the electrostatic case, the formulae for numerically computing the electric potential and electric fields are

$$\Phi(\mathbf{x}) = \sum_j \left( \int_{\Delta\partial\Sigma_j} G(\mathbf{x}, \mathbf{x}') dS \right) \cdot \sigma(\mathbf{x}_j) \quad (2.60)$$

and

$$\mathbf{E}(\mathbf{x}) = - \sum_j \left( \int_{\Delta\partial\Sigma_j} \frac{\partial G(\mathbf{x}, \mathbf{x}')}{\partial n} dS \right) \cdot \sigma(\mathbf{x}_j), \quad (2.61)$$

respectively. Analytic expressions for the integrals in Equations 2.60 and 2.61 for triangle and rectangle boundary surfaces are given in Appendix A and B, respectively. Additionally, a solution profile can be incorporated into a more sophisticated field-solving technique (like fast multipole methods).

## Section 2.5: Conclusion

Given the Laplace equation and a sufficient description of a system's boundaries, we have developed a means of converting an arbitrarily complex electrostatic system into a discrete set of coupled equations whose solution provides a means to approximate our solution field to second order with respect to the length scale of our discretization. While this description is tailored to solving the electrostatic problem, this derivation can naturally be extended to solve other elliptic problems (magnetostatics and frequency-dependent electromagnetic problems, for example). Furthermore, the integral descriptions of the Laplace equation subject to different boundary conditions described here are directly applicable to other Boundary Element Method techniques (such as employing Galerkin methods in lieu of the collocation method). In the following chapters, we will construct techniques for solving these coupled equations, demonstrate the accuracy provided by this method, and describe the results of its application.

## CHAPTER 3: Robin Hood Iterative Linear Algebraic Solver

### Section 3.1: Introduction

A crucial step in implementing the Boundary Element Method (BEM) to compute charge densities for electrostatic geometry configurations is solving the linear algebraic equation

$$A\mathbf{x} = \mathbf{b} \tag{3.1}$$

for vector  $\mathbf{x}$ , where matrix  $A$  and vector  $\mathbf{b}$  are known quantities. Problems involving equations of this type are ubiquitous in all fields of computational analysis. Consequently, the study of techniques used to solve these methods is quite active and spans many fields of research. Due to the varied nature and scale of problems of this type, there is no distinct “best approach” in obtaining a solution; solvers are instead tailored to complement distinguishing properties inherent to the matrix  $A$  (exploiting such features as element density, symmetries, data management, etc.).

The technique introduced here is known as the *Robin Hood* method, described in (35), (36). The Robin Hood method is a nonstationary iterative method, named for its original implementation where the two solution elements corresponding to the most positive and most negative residual terms are simultaneously corrected at each iteration (thus “taking from the rich and giving to the poor” terms of the solution vector). The method has since been generalized to resemble a nonstationary adaptation of the *Successive Subspace Correction* (SSC) method, where the residual is iteratively minimized over subspaces of  $A$  (37).

### Section 3.2: Iterative Methods

The technique of employing an *iterative*, or *relaxation*, method to solve Equation 3.1 is theoretically straightforward: an initial guess for the solution vector  $\mathbf{x}$  is made (defined as  $\mathbf{x}^{(0)}$ ), and a transformation is continually affected on this vector until a desired accuracy is reached. In most cases where the true solution vector  $\mathbf{x}$  is not known *a priori*, the norm of the *residual*  $\mathbf{r}$ ,

$$\mathbf{r}^{(k)} = \mathbf{b} - A\mathbf{x}^{(k)}, \tag{3.2}$$

is computed to quantify the state of convergence of the system. In order to provide context for the Robin Hood method, we require some background in both stationary and nonstationary iterative methods.

### Section 3.3: Stationary Iterative Methods

Stationary methods are so named because the action performed on the solution vector  $\mathbf{x}^{(k)}$  does not vary from iteration to iteration. The *Jacobi* and *Gauss-Seidel* methods, described below, are canonical examples of stationary methods. As will be demonstrated later in this chapter, there is a direct connection between these methods and the Robin Hood method, warranting their brief description.

#### 3.3.1: Jacobi Method

The Jacobi method, as described in (38), is derived by first affecting an additive splitting on  $A$  of the form

$$A = D + L + U, \quad (3.3)$$

where  $D$  represents the diagonal elements of matrix  $A$ , and  $L$  and  $U$  represent the lower and upper triangular components of  $A$ , respectively. Equation 3.1 can then be rewritten as

$$(D + L + U)\mathbf{x} = \mathbf{b}, \quad (3.4)$$

which can be manipulated algebraically into

$$\mathbf{x} = D^{-1}(\mathbf{b} - (L + U)\mathbf{x}), \quad (3.5)$$

the classical description of the Jacobi method in matrix form. The component-wise description of Equation 3.5 is expressed as

$$x_i = \frac{1}{A_{ii}} \left( b_i - \sum_{j < i} A_{ij} x_j - \sum_{j > i} A_{ij} x_j \right). \quad (3.6)$$

Since Equation 3.6 describes a single element of  $\mathbf{x}$  in terms of the other elements of  $\mathbf{x}$ , the expression extends naturally to the recurrence relation

$$x_i^{(\kappa+1)} = \frac{1}{A_{ii}} \left( b_i - \sum_{j < i} A_{ij} x_j^{(\kappa)} - \sum_{j > i} A_{ij} x_j^{(\kappa)} \right). \quad (3.7)$$

### 3.3.2: Gauss-Seidel Method

While the Jacobi method is useful as an academic tool to introduce stationary iterative matrix solving techniques, it is rarely used; the Gauss-Seidel method is favored in practice. The implementation of the Gauss-Seidel method differs from the Jacobi method by utilizing the newly computed  $\mathbf{x}$  elements as soon as they are available, rather than after the completion of an entire iteration. This change is described mathematically by the recurrence relation

$$x_i^{(\kappa+1)} = \frac{1}{A_{ii}} \left( b_i - \sum_{j<i} A_{ij} x_j^{(\kappa+1)} - \sum_{j>i} A_{ij} x_j^{(\kappa)} \right), \quad (3.8)$$

where it is assumed that, prior to the computation of element  $x_j$ , the previous  $j - 1$  elements of  $\mathbf{x}$  have already been computed and can therefore be used to increase the accuracy of  $x_j$ . Because the estimate for  $x_j$  is improved over that of the Jacobi method, the Gauss-Seidel method comparatively reduces the number of iterations required to obtain a certain tolerance.

It is important to emphasize the aspect of element-replacement within a single iteration of the Gauss-Seidel method. The aforementioned modification to the Jacobi method introduces an implicit ambiguity in the application of the Gauss-Seidel method: the order in which the elements of  $\mathbf{x}$  are updated will produce entirely different convergence patterns for the same choice of  $A$ ,  $\mathbf{b}$  and  $\mathbf{x}^{(0)}$ .

### Section 3.4: Nonstationary Methods

In contrast to stationary methods, nonstationary methods affect adaptive algorithms to  $\mathbf{x}^{(k)}$  that are computed at each iteration. In general, nonstationary methods successively refine an initial guess  $\mathbf{x}^{(0)}$  via a repeated application of an iterative equation of the form

$$\mathbf{x}^{(k)} = \mathbf{x}^{(k-1)} + \alpha^{(k)} \mathbf{d}^{(k)}, \quad (3.9)$$

where  $\mathbf{d}^{(k)}$  is a *search vector*, and  $\alpha^{(k)}$  is the *step length* of the  $k$ -th correction. The means by which a search vector is chosen is specific to the particular nonstationary method being applied. Once a search vector is chosen, the step length is computed to minimize the norm of the projection of the  $k$ -th residual along  $\mathbf{d}^{(k)}$ :

$$\begin{aligned} \left( \mathbf{d}^{(k)} \right)^T \mathbf{r}^{(k)} &= \left( \mathbf{d}^{(k)} \right)^T \left( b - A\mathbf{x}^{(k)} \right) \\ &= \left( \mathbf{d}^{(k)} \right)^T \left( b - A \left( \mathbf{x}^{(k-1)} + \alpha^{(k)} \mathbf{d}^{(k)} \right) \right) = \\ &= \left( \mathbf{d}^{(k)} \right)^T \left( \mathbf{r}^{(k-1)} - \alpha^{(k)} A\mathbf{d}^{(k)} \right) = 0, \end{aligned} \quad (3.10)$$

or

$$\alpha^{(k)} = \frac{\left(\mathbf{d}^{(k)}\right)^T r^{(k-1)}}{\left(\mathbf{d}^{(k)}\right)^T A \mathbf{d}^{(k)}}. \quad (3.11)$$

### Section 3.5: Reinterpretation of the Gauss-Seidel Method

Though it is a stationary method, the Gauss-Seidel method can be redefined in the form of Equation 3.9. The Gauss-Seidel implementation described in Equation 3.8 is constructed by selecting the  $k$ -th search vector to be

$$\mathbf{d}^{(k)} = \mathbf{e}_{k \bmod N}, \quad (3.12)$$

where  $\mathbf{e}_i$  is the  $i$ -th canonical basis vector and  $N$  is the dimension of the matrix. Inserting Equation 3.12 into Equation 3.11 and defining  $i \equiv k \bmod N$  yields the step length

$$\alpha^{(k)} = \frac{(\mathbf{e}_i)^T r^{(k-1)}}{(\mathbf{e}_i)^T A \mathbf{e}_i}, \quad (3.13)$$

which can be inserted back into Equation 3.9 to yield the recurrence relation

$$\mathbf{x}^{(k)} = \mathbf{x}^{(k-1)} + \frac{(\mathbf{e}_i)^T r^{(k-1)}}{(\mathbf{e}_i)^T A \mathbf{e}_i} \mathbf{e}_i. \quad (3.14)$$

To show that this is equivalent to Equation 3.8, we must first note that a single  $\kappa$ -iteration in the stationary approach is equivalent to  $N$   $k$ -iterations in this nonstationary method (one sweep of the stationary Gauss-Seidel method updates every element of  $\mathbf{x}$ , whereas one sweep of the nonstationary version only updates the  $i$ -th element). As a result, during the computation of the  $(k)$ -th iteration  $\mathbf{x}^{(k)}$  has updated values  $\forall x_j^{(k)}, j < i$ , and has the same values as the prior  $(\kappa)$ -iteration  $\forall x_j^{(k)}, j \geq i$ . In other words,

$$x_j^{(k-1)} = \begin{cases} x_j^{(\kappa)} & j < i \\ x_j^{(\kappa-1)} & j \geq i \end{cases}. \quad (3.15)$$

We can then explicitly write the  $i$ -th element of  $\mathbf{x}^{(k)}$  in Equation 3.14 as follows:

$$\begin{aligned}
x_i^{(k)} &= x_i^{(k-1)} + \frac{r_i^{(k-1)}}{A_{ii}} = \\
&= x_i^{(k-1)} + \frac{1}{A_{ii}} \left( b_i - \sum_j A_{ij} x_j^{(k-1)} \right) = \\
&= x_i^{(k-1)} + \frac{1}{A_{ii}} \left( b_i - \sum_{j<i} A_{ij} x_j^{(\kappa)} - \sum_{j\geq i} A_{ij} x_j^{(\kappa-1)} \right) = \\
&= \frac{1}{A_{ii}} \left( b_i - \sum_{j<i} A_{ij} x_j^{(\kappa)} - \sum_{j>i} A_{ij} x_j^{(\kappa-1)} \right), \tag{3.16}
\end{aligned}$$

which is identical to Equation 3.8.

### Section 3.6: Generalization of the Gauss-Seidel method to a Successive Subspace Correction Method

For the description of the Gauss-Seidel method in Section 3.5, we chose our search vectors from the set of  $N$  canonical basis vectors  $\mathbf{e}_i$ ,  $i = \{1 \dots N\}$ . However, the technique of minimizing the projection of the residual is quite general. Instead of projecting our residual onto a vector, we can instead project our residual vector onto any subspace of our solution space that we desire, and iterate by minimizing the norm of its projected component. This technique is known as the Successive Subspace Correction (SSC) method, and extends the number of elements of  $\mathbf{x}^{(k)}$  that are updated during each iteration (37).

We begin by defining the  $N$ -dimensional space in which our problem lies as  $S^N$ . We then divide this space into  $\mathcal{N}$   $D$ -dimensional subspaces that span  $S^N$ , and label these subspaces  $S_i$ ,  $i = \{1 \dots \mathcal{N}\}$ . The means of selecting these subspaces is arbitrary, provided they span  $S^N$ ; for our implementation, we choose  $S_i$  to be spanned by  $D$  sequential canonical basis vectors of our problem space\* ( $S_i = \text{span}(\mathbf{e}_{D \cdot (i-1) + 1}, \dots, \mathbf{e}_{D \cdot i})$ ).

In a similar fashion to the Gauss-Seidel method, we choose our  $(k)$ -th search subspace  $S^{(k)}$  to be

$$S^{(k)} = S_{k \bmod \mathcal{N}}. \tag{3.17}$$

We define  $i \equiv k \bmod \mathcal{N}$ , and the projection matrix onto subspace  $S_i$  as  $\mathbb{P}_{S_i}$ . Once we have selected our  $k$ -th subspace  $S^{(k)}$ , we find our  $(k)$ -th search vector and step size simultaneously by enforcing that they minimize

---

\*For the sake of simplicity, we have implicitly assumed that  $D$  divides  $N$  evenly.

the norm of the projection of our residual:

$$\begin{aligned}
\mathbb{P}_{S_i} \mathbf{r}^{(k)} &= \mathbb{P}_{S_i} \left( \mathbf{b} - A \mathbf{x}^{(k)} \right) = \\
&= \mathbb{P}_{S_i} \left( \mathbf{b} - A \left( \mathbf{x}^{(k-1)} + \alpha^{(k)} \mathbf{d}^{(k)} \right) \right) = \\
&= \mathbb{P}_{S_i} \left( \mathbf{r}^{(k-1)} - A \alpha^{(k)} \mathbf{d}^{(k)} \right) = 0.
\end{aligned} \tag{3.18}$$

Solving Equation 3.18 for  $\alpha^{(k)} \mathbf{d}^{(k)}$  yields

$$\alpha^{(k)} \mathbf{d}^{(k)} = (\mathbb{P}_{S_i} A)^{-1} \mathbb{P}_{S_i} \mathbf{r}^{(k-1)}, \tag{3.19}$$

where  $(\mathbb{P}_{S_i} A)^{-1}$  is the inverse of the sub-matrix  $(\mathbb{P}_{S_i} A) \in S_i$ .

We can immediately see that, for  $D = 1$ , our search subspace reduces to the  $i$ -th canonical basis vector  $\mathbf{e}_i$ , and we recover Equations 3.12 and 3.13 for the  $k$ -th search vector and step length, respectively:

$$\begin{aligned}
\alpha^{(k)} \mathbf{d}^{(k)} &= (\mathbb{P}_{S_i} A)^{-1} \mathbb{P}_{S_i} \mathbf{r}^{(k-1)} = \\
&= \left( (\mathbf{e}_i)^T A \mathbf{e}_i \right)^{-1} \left( (\mathbf{e}_i)^T \mathbf{r}^{(k-1)} \right) \mathbf{e}_i.
\end{aligned} \tag{3.20}$$

In other words, our SSC method is merely an extension of the Gauss-Seidel method that simultaneously corrects  $D$  elements with each iteration. For higher dimensions, our  $(k)$ -th residual correction is obtained by inverting the sub-matrix  $\mathbb{P}_{S_i} A$  and applying it to the the components of the residual vector that lie in our  $(k)$ -th subspace.

The SSC method has the useful property that multiple equations are solved simultaneously. This feature can be exploited to easily apply additional constraints between elements of our system of equations that would otherwise require a complete restructuring of our matrix equation. One such example where it is useful to apply additional constraints to multiple elements simultaneously is the electrostatic case of an isolated charged surface, where charge must be macroscopically conserved across a contiguous boundary (see (36)).

### Section 3.7: Robin Hood method

With the preceding derivations in mind, we define the Robin Hood method as a non-stationary extension to the SSC method, where our  $(k)$ -th search subspace is determined adaptively using information from the  $(k-1)$ -th residual. For the  $D$ -Element Robin Hood method, we define  $\mathcal{N} = \binom{N}{D}$   $D$ -dimensional subspaces, where each subspace is defined as the span of  $D$  unique canonical basis vectors  $\mathbf{e}_i$ ,  $i \in \{1 \dots N\}$ . The  $(k)$ -th



subspace is then chosen from these  $\mathcal{N}$  subspaces to maximize the norm<sup>†</sup> of the subspace projection of the  $(k-1)$ -th residual:

$$\mathbb{P}_{S^{(k)}} \mathbf{r}^{(k-1)} = \max_j \left| \mathbb{P}_{S_j} \mathbf{r}^{(k-1)} \right|. \quad (3.21)$$

In other words, for the  $(k)$ -th iteration we choose the  $D$  canonical basis vectors that correspond to the  $D$  largest terms of the  $(k-1)$ -th residual vector, and we project our residual vector onto the subspace spanned by these  $D$  vectors. We then minimize this projection by choosing a search vector and step size as prescribed in Equation 3.19.

By exploiting our knowledge about the residual vector from the prior iteration to judiciously choose our next subspace, the Robin Hood method provides for an acceleration in convergence over the SSC method. The Robin Hood method can be construed as an effective conversion of the SSC method to a non-stationary method: while the principle equations affected in both the SSC and Robin Hood methods are identical (the minimization of the  $(k)$ -th residual norm over a subspace comprised of basis vectors of  $A$ ), the Robin Hood method incorporates prior information to adaptively select the  $(k)$ -th subspace.

For completeness, we shall restate the definition of the Robin Hood method compactly: given a linear algebraic equation

$$A\mathbf{x} = \mathbf{b} \quad (3.22)$$

where  $A$ ,  $\mathbf{b}$  are known and  $\mathbf{x}$  is unknown, the Robin Hood method is a nonstationary iterative method of the form

$$\mathbf{x}^{(k)} = \mathbf{x}^{(k-1)} + \alpha^{(k)} \mathbf{d}^{(k)} \quad (3.23)$$

where, at each iteration step, a  $D$ -dimensional subspace  $S^{(k)}$  is constructed from  $D$  unique canonical basis vectors of  $A$  that maximize the  $D$ -dimensional projection of the  $(k-1)$ -th residual onto this subspace:

$$\mathbb{P}_{S^{(k)}} \mathbf{r}^{(k-1)} = \max_j \left| \mathbb{P}_{S_j} \mathbf{r}^{(k-1)} \right|, \quad (3.24)$$

and a search vector  $\mathbf{d}^{(k)}$  and step length  $\alpha^{(k)}$  are defined with respect to this subspace as

$$\alpha^{(k)} \mathbf{d}^{(k)} = (\mathbb{P}_{S^{(k)}} A)^{-1} \mathbb{P}_{S^{(k)}} \mathbf{r}^{(k-1)} \quad (3.25)$$

to minimize this projection.

We have empirically determined that the fastest rate of convergence is obtained in the case where  $D = 1$ .

---

<sup>†</sup>It is important to note that the infinity norm is not used in Equation 3.21.

It is still useful to consider the higher-dimensional variants, however, for the aforementioned ability to apply constraints to simultaneous elements, and to justify the method’s name for the  $D = 2$  case! Pseudocode for both the 1-dimensional and  $D$ -dimensional Robin Hood technique presented in Appendix C.

### Section 3.8: Comparison of Robin Hood to Krylov Methods

It is useful to compare the Robin Hood method to *Krylov Subspace* nonstationary methods, which are more commonly used to solve equations in the form of Equation 3.1 (39). Krylov methods, for example the conjugate gradient method (and its adaptation to non-symmetric matrices, the stabilized biconjugate gradient method or *BiCGStab*), also take the form of Equation 3.9. The defining characteristic of these methods is the construction of search vectors that span the subspace formed by sequential matrix powers times the original residual,

$$K_k(A, \mathbf{r}^{(0)}) = \text{span}(\mathbf{r}^{(0)}, A\mathbf{r}^{(0)}, A^2\mathbf{r}^{(0)}, \dots, A^{k-1}\mathbf{r}^{(0)}), \quad (3.26)$$

that have the property of being orthogonal in the solution space, or *conjugate*:

$$\left(\mathbf{d}^{(i)}\right)^T A\mathbf{d}^{(j)} = 0 \forall i \neq j. \quad (3.27)$$

The conjugate nature of these search vectors yields the advantage of guaranteeing convergence in  $N$  iterations (and, in practice, usually converging in much fewer than  $N$  iterations).

While we defer the discussion of the implementation of the methods described here to Chapter 4, it is worth noting that our BEM matrix constructed in Chapter 2 is pathologically dense, asymmetric, and evaluated using only the properties of  $N$  boundary elements. As such, it is advantageous to avoid the memory constraints inherent to an explicit construction of our entire matrix, in favor of maintaining an  $\mathcal{O}[N]$  memory footprint and recomputing each element as it is required. While this approach makes feasible the scaling of our problem space to at least  $\mathcal{O}[10^6]$  dimensions (see Chapter 5), we incur the cost of computationally expensive (*i.e.* time-consuming) access to our matrix elements<sup>‡</sup>. As a result, the properties of our  $A$  matrix disfavor the use of Krylov Subspace methods due to their requirement of aggressive access to matrix elements inherent to repeated matrix-vector multiplication (each matrix-vector multiplication naively requires  $N^2$  matrix element calls). In contrast, the choice of constructing search subspaces from the canonical basis vectors of our  $A$  matrix in the Robin Hood method matches the memory access properties of our BEM implementation quite

---

<sup>‡</sup>This computational cost is mitigated to a large degree by the use of purely analytic expressions in our matrix element evaluations (see Chapters A, B), but is still far more expensive than the cost of accessing a precomputed value.

well: for each Robin Hood iteration, only  $N$  matrix element calls are performed.

### Section 3.9: Comparison of Matrix Solving Methods applied to the Spherical Capacitor

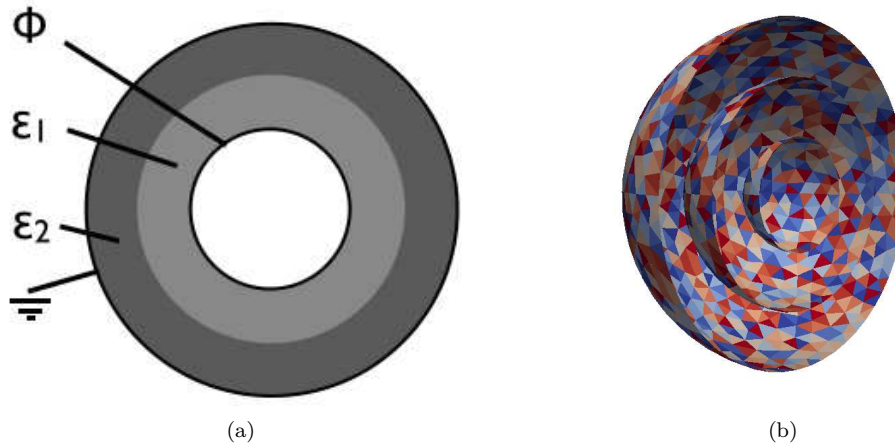


Figure 3.1: (a) A diagram of a spherical capacitor, and (b) its boundaries discretized into 4112 triangles, colored for clarity.

To compare the convergence rates of the methods described in this chapter, we compute the charge density profile for a spherical capacitor with two linear dielectric media using different levels of boundary discretization (See Figure 3.1). The three spherical boundary shells are discretized into triangular regions using Gmsh (40). As a comparison, a generic Gaussian elimination solver is also used<sup>§</sup> (39). A description of the linear algebra solvers is given in Section 4.1.3. All iterative solvers were set to compute to a residual norm of  $10^{-6}$ . At this level of precision, the predominant error of these simulations is due to discretization artifacts, rather than from the implementation of different methods (see Fig. 3.2 for a comparison of the resultant fields to their analytic counterparts). All methods were performed without parallel enhancement (i.e. using only a single thread)<sup>¶</sup>

Figure 3.3 shows a comparison of the different methods for various dimensions of matrix  $A$ , in the case where the elements of  $A$  were recomputed each time they were accessed. As expected, the single-element and 2-element Robin Hood methods show a marked improvement in performance over their stationary counterparts, the Gauss-Seidel and 2-dimensional SSC methods, respectively. It is also apparent from this figure that the BiCGStab methods show a larger dependence on the dimensionality of  $A$  than the Robin

---

<sup>§</sup>The Gaussian elimination solver must precompute the matrix elements before solving. Since it is not an iterative solver, there is no associated residual norm.

<sup>¶</sup>Computations were performed on a Mac Pro "Eight Core" 3.2 (Early 2008) with two 3.2 GHz Quad Core Intel Xeon processors.

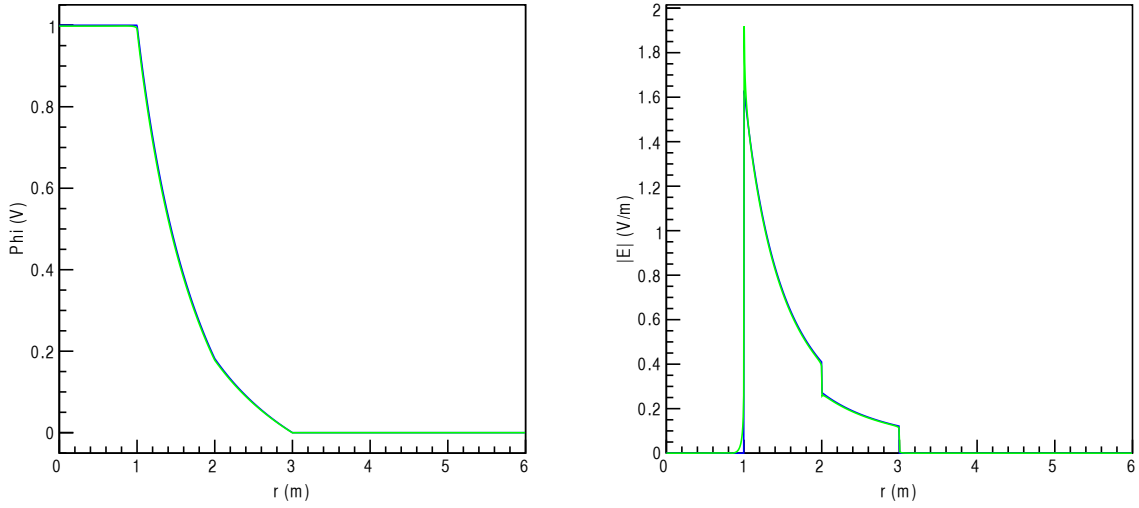
Hood method.

Figure 3.4 shows a comparison of the different methods for various dimensions of matrix  $A$ , in the case where the elements of  $A$  were precomputed prior to the solve. By precomputing the matrix elements, we remove the time-cost of accessing individual elements, allowing for a correlation of the intrinsic properties of the matrix and the efficacy of the solver. To this end, there is a marked improvement in computation time between the non-stationary and stationary methods, demonstrating the benefit of an adaptive selection of subspace refinement in Robin Hood over the Gauss-Seidel and SSC methods.

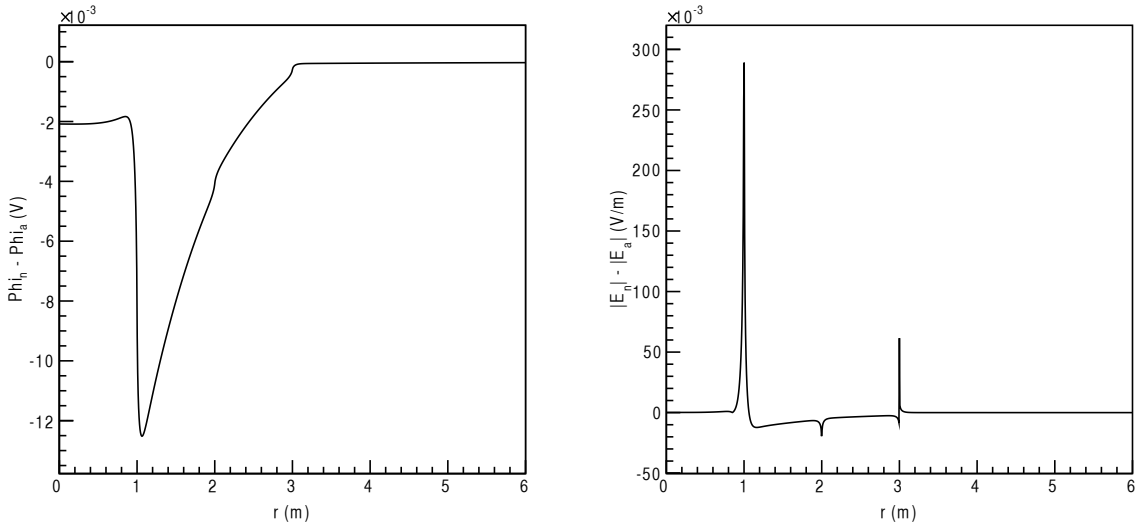
Finally, Figure 3.5 compares Robin Hood convergence times for different subspace dimensions, from  $D = 1$  to 10. A single-element Robin Hood method is also displayed; this algorithm was tailored specifically to the  $D = 1$  case. It is apparent from this figure that the advantages of simultaneously correcting multiple elements of the solution in a single iteration quickly become offset by the computational cost of inverting increasingly larger sub matrices of  $A$ .

### **Section 3.10: Conclusion**

We have derived the Robin Hood method, a technique for solving large linear algebraic equations in the form of Equation 3.1. This method was constructed by first introducing the Gauss-Seidel method, a classical stationary iterative solver. The Gauss-Seidel method was then augmented to operate over multidimensional subspaces of our problem space, thus introducing a technique known as the Successive Subspace Correction (SSC) method. Finally, the Robin Hood method was derived as a conversion of the SSC method into a nonstationary method, where a subspace that maximized the projection of the current residual was selected at each iteration. In the context of comparing the Robin Hood method to more commonly used techniques, we briefly introduced the conceptual framework of Krylov Subspace methods, highlighting their use of conjugate search vectors over the canonical basis vectors used in the Robin Hood method. By comparing the rates of convergence of these methods when applied to an archetypical implementation of our linear algebraic system (as described in Chapter 2), we have demonstrated that, when we incorporate the computational cost of recomputing matrix elements as they are needed, the Robin Hood method has the fastest rate of convergence.



(a)



(b)

Figure 3.2: Comparison of (a) analytic (blue) to computed (green) electric potential and electric field magnitude and (b) their residuals (boundaries have been discretized into 4112 triangles). While the associated charge density profile was computed using the Robin Hood method, the solutions from all solvers display similar results; the error in the computed values is dominated by discretization artifacts.

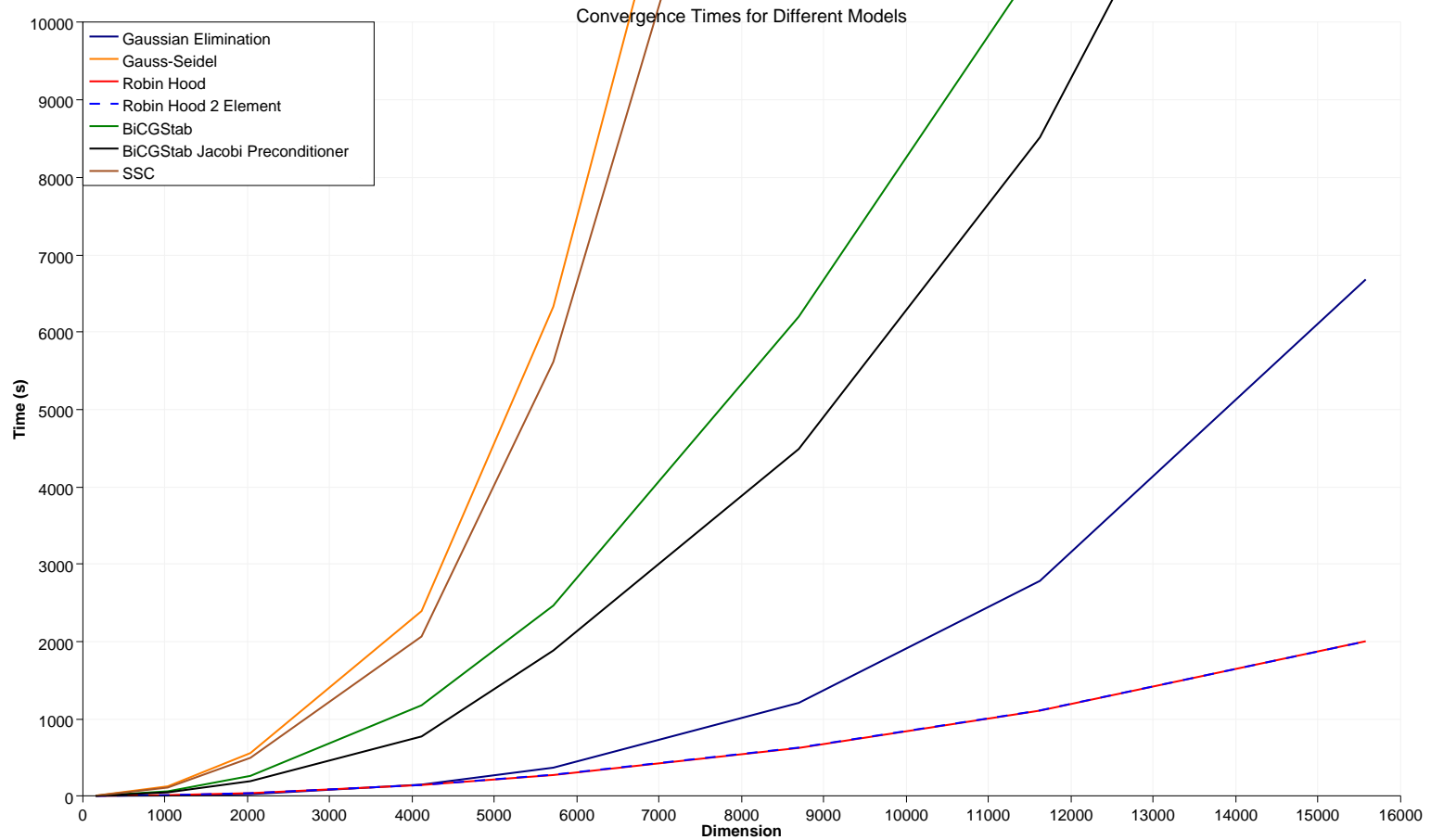


Figure 3.3: Computation time of the spherical capacitor vs dimension for several computation methods, where the elements of  $A$  are recomputed each time they were accessed. The single- and 2-element Robin Hood methods overlap with the fastest convergence times.

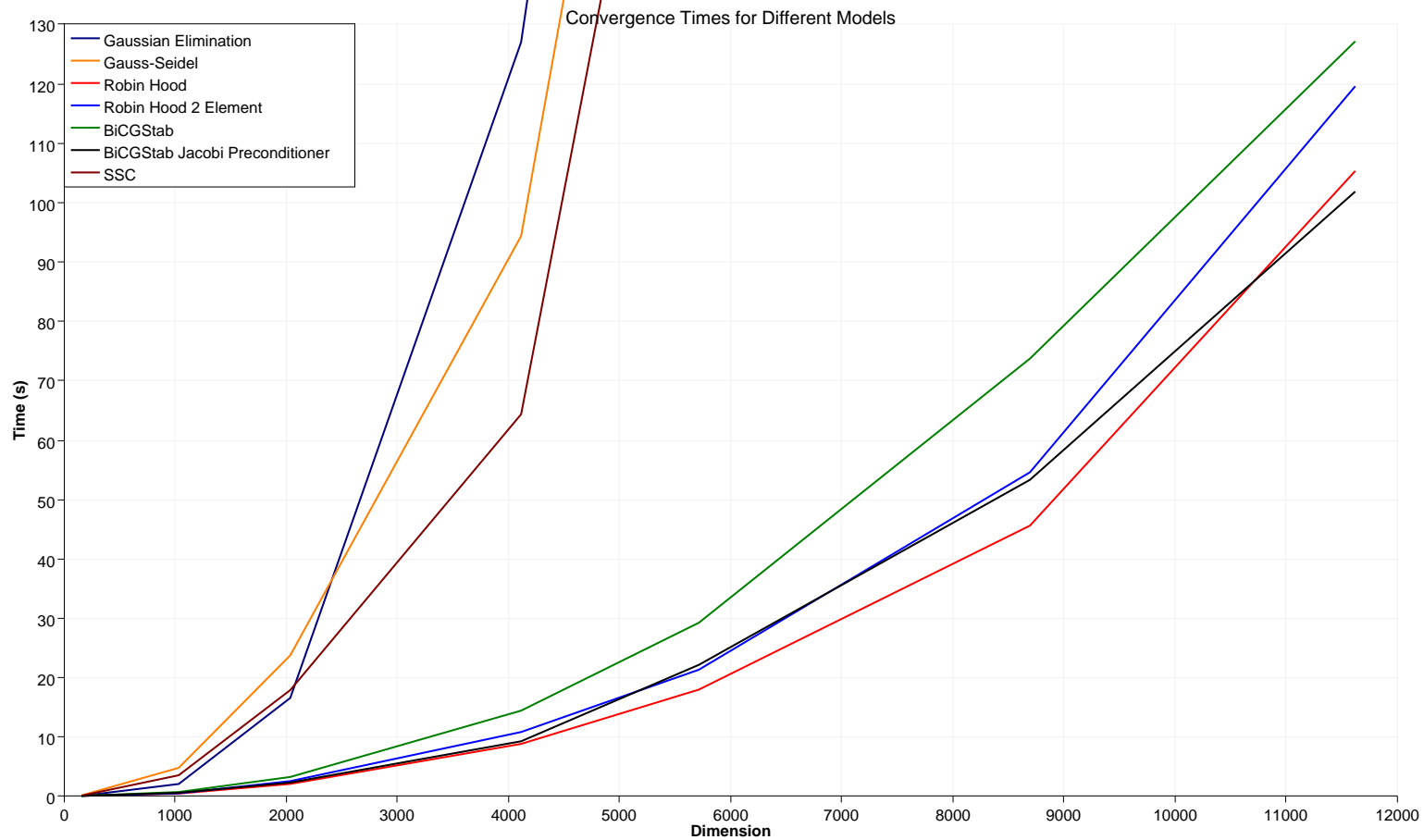


Figure 3.4: Computation time of the spherical capacitor vs dimension for several computation methods, in the case that the elements of  $A$  are precomputed prior to the solve.

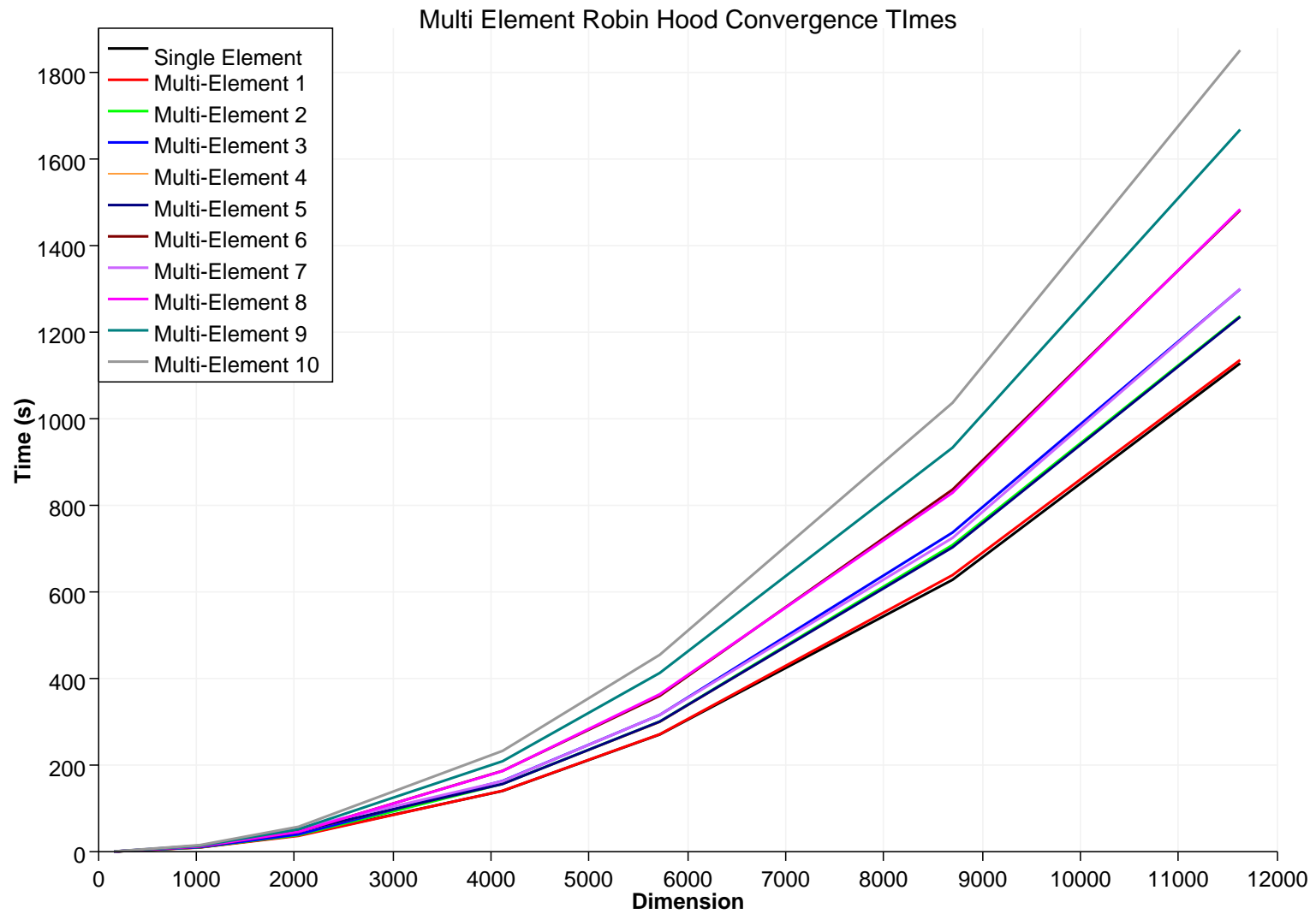


Figure 3.5: Computation time of the spherical capacitor vs dimension for different Robin Hood subspace dimensions.



## CHAPTER 4: Simulation Software

### Section 4.1: KEMFIELD: a Boundary Element Method implementation in C++

KEMFIELD is an object-oriented toolkit written in C++ that constructs and solves BEM systems by applying the techniques outlined in Chapters 2 and 3. To accomplish this, KEMFIELD is logically separated into the following tasks:

- construction and aggregate manipulation of **Surfaces**,
- execution of **Boundary Integrals** over surface elements,
- **Linear Algebra** methods for solving equations in the form of Equation 3.1,
- **Serialization** for generalized data manipulation and persistency,
- **Field Solvers** that use the results of the BEM computation to calculate fields in space,
- **External Fields** that do not rely on the BEM for generation,
- optional **Plugins** that use external libraries augment KEMFIELD's set of features, and
- **Validation** to validate and demonstrate the utility of the software.

The primary implementation of KEMFIELD is for the solution of electrostatic systems; however, the software has been designed to be extensible enough to incorporate other linear BEM systems (like magnetostatic, frequency-dependent electromagnetic and steady-state heat systems).

#### 4.1.1: Surfaces

KEMFIELD surfaces (**KSurface** elements) are composed using a policy-based design (41). Each surface is the unique composition of a basis, boundary and shape policy. Within this context, a *basis* policy defines the type of problem to be solved (e.g. electrostatic, magnetostatic, etc.), as well as the dimensionality and type associated with a 2-dimensional boundary surface (e.g. a 1 dimensional real field corresponding to an electrostatic charge density, 2 dimensional real fields corresponding to orthogonal magnetostatic surface currents, etc.). A *boundary* policy defines the type of boundary condition a surface element describes (e.g. Dirichlet, Neumann, etc.), and the values associated with this boundary condition. Finally, a *shape* policy describes the geometric representation of the surface (e.g. rectangle, triangle, etc), and its defining values.

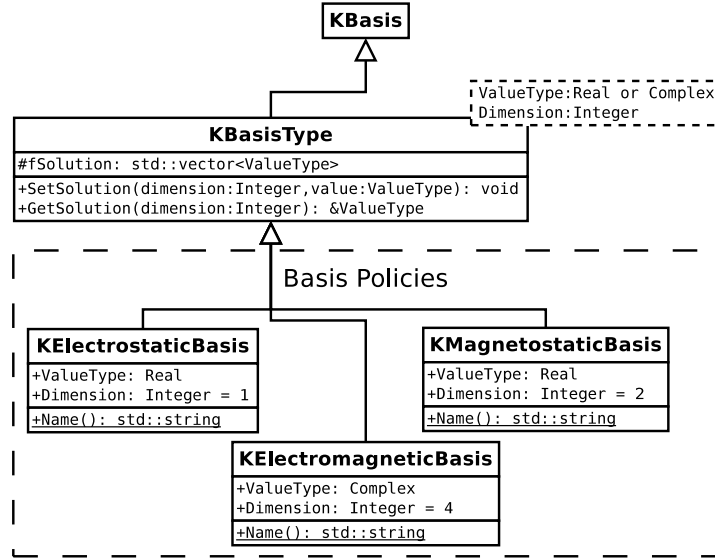


Figure 4.1: Diagram of KSurface basis policies.

The use of a policy-based design to describe surface elements allows for extensibility to other BEM-related systems and boundary types, while keeping the memory footprint of each surface element at a minimum (a feature that becomes necessary for large systems containing many surface elements).

Surfaces are stored in a surface container (`KSurfaceContainer`), a heterogeneous container optimized for element access according to surface policy type. Surface containers are ordered and provide access to their elements both by index and by iterator. In addition, by explicitly specifying surface policies, a surface container provides fast access to ordered subsets of its contents. Once constructed, `KSurfaceContainer` is the sole means of access to surface elements within `KEMFIELD`, using surfaces' base class handle `KSurfacePrimitive`, by use of the typelist visitor pattern, or directly as a Standard Template Library (STL)-style container (41).

#### 4.1.2: Boundary Integrals

Boundary Integral classes contain the methods that affect integrations over single surface elements. The requirements imposed on these classes are general by design, allowing a user to implement his or her own integration technique to compute a boundary integral. Boundary integral classes are required to define the method `BoundaryIntegral` that accepts a source surface (the surface on which the source is located), a source term index (for multidimensional sources, the index of the source dimension), and a target surface (whose centroid is the field evaluation point), and returns the value due to the indexed term of the source

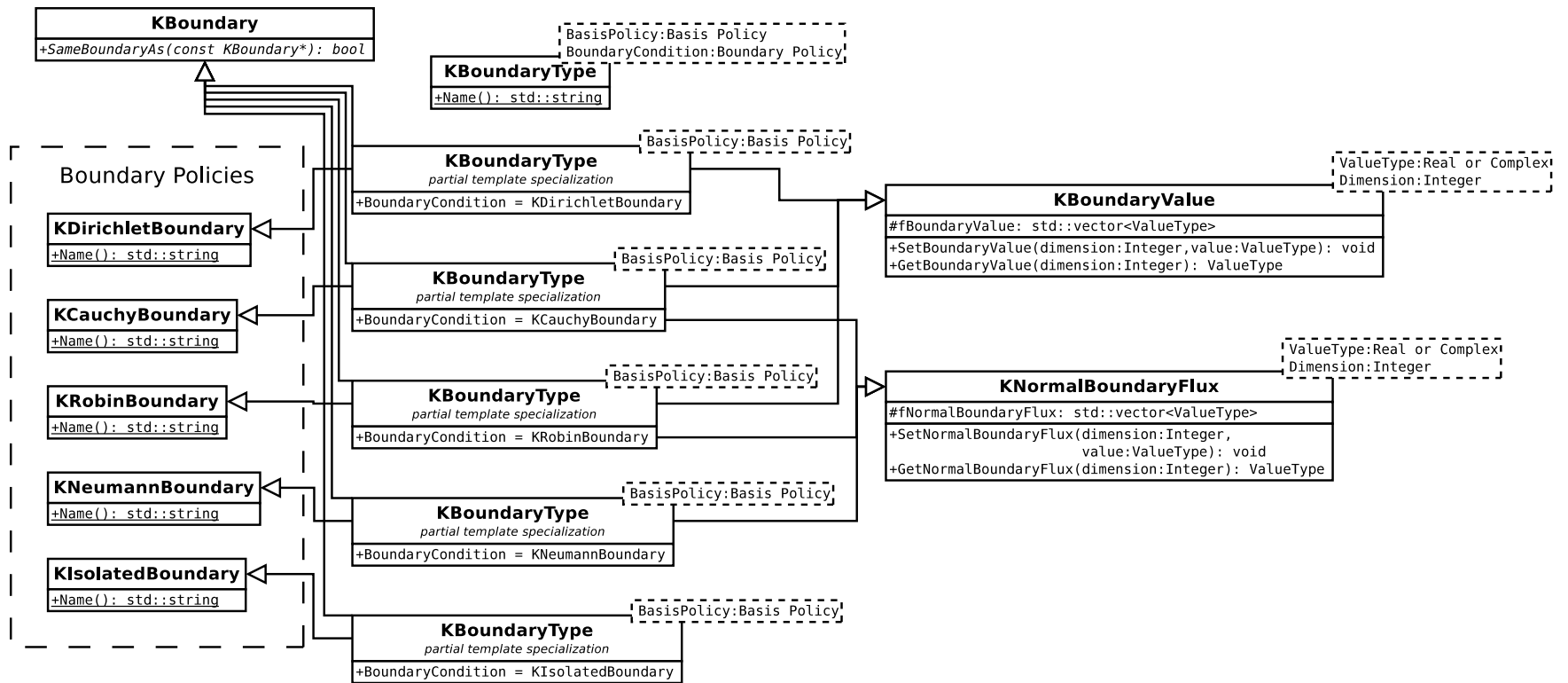


Figure 4.2: Diagram of KSurface boundary policies.

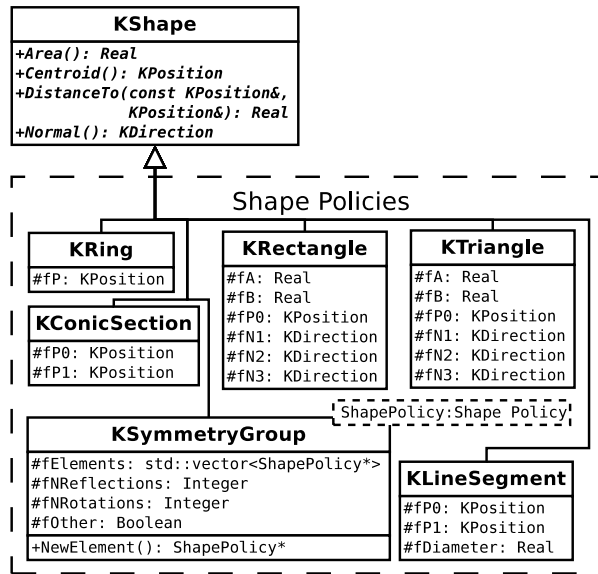


Figure 4.3: Diagram of KSurface shape policies.

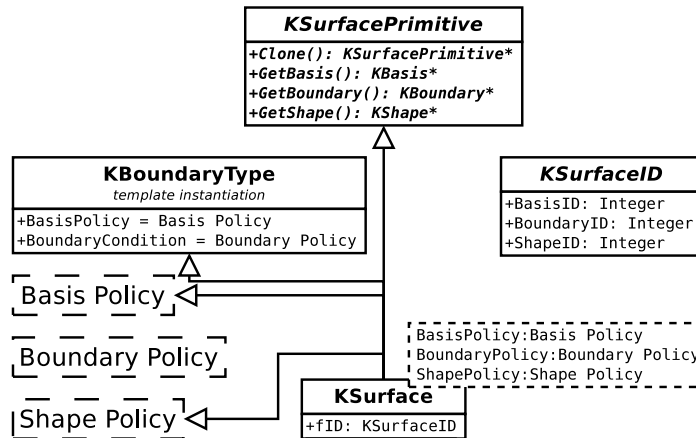


Figure 4.4: Diagram of KSurface.

surface at the target surface:

```
ValueType BoundaryIntegrator::BoundaryIntegral(KSurfacePrimitive* source,
                                                unsigned int index,
                                                KSurfacePrimitive* target);
```

Boundary integral classes must also define methods for accessing a surface's boundary and basis values corresponding to a source term index:

```
ValueType BoundaryIntegrator::BoundaryValue(KSurfacePrimitive* source,
                                             unsigned int index);
```

and

```
ValueType BoundaryIntegrator::BasisValue(KSurfacePrimitive* source,
                                          unsigned int index);
```

These methods are converted from surface-specific queries into discrete, indexed values by the classes `KBoundaryIntegralMatrix`, `KBoundaryIntegralVector`, and `KBoundaryIntegralSolutionVector`, which derive from the virtual classes `KSquareMatrix` and `KVector`, described in the following section.

#### 4.1.3: Linear Algebra

KEMFIELD's linear algebra library is used to solve the equation  $A\mathbf{x} = \mathbf{b}$  for vector  $\mathbf{x}$ , where matrix  $A$  and vector  $\mathbf{b}$  are known quantities.

#### Matrix-free implementation

The primary types used in KEMFIELD's linear algebra library are `KSquareMatrix` and `KVector`, which are abstract representations of a matrix and vector, respectively. Rather than requiring that the elements of a matrix and vector be stored explicitly, the data contained within these classes are manipulated via the virtual methods

```
ValueType KSquareMatrix::operator() (unsigned int i,
                                     unsigned int j) const;

ValueType& KVector::operator() (unsigned int i);

ValueType KSquareMatrix::Multiply(const KVector&, KVector&) const;

ValueType KSquareMatrix::MultiplyTranspose(const KVector&, KVector&) const;
```

By keeping these classes abstract, it is possible to represent large matrices while maintaining a minimal memory footprint (a so-called *matrix-free* matrix design).

## Solvers

Available linear algebraic solvers all have the method signature

```
void Solver::Solve(const KSquareMatrix& A, KVector& x, const KVector& b);
```

Additionally, iterative solvers have been designed to accept visitor classes to perform incremental state save and retrieval, and to visualize the progress of an iterative solve.

KEMFIELD has implementations for the following solvers:

- Gaussian Elimination,
- Gauss-Seidel,
- Stabilized Biconjugate Gradient method,
- Stabilized Biconjugate Gradient method with Jacobi preconditioner,
- Successive Subspace Correction method,
- Single-Element Robin Hood, and
- Multi-Element Robin Hood.

With the inclusion of the plugin for the third-party linear algebra package PETSc (see Sec. 4.1.7), the user can also use all of the linear algebraic solvers associated with the PETSc project (42).

### 4.1.4: Serialization

In order to flexibly send and receive data to and from files (a process known as *serialization*), KEMFIELD employs a templated streamer pattern. The pattern is designed to decouple the objects containing raw data from the objects that act on raw data streams. To accomplish this, each object in KEMFIELD that holds data contains methods for streaming its contents in the form of fundamental types (integers, floating point fields, etc.). In turn, the objects that accept data streams (hereafter referred to as *streamers*) need only know how to perform actions on fundamental types. For cases where a streamer's actions are dependent on a streamed object's type, a streamer has access to the object type both before and after an object is streamed.

The templated streamer pattern provides a uniform interface to all data contained by KEMFIELD objects. This access facilitates the straightforward implementation of streamers that store data to file, generate unique hashes for an object, and even manipulate data *in situ*, such as transforming a surface's coordinates, without requiring a dependency between streamers and streamed objects.

#### 4.1.5: Field Solvers

Once the BEM is performed on a discretized surface, the resulting solution is used to compute field values. Currently, fields can be computed by summing the contributions from each surface element using `KIntegratingFieldSolver`, and fields from axially symmetric systems can be computed via zonal harmonic expansion using `KZonalHarmonicFieldSolver` (43). Work is currently underway on a fast Fourier transform on multipoles (FFTM) expansion technique (44).

#### 4.1.6: External Fields

In addition to field solvers that utilize the results of a BEM computation, `KEMFIELD` uses the techniques described in Section 4.1.5 to generate fields from user-defined sources. An example of this is the use of superposition to sum the magnetostatic contribution of line currents, and the zonal harmonic expansion to compute magnetostatic fields from axially symmetric current sources (45). These *external fields* could also be used as additional terms in applying the BEM (e.g. the charge density profile of a grounded sphere in the presence of a constant electric field).

#### 4.1.7: Plugins

In order to ensure compatibility with as many computing systems as possible, the base features of `KEMFIELD` depend only on the C++ Standard Library (46). There are obvious benefits to using preexisting software to augment the feature set of `KEMFIELD`, however. Additional dependencies are therefore partitioned into optional *plugins* that can be included at compile time.

### Parallel Implementations

To facilitate the implementation of linear algebra solvers in a high performance computing environment, `KEMFIELD` uses the Message Passing Interface (MPI) to transfer information across multiple processors (47). Specifically, the Robin Hood algorithm has been optimized with MPI to distribute computation tasks within a single iteration. In conjunction with MPI, the Portable, Extensible Toolkit for Scientific Computation (PETSc) has been incorporated as an optional linear algebraic solver, providing the user with a large selection of matrix solving algorithms (42).

The compact representation of BEM matrix data and the use of analytic methods to compute matrix elements make the solution of the BEM matrix equation well-suited for computation on a graphical processing unit (GPU). To this end, `KEMFIELD` uses the OpenCL standard for GPU implementations of both the Robin Hood and Gauss-Seidel solvers, and as a parallel integrating field solver (48). A hybrid MPI and

OpenCL implementation of Robin Hood has also been developed, enabling the application of the BEM to geometries containing an excess of 5 million elements on GPU-enabled clusters (see Section 5.3).

## Visualization

KEMFIELD uses the Visualization Toolkit (VTK) to construct 3-dimensional visual models and generate field maps (49). Using VTK, models can be rendered in real-time or saved to file and analyzed off-line using ParaView (50). Additionally, the ROOT framework can be used in substitution of VTK for generating two-dimensional field maps (51).

### 4.1.8: Validation

To validate our software, we have compared the results of our computation against both analytically soluble systems and against the published results of other BEM techniques. Since our application of the BEM effectively solves for a piece-wise constant function for the charge density on our boundaries, it is straightforward to compute the capacitance  $C$  of a geometry as the sum of the computed charge of our system held at unit voltage. In other words, for a system described by Equation 2.56,

$$C = \sum_i |\partial\Sigma_i| \cdot \varphi_i, \quad (4.1)$$

where  $|\partial\Sigma_i|$  and  $\varphi_i$  are the area measure and computed charge density of the  $i$ -th boundary element, respectively.

Once a charge density profile is generated for a system, the electrostatic potential  $\Phi_n(\mathbf{x})$  and electric field  $\mathbf{E}_n(\mathbf{x})$  is computed using Equations 2.60 and 2.61, respectively, where the subscript  $n$  indicates the number of discrete boundary elements in the system\*. To obtain a numeric estimate of the accuracy of these formulae, we first define a 3-dimensional region  $D$  over which the analytic solutions  $\Phi$  and  $\mathbf{E}$  are known. We then construct an error field  $Err_n(\mathbf{x}) : \mathbb{R}^3 \rightarrow \mathbb{R}^4$ , defined as

$$(Err_n(\mathbf{x}))_i = \begin{cases} \Phi(\mathbf{x}) - \Phi_n(\mathbf{x}) & i = 0 \\ (\mathbf{E}(\mathbf{x}) - \mathbf{E}_n(\mathbf{x})) \cdot \hat{x}_i & i = 1, 2, 3 \end{cases}. \quad (4.2)$$

We then use the 2-norm and  $\infty$ -norm of the components of our error field over  $D$ , using the definitions

$$\|(Err_n)_i\|_2 \equiv \left( \frac{1}{|D|} \cdot \int_D [(Err_n(\mathbf{x}'))_i]^2 dV \right)^{\frac{1}{2}}, \quad (4.3)$$

---

\*Both MPI and OpenCL were used to compute the charge density profiles and fields in the following tests.



and

$$\|(Errr_n)_i\|_\infty \equiv \max [ |(Errr_n(\mathbf{x}'))_i| ]_{\mathbf{x}' \in D}, \quad (4.4)$$

to compute an absolute global and local error estimate of our potential and electric field, respectively. To acquire a relative global and local error estimate, we normalize our absolute error estimate using the norm of our analytic fields over  $D$ :

$$\|(Errr_n)_i\|_k^{rel} = \begin{cases} \frac{\|(Errr_n)_i\|_k}{\|\Phi\|_k} & i = 0 \\ \frac{\|(Errr_n)_i\|_k}{\|\mathbf{E} \cdot \hat{x}_i\|_k} & i = 1, 2, 3 \end{cases}. \quad (4.5)$$

Our technique for evaluating the integrals in Equation 4.3 is given in Appendix D.

## Unit Cube

While there is no analytic expression for the capacitance of the unit cube, the task of numerically estimating the capacitance has been performed by computational physicists using several techniques, including the BEM, Finite Difference Method, and Monte Carlo random walks. A current best value for the capacitance in units of  $4\pi\epsilon_0$  is given by Hwang et al. to be  $C = 0.6606782 \pm 1 \times 10^{-7}$  (52). Using KEMFIELD, we can compute this capacitance using Equation 4.1 with successively refined boundaries to gain insight into how the accuracy of our charge density profile scales with the length scale of our discretized boundary elements. We can also acquire a sense for how a parametrization of the length scales of our boundary elements can improve this scaling factor.

Figure 4.5 (a) depicts the accuracy of the KEMFIELD's capacitance measure relative to that of Hwang et al. as a function of the length scale of the discretized boundary elements in the cases where all boundary elements are subdivided into squares with equal side length. Figure 4.5 (b) depicts error values for simulations with the the same number of boundary elements as in (a), but where the length scale of the boundary elements are scaled according to the distance of a surface element to an edge of the cube. By noting the increase in the convergence slope between (a) and (b), we see that, while our zeroth-order collocation scheme provides the scaling relationship between error and element dimension, we can improve this scaling factor by a factor of  $\sim 1.9$  by judiciously dicretizing a boundary to conform to a charge density profile (in this case, applying smaller area elements to regions closer to the edges of the cube).

Inside a unit cube centered at the origin and held at unit potential, the analytic values for the potential and electric field are determined by application of Gauss' law to be  $\Phi(\mathbf{x}) = 1$  and  $\mathbf{E}(\mathbf{x}) \cdot \hat{x}_i = 0 \forall \mathbf{x} : |\mathbf{x} \cdot \hat{x}_j| < 0.5, \forall i, j \in \{1, 2, 3\}$ . Figure 4.6 depicts the global and local error estimates for  $\Phi$  and  $\mathbf{E}$ , computed using Equations 4.3 and 4.4, respectively, for the charge density profiles in Figure 4.5. As predicted in Section 2.3, Figure 4.6

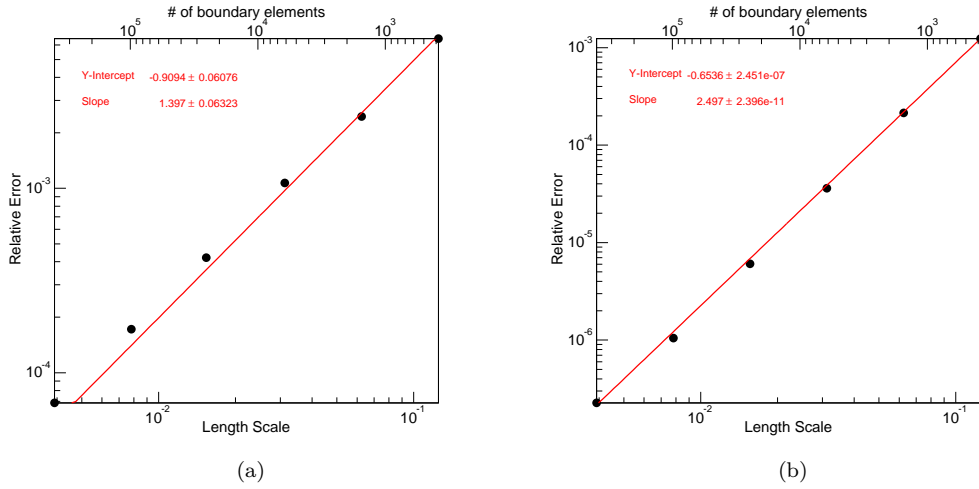


Figure 4.5: Computed error of the capacitance of the unit cube relative to Hwang et al. with discretized boundary elements that are (a) equal in measure, and (b) scaled according to a power of two near the edges of the cube. Error estimates on the electric field in (b) are omitted for length scales  $< 0.01$  due to memory overflow problems related to convergence with the adaptive integrator, but trends in the global and local error of the electric field are still identifiable.

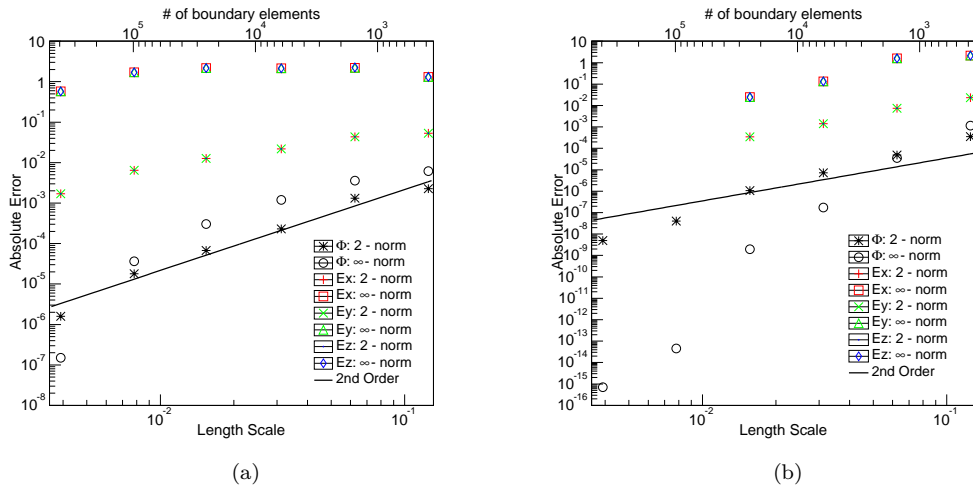


Figure 4.6: Absolute Error of the electrostatic potential and electric field for the unit cube with discretized boundary elements that are (a) equal in measure, and (b) scaled according to a power of two near the edges of the cube.

(a) shows that, with our collocation technique, the error in the global norm of the electrostatic potential for the unit cube with equal measure boundary elements is proportional to the square of the boundary length scale. In Figure 4.6 (b), we see that applying a discretization tailored to the charge density profile yields an improvement in global accuracy of the electrostatic potential of  $\sim 1.79$  (i.e. for the same number of elements, the tailored discretization is  $10^{1.79}$  more accurate than the uniform discretization). In both simulations, the local norm of the potential demonstrates a smoothing of the potential at finer length scales.

It is interesting to note that, while the global norm of the error in the electric field seems to be proportional to the boundary length scale to the first power (as expected, since the electric field is the negative gradient of the potential), the local norm of the error in the electric field is independent of length scale. This may be attributed to the effects of approximating a discontinuity at the boundary with a continuous function, resulting in an overshoot irrespective of the granularity at the boundary (this overshoot can be seen in Fig. 3.2 for the spherical capacitor).

### Spherical Capacitor

The boundary configuration for the spherical capacitor has been described in Section 3.9. This model incorporates both Dirichlet and Neumann boundary conditions, and is comprised of triangle boundary elements. Given the boundary conditions  $\Phi_0, \epsilon_1$  and  $\epsilon_2$  and the radii  $r_1 < r_2 < r_3$ , we can use Gauss' law to compute the free charge on the inner boundary  $Q_F$ , as well as the total (free and bound) charge deposited on the inner electrode  $Q_1$ , the dielectric boundary interface  $Q_2$  and the outer electrode  $Q_3$  to be

$$Q_F = 4\pi\Phi_0 \left( \frac{1}{\epsilon_2 r_2} - \frac{1}{\epsilon_2 r_3} + \frac{1}{\epsilon_1 r_1} - \frac{1}{\epsilon_1 r_2} \right)^{-1}, \quad (4.6)$$

$$Q_1 = Q_F \cdot \left( 1 - \frac{\epsilon_1 - \epsilon_0}{\epsilon_1} \right), \quad (4.7)$$

$$Q_2 = Q_F \cdot \left( \frac{\epsilon_1 - \epsilon_0}{\epsilon_1} - \frac{\epsilon_2 - \epsilon_0}{\epsilon_2} \right), \quad (4.8)$$

$$Q_3 = Q_F \cdot \left( \frac{\epsilon_2 - \epsilon_0}{\epsilon_2} - 1 \right). \quad (4.9)$$

The total charge on each boundary surface can be used to calculate the analytic potential and electric field to be

$$\Phi(\mathbf{x}) = \begin{cases} \Phi_0 & |\mathbf{x}| < r_1 \\ \frac{1}{4\pi\epsilon_0} \cdot \left( \frac{Q_2}{r_2} - \frac{(Q_1+Q_2)}{r_3} + \frac{Q_1}{|\mathbf{x}|} \right) & r_1 < |\mathbf{x}| < r_2 \\ \frac{Q_1+Q_2}{4\pi\epsilon_0} \cdot \left( \frac{1}{|\mathbf{x}|} - \frac{1}{r_3} \right) & r_2 < |\mathbf{x}| < r_3 \\ 0 & |\mathbf{x}| > r_3 \end{cases} \quad (4.10)$$

and

$$\mathbf{E}(\mathbf{x}) = \begin{cases} 0 & |\mathbf{x}| < r_1 \text{ or } |\mathbf{x}| > r_3 \\ \frac{Q_1}{4\pi\epsilon_0|\mathbf{x}|^2}\hat{\mathbf{x}} & r_1 < |\mathbf{x}| < r_2 \\ \frac{Q_1+Q_2}{4\pi\epsilon_0|\mathbf{x}|^2}\hat{\mathbf{x}} & r_2 < |\mathbf{x}| < r_3 \end{cases}. \quad (4.11)$$

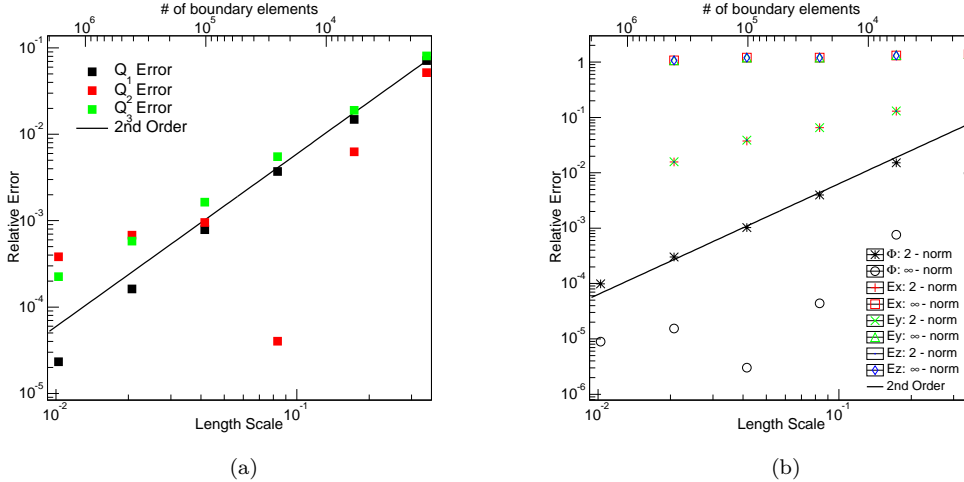


Figure 4.7: Error analysis of (a) the computed charge and (b) electrostatic potential and electric field for the spherical capacitor. Error estimates on the electric field in (b) are omitted for length scales  $< 0.02$  due to memory overflow problems related to convergence with the adaptive integrator, but trends in the global and local error of the electric field are still identifiable.

Figure 4.7 (a) depicts the relative error of the computed charge at the three boundary interfaces with respect to the length scale of the discretization, as compared to the analytic values defined in Equation 4.9. The boundary elements for these models were constructed via Delaunay triangulation using Gmsh (40). The error in the computed charge on the Dirichlet boundaries (the black and green squares in Fig. 4.7 (a)) appear to scale nearly with the square of the length scale. The error in the charge at the Neumann boundary (the red squares in the same figure) is more difficult to predict; from experience with the convergence of systems with Neumann boundaries, error estimates for Neumann boundaries tend to have a less stable convergence.

Figure 4.7 (b) depicts the relative error of the computed electrostatic potential and electric field components with respect to the length scale of the discretization, as compared to the analytic values defined in Equations 4.10 and 4.11. We see that the global norm of the error in potential scales nearly exactly with the square of the length scale, in accordance to Equation 2.46, while the global norms of the errors in the components of the electrostatic field scale with the length scale to the first power. By noting that the local error in the electric field remains constant for different length scales, we see again the invariance of the local norm of the error in electric field, owing to discontinuities at the boundary.

## Section 4.2: KGEOBAG: C++ geometry modeling software

### 4.2.1: Motivation

Now that we have a BEM solver in place, we need to provide it with discretized boundary systems. The task of constructing a navigable and discretizable geometry is deceptively tricky: one must strike a balance between a faithful representation of the system to be modeled and a generated system that is computationally approachable. Additionally, the modeling software must be sufficiently flexible to work in concert with our BEM solver, allowing for seamless integration into larger, more complex simulation software. There are many preexisting software packages designed to accomplish the goals of navigation and discretization (various CAD modeling applications, CGAL (53), and Gmsh (40), for example). After considering the implementation of an external geometry package, we were unable to find available software that provided us with the right amount of control over the generated mesh that would be easily implementable into a larger simulation framework. To solve this problem, we have constructed geometry modeling software in C++ called KGEOBAG.

### 4.2.2: Overview

KGEOBAG is a software package for designing generic 3-dimensional models for physics simulations, and has been designed around the fundamental concept of providing users with the ability to naturally extend its functionality to suit their needs by the use of extensible C++ templates. The underlying idea behind KGEOBAG is straightforward: in order to construct a model, we first decompose it into parametrically defined shapes that are geometrically easy to describe. We then provide navigation and discretization methods for each of these shapes. Finally, we compose our systems from a discrete set of these shapes, and assign user-defined information to each shape (e.g. BEM boundary type and value, visualization color, etc.). The description of the shapes, parameters and other information that comprise our system can be constructed directly in C++, or can be provided as inputs in an XML document.

The active elements of a KGEOBAG geometry are `KGSurfaces` and `KGSpaces`. Instances of these two element types are associated with one of a multitude of `KGAreas` and `KGVolumes`, respectively. Conceptually, a `KGArea` and `KGVolume` provide a description of the physical aspects of a shape, while a `KGSurface` and `KGSpace` represent the actual implementation of these shapes in a simulation. Instances of `KGSpace` and `KGSurface` can be placed within a parent `KGSpace` to form a recursive geometry tree, facilitating the construction of complex geometry assemblies while maintaining a minimal memory footprint.

An important feature of KGEOBAG that applies to its implementation as an input generator for KEM-FIELD is the method of generating surface meshes. The use of a zeroth-order collocation scheme in our

derivation of the BEM in Chapter 2 implies a constant solution value across each of our discretized elements. It is therefore critical that the size of our discretized elements conform to our solution profile. In the case of electrostatics, we know *a priori* that charge densities vary most greatly near sharp gradients in a surface's curvature (e.g. surface edges, sharp corners, etc.). The discretization of surfaces in KGEOBAG is therefore parametrized to facilitate a reduction in element size near surface edges. This provides us with tunable parameters with which we can tailor the generated mesh specifically for use in the electrostatic BEM computation.

### Section 4.3: Conclusion

KEMFIELD is a software package written in C++ designed to implement the BEM as described in Chapters 2 and 3, and subsequently compute the associated scalar and vector fields in all space. While its primary use-case is the application to electrostatic simulations, KEMFIELD exploits the extensibility of C++ templates to provide a natural extension to a broad range of BEM physics simulations. Additionally, KEMFIELD has been designed to non-intrusively incorporate third-party software to enable users to easily extend its available features. This aspect of its design is successfully demonstrated by the incorporation of hybrid CPU and GPU-enabled parallel acceleration techniques to facilitate the application of the BEM to large-scale simulations, and by the inclusion of the geometry modeling software KGEOBAG to model sophisticated problems in electrostatics. Both KEMFIELD and KGEOBAG are currently in use by the KATRIN collaboration to model the complex electrostatic and magnetostatic fields intrinsic to its mass spectrometers and detector system, described in greater detail in Chapter 5.

## CHAPTER 5: Development and Application of Simulation Software for the KATRIN Experiment

### Section 5.1: Introduction

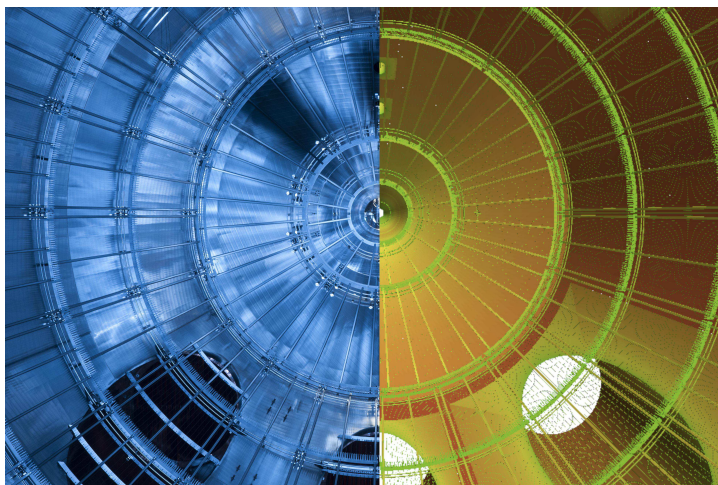


Figure 5.1: A side-by-side comparison of a photograph looking downstream inside KATRIN's main spectrometer (left) and its representation in KGEOBAG (right).

Electrostatics and magnetostatics play critical roles in the tasks of particle transport, mass spectroscopy and background suppression in the KATRIN experiment. As a consequence, we have devoted a large amount of time and effort towards acquiring a deep understanding of the electromagnetic fields throughout the entire KATRIN assembly, from both a computational and experimental viewpoint. This chapter describes some of the work that has been performed to simulate the electromagnetic fields present in KATRIN's focal plane detector (FPD) system and main spectrometer, and to understand the effects these fields may have on the efficacy of the experiment's scientific goals.

### Section 5.2: KATRIN detector region

#### 5.2.1: Overview of Electromagnetic Components

From an magnetostatic perspective, KATRIN's FPD section consists of two superconducting magnets designed to focus the incident electron beam, referred to as the *pinch* and *detector* magnets (see Fig. 5.2).

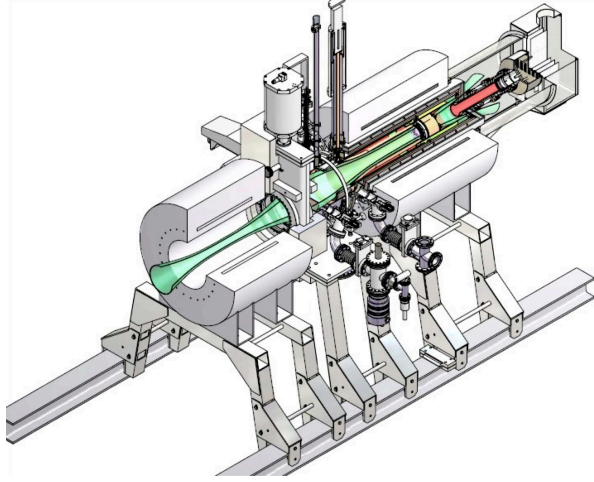


Figure 5.2: A CAD representation of the KATRIN FPD system, with the flux tube in green (4). In this orientation, the direction of the beam line is up and to the right. For a length scale, the pinch magnet (upstream) casing is 711 mm, and the detector magnet (downstream) casing is 910 mm.

The pinch magnet is located immediately downstream from the main spectrometer vessel, and acts as the refocusing magnet for this MAC-E filter (see Section 1.2.3) by producing a magnetic field of 6  $T$ . The detector magnet surrounds KATRIN’s silicon pin diode detector and, with the pinch magnet, focuses the electron beam onto the detector face by producing a magnetic field of 3.3  $T$  (with the ability to produce magnetic fields up to 6  $T$ ). By doing so, the detector magnet acts to minimize possible backgrounds due to the backscattering of incident electrons with trajectories oblique to the detector face (4).

The electrostatic fields that influence the electron beam’s trajectory in the FPD are formed by a post-acceleration system designed to translate the energy of the electrons emerging from the spectrometer into a favorable energy region for detection (see Fig. 5.2). The post-acceleration system consists of a horn-shaped electrode (this region is referred to as the *flux-tube* region; see Fig. 5.2) held at a post-acceleration potential (that can be set up to 30  $kV$ ), and three quartz cylinders coaxial to the flux-tube region and lined on both the inner and outer faces with stainless-steel electrodes. The post-acceleration horn is connected to the grounded detector base by a ceramic insulator (with a relative dielectric constant  $\epsilon_r$  of  $\sim 7$ ). The inner electrodes affixed to the quartz tubes (which have a relative dielectric constant  $\epsilon_r$  of  $\sim 3.8$ ) are held at post-acceleration potential, while the outer electrodes are fixed to ground; they are designed to prevent the formation of Penning traps in the flux-tube region (see Section 5.2.3). Additionally, a segmented silicon detector located at the center of the detector magnet bore reads the count rate and energy of our signal electrons and is held at 125  $V$  above the post-acceleration voltage. Finally, there is a pneumatic calibration system capable of inserting a disk electrode held at a user-definable electrostatic potential (from 0 to  $-20$   $kV$ ) into the beam line (4).



### 5.2.2: Electrostatic & Magnetostatic Simulation

Using KGEOBAG, we have converted a CAD model of KATRIN’s FPD system into a BEM model consisting of 40 parametrized surfaces and 5 parameterized shape types (`KG Cylinder`, `KGPortHousing`, `KGRotatedObject`, `KGExtrudedObject` and `KGGateValve`). The resulting mesh has  $\sim 450,000$  elements consisting of rectangles and triangles, whose areas are tailored to better conform to sharp curvatures in the geometry (see Fig. 5.3).

System	Technique	Hardware	Concurrency # (nodes or streams)	Wall Time (h)
Killdevil (UNC)	MPI	Intel 2.93 GHz	100	19.76
Hopper (NERSC)	MPI	Cray XE6	96	9.87
Jolokia (local)	OpenCL	ATI Radeon HD 5870	1600	8.65
Scorpion (local)	OpenCL	AMD FirePro W9000	2048	11

Table 5.1: Computation times for the charge density calculation of KATRIN’s detector section on the Killdevil cluster at UNC, the Hopper supercomputer at the National Energy Research Scientific Computing Center (NERSC), and on two local GPU-enabled workstations (Jolokia and Scorpion). On both the Killdevil and Hopper systems, MPI-parallel algorithms were used. On Jolokia and Scorpion, OpenCL-parallel algorithms were used.

To solve the linear algebraic system affiliated with a BEM implementation of the detector region, we developed the Robin Hood linear algebraic solver that is readily extendable to a cluster computing environment, and whose memory requirement scales linearly with the number of elements in the simulation (see Sec. 3.7). We then adapted this solver to utilize either cluster-based or GPU-based architectures (see Sec. 4.1.7). While both methods proved to be effective for computing the electrostatic charge density profile of the detector section (see Table 5.1 for a time comparison on different architectures), we resultantly used the GPU-based technique for our subsequent analysis, owing to the simplicity of performing a computation on a local computer with a single GPU compared to the relatively more complicated procedure inherent to the use of a dedicated computing cluster. Figure 5.4 shows the KEMFIELD-computed charge density profile and the computed electrostatic potential and magnetostatic field lines for the FPD system with the boundary conditions depicted in Figure 5.3 (a).

### 5.2.3: Penning Trap Search

#### Motivation

One use-case for an electromagnetic field simulation of the FPD system is a search for regions in our apparatus that may be susceptible to *Penning discharge*. Penning discharge occurs when a charged particle

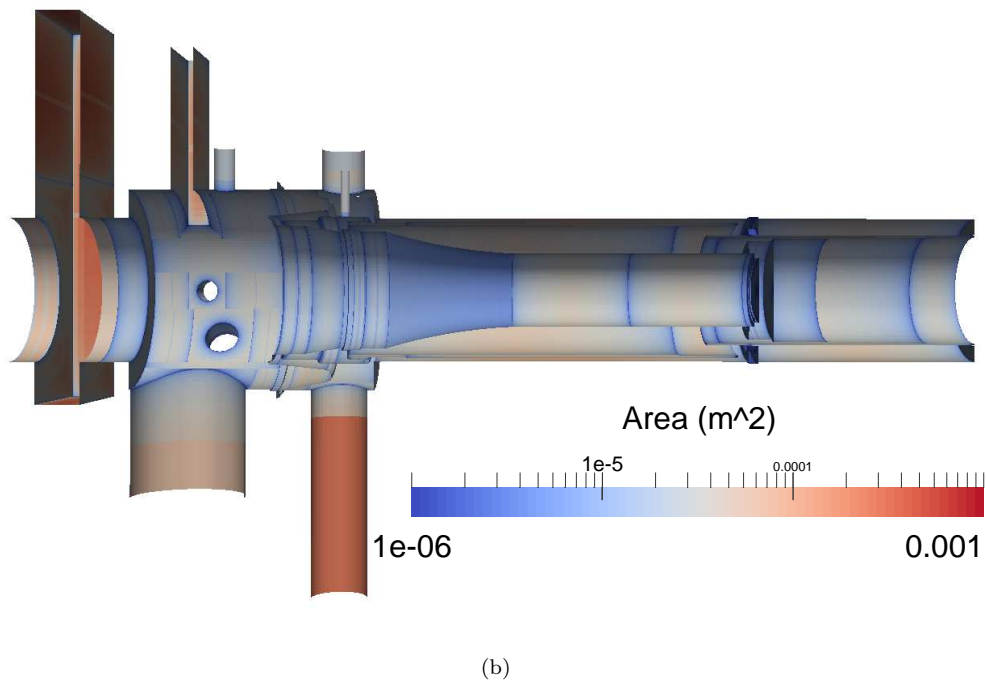
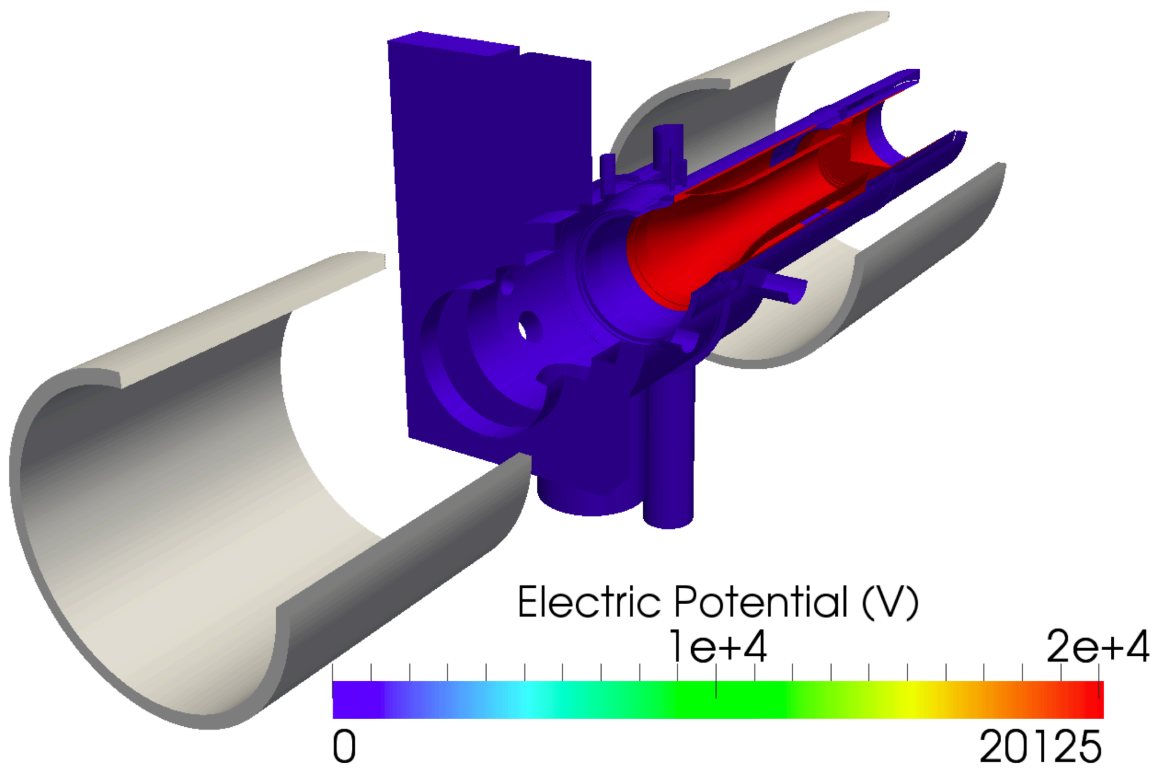
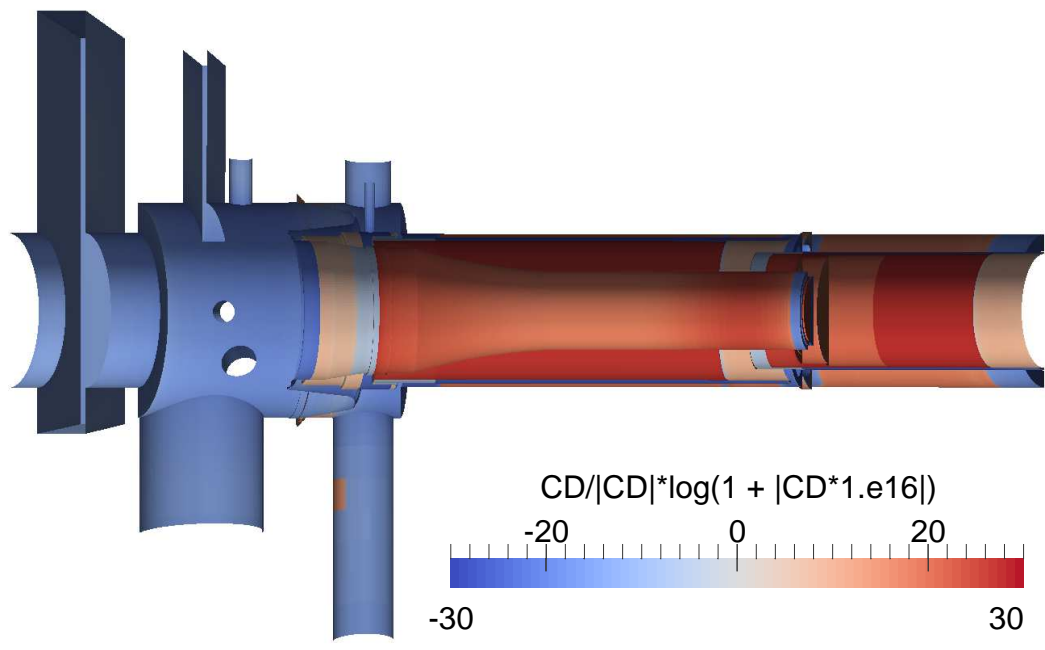
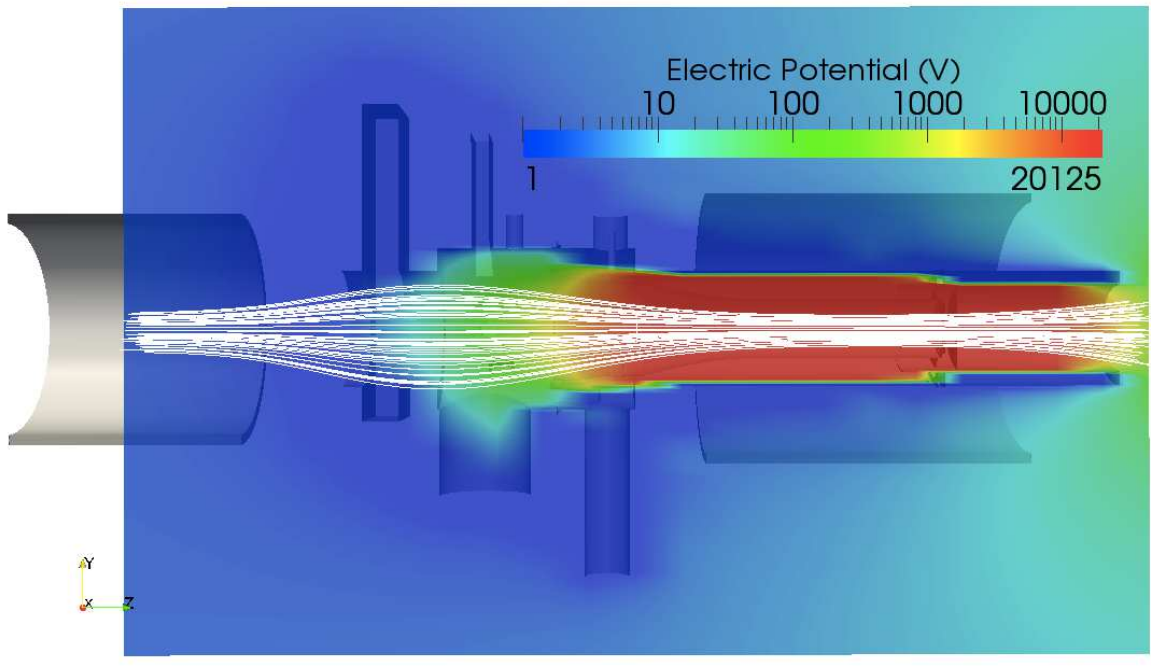


Figure 5.3: (a) A KGEOBAG representation of the KATRIN FPD system, and (b) an area measure of its discretization, colored by area. The model consists of 444,821 elements.



(a)



(b)

Figure 5.4: (a)The computed charge density (scaled to accentuate small deviations from zero) and (b) electrostatic potential (color scale) and magnetic field lines (white) in the KATRIN FPD system.

confined within a *Penning trap* (a potential well along a magnetic field line) ionizes residual gas molecules, resulting in background noise and allowing for the formation of unstable plasmas. Penning traps are a geometry-dependent phenomenon, related to the configurations of both the electromagnets and electrodes producing the magnetostatic and electrostatic fields, respectively. Since these fields can quickly become rather complex for even a simple electrode and magnet configuration and since it is difficult (and dangerous to the electronic components of the detector) to experimentally locate Penning traps, the task of identifying Penning traps is best suited to simulation. An additional requirement for the formation of stable Penning traps is that they be axially contiguous, since a secondary term in a particles' trajectory through strong electrostatic and magnetostatic fields corresponds to an axial drift (54). It is therefore efficacious to use a fully 3-dimensional model of a system instead of an axially symmetric approximation, as the latter may falsely identify axially contiguous traps that result from a geometric approximation.

## Technique

Figure 5.5 outlines the procedure for performing a Penning trap search on a toy model of the pre-spectrometer (a). We begin by voxelizing our region into a uniform grid (b). We then reject the points in our grid that are outside of our geometry (c), and keep the remaining points as *sampling points*. For each sampling point  $H$  in our system, we traverse the magnetic field line in both the upstream and downstream directions until the field line exits our system (d). We then sample the electrostatic potential along this field line (e), producing a discrete vector  $\Phi^-$  of potential values along the field line that crosses through sampling point  $H$  (the superscript on  $\Phi^-$  represents the fact that our subsequent analysis is performed on the negative values of the potential).

Now that we have a vector of negated potential values  $\Phi^-$  corresponding to sampling point  $H$  and ordered by the field sampling location on the one-dimensional magnetic field line, we can analyze this data for possible Penning traps. We begin by identifying the local minima of  $\Phi^-$  (labeled  $C$  in Table 5.5 (f)). For each local minimum, we locate the smallest neighboring local maximum  $D$ , and obtain a value for the depth of the potential well (labeled  $A$  in Table 5.5 (g)). Using the value of  $\Phi^-$  at  $D$ , we identify the points  $E$  and  $F$  on the opposing side of our identified potential well, and interpolate to obtain a second extremum and width  $B$  for the well (see Table 5.5 (h)). We omit all identified potential wells that do not contain our sampling point  $H$ , leaving us with at most one potential well corresponding to  $H$ . Finally, we compute the depth  $G$  of the potential well at our sampling point  $H$  (see Table 5.5 (i)).

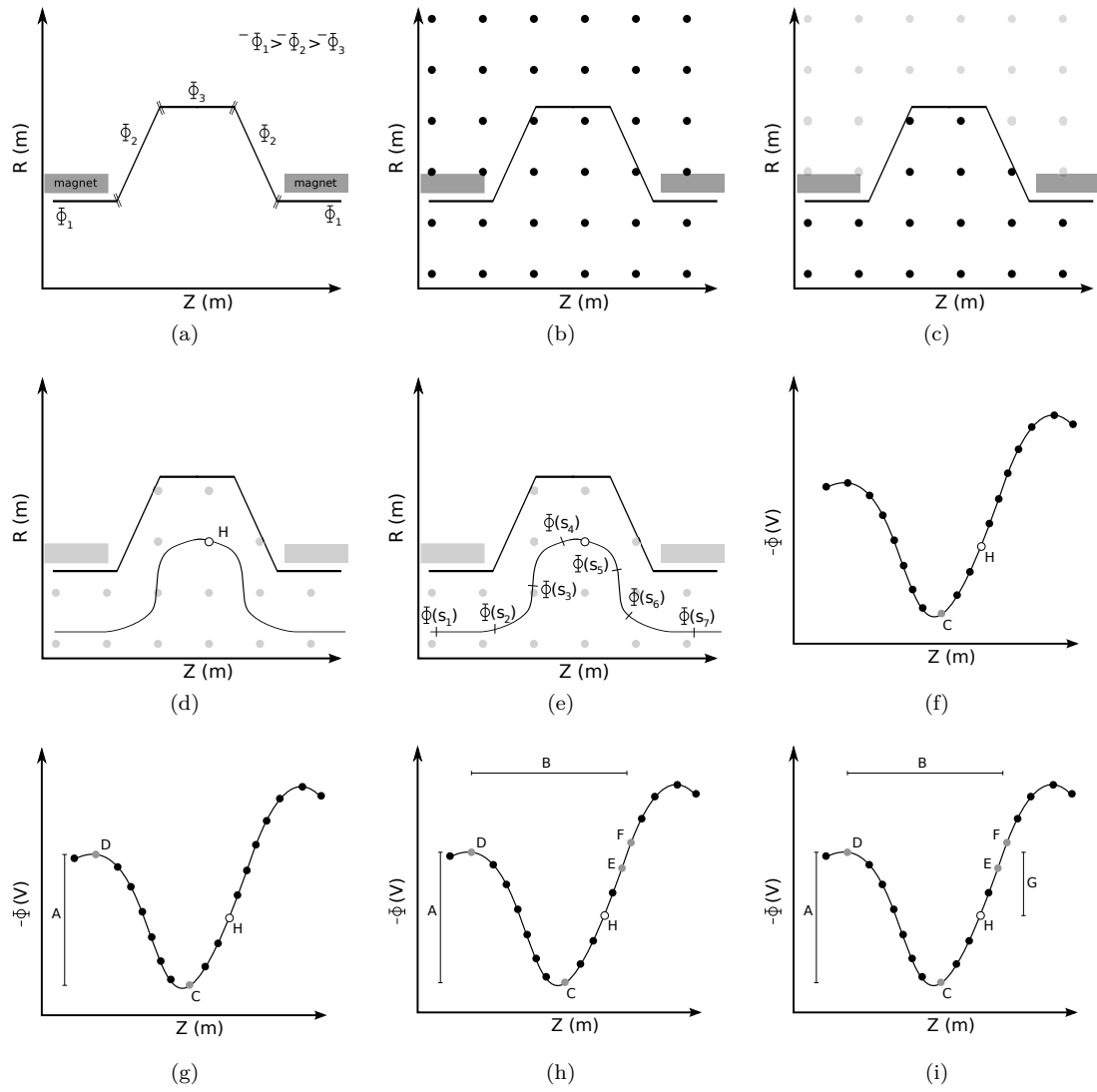
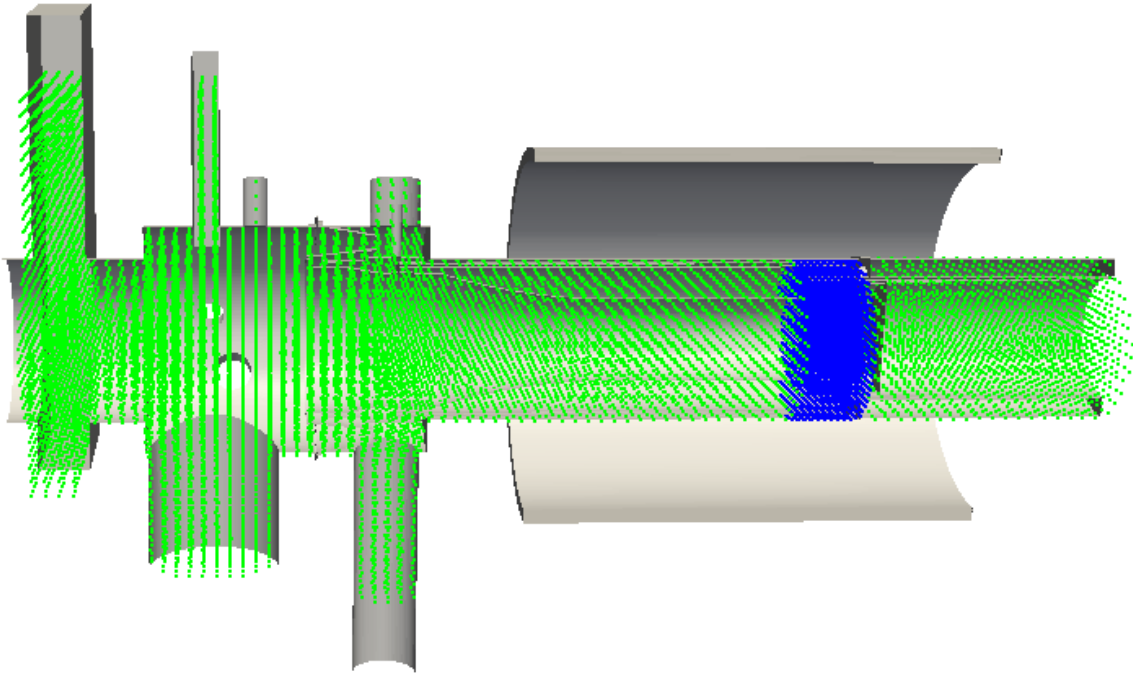
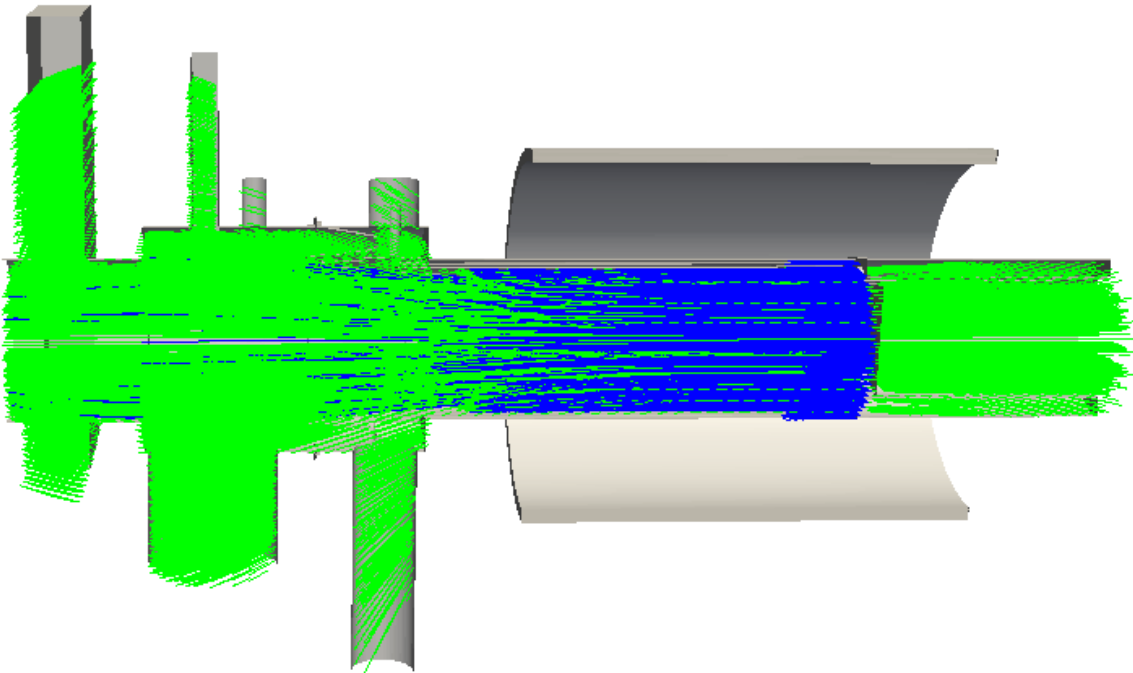


Figure 5.5: Diagrammatic representation of a Penning trap search simulation.



(a)



(b)

Figure 5.6: (a) Sampling points for a full (green) and focused (blue) Penning trap searches in the KATRIN FPD system, and (b) the field lines corresponding to these sampling points.

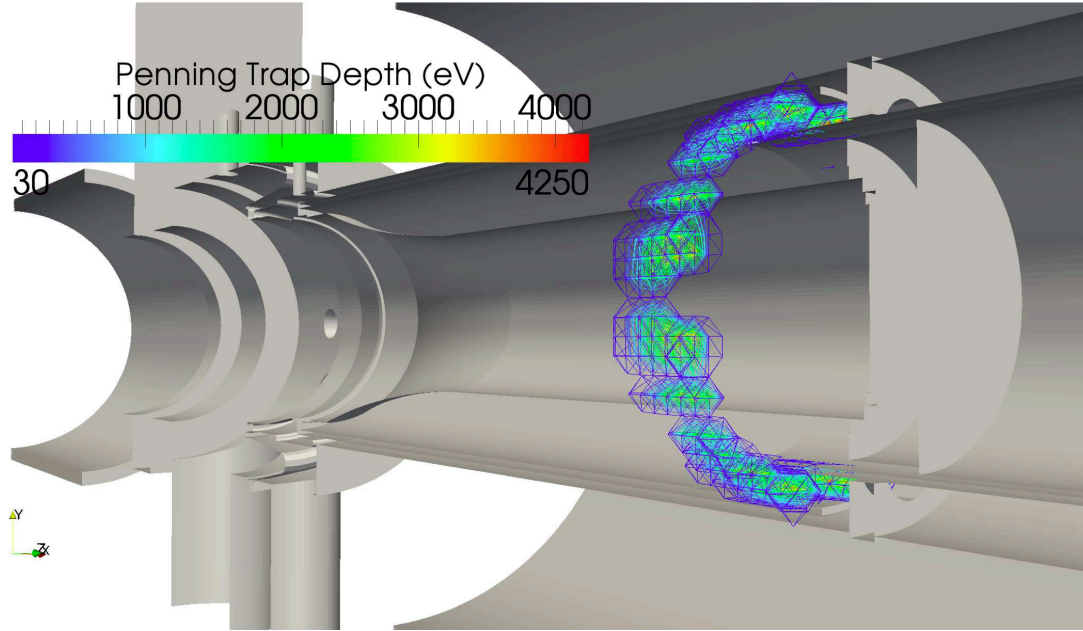


Figure 5.7: Result of a Penning trap search in the KATRIN FPD system. In this image, sampling points are assigned values according to the depth of the Penning trap at the sampling point (labeled  $G$  in Table 5.5 (i)).

## Result

By applying the aforementioned Penning trap search technique on the KATRIN FPD system, we performed a search over the entire system with  $5 \times 5 \times 5 \text{ cm}^3$  voxels, and a focused search around the detector with  $2 \times 2 \times 2 \text{ cm}^3$  voxels (see Fig. 5.6). As a result, we identified a Penning trap in the region outside of the flux tube region, resulting from radial offsets of the quartz tubes in the post-acceleration system (see Fig. 5.7). This region is isolated from the flux-tube region, and will therefore not contribute as a background to the FPD's detection efficiency. However, it has been postulated that the location and depth of the identified Penning trap may contribute to the experimentally determined limit placed on the post-acceleration voltage of  $12 \text{ kV}$ , as values above this threshold result in discharges within the apparatus (4).

## Section 5.3: KATRIN main spectrometer

### 5.3.1: Overview of Electromagnetic Components

KATRIN's main spectrometer is a MAC-E-Filter that acts as a high-pass filter on the energy spectrum of the incident electron beam. The largest electrode in the system is the spectrometer's vessel, with a maximum diameter of  $\sim 10 \text{ m}$  and a length of  $23.3 \text{ m}$  (see Fig. 5.8). The vessel is largely axially symmetric, with



Figure 5.8: A diagram of KATRIN’s main spectrometer, with superconducting magnets (green) at its entrance and exit.

the largest exception being the three large ( $\sim 0.8\text{ m}$  radius) vacuum pump ports located on the lower half of the downstream section. To produce a more axially symmetric field in the vicinity of these pump ports, the regions of intersection between the vessel and pump ports are spanned by  $5\text{ mm}$  diameter stainless steel rods (2).

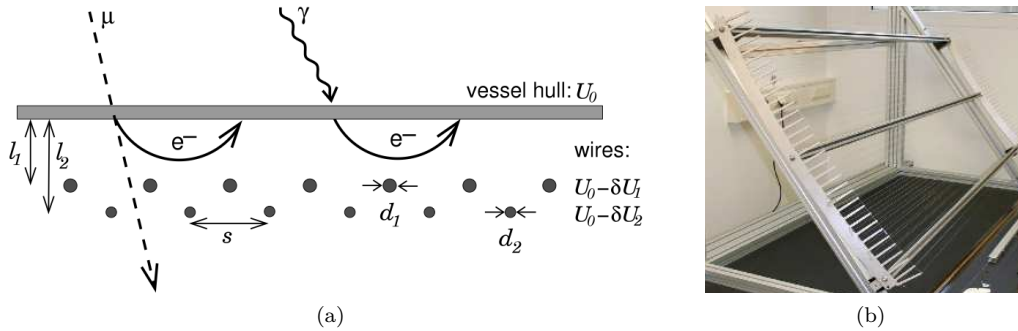


Figure 5.9: (a) A schematic of the use of wire arrays to improve background rejection in the main spectrometer (in the cylinder section of the main spectrometer:  $d_1 = 0.3\text{ mm}$ ,  $d_2 = 0.2\text{ mm}$ ,  $l_1 = 150\text{ mm}$ ,  $l_2 = 220\text{ mm}$ ,  $s = 25\text{ mm}$ ,  $\delta U_1 = 100\text{ V}$ ,  $\delta U_2 = 200\text{ V}$ ). Image from (5). (b) A photograph of one of the 248 wire modules that tile the inside of KATRIN’s main spectrometer.

The large dimensions of the main spectrometer provide for an unprecedented theoretical energy resolution for a filter of its type ( $< 1\text{ eV}$  at  $18.6\text{ keV}$ ). However, they also increase the spectrometer’s susceptibility to background electrons from the large ( $\sim 650\text{ m}^2$ ) electrode surfaces. To mitigate this source of background, the interior of the main spectrometer is lined with two concentric wire arrays, held at increasingly negative voltage with respect to the vessel (see Fig. 5.9 (a)). In addition to providing the electrostatic profile for the filtering mechanism of the spectrometer, these wire arrays create an electrostatic barrier for background electrons emitted from the vessel surface, while minimizing the additional surface area from which background electrons can be emitted.

To match the contours of the interior of the main spectrometer vessel, 148 wire modules have been installed with six different geometric profiles (referred to as the *Full Metal*, *Steep Cone*, *Small*, *Middle* &



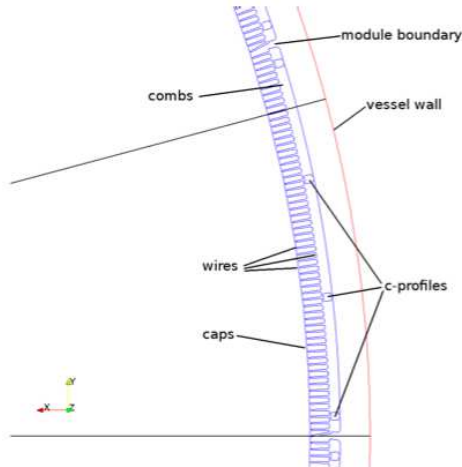


Figure 5.10: A cross-section of a wire module ring in the cylindrical section of the main spectrometer. The teeth of the wire module combs are capped by a long, narrow metal strip, labeled in this image as *caps*.

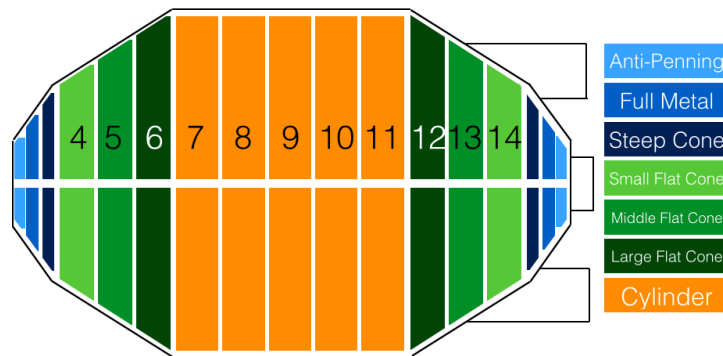


Figure 5.11: A diagram of the wire module placements (rings 2 – 16) in KATRIN’s main spectrometer.

*Large Flat Cone* and *Cylinder* wire modules). These wire modules consist of the two aforementioned wire arrays affixed to two wire combs held at the outer wire potential, which are connected by C-shaped beams (known as *C-profiles*) also held at outer wire potential. As an example, Figure 5.9 (b) is a picture of a Small Flat Cone wire module prior to installation. These wire modules have been azimuthally tiled in a ring-formation about the interior of the spectrometer vessel, and affixed to the vessel’s interior by a series of support structures held at vessel potential (see Fig. 5.1). To reduce the influence of the wire combs on the potential profile within the center of the spectrometer, the cylinder wire module rings have additional wire comb caps held at inner wire potential along the interior of the wire combs (see Fig. 5.10). The electrical connections for these wire modules are designed to be isolated between the East and West halves of the spectrometer, enabling the option for introducing a global dipole field to further reduce background particles within the spectrometer. In addition to the wire modules, the main spectrometer has conically shaped solid

electrodes at its entrance and exit (referred to as the *Ground* and *Anti-Penning* electrodes), designed to create a reference potential for the filter, and to prevent the formation of Penning traps in these regions of strong magnetic field, respectively.

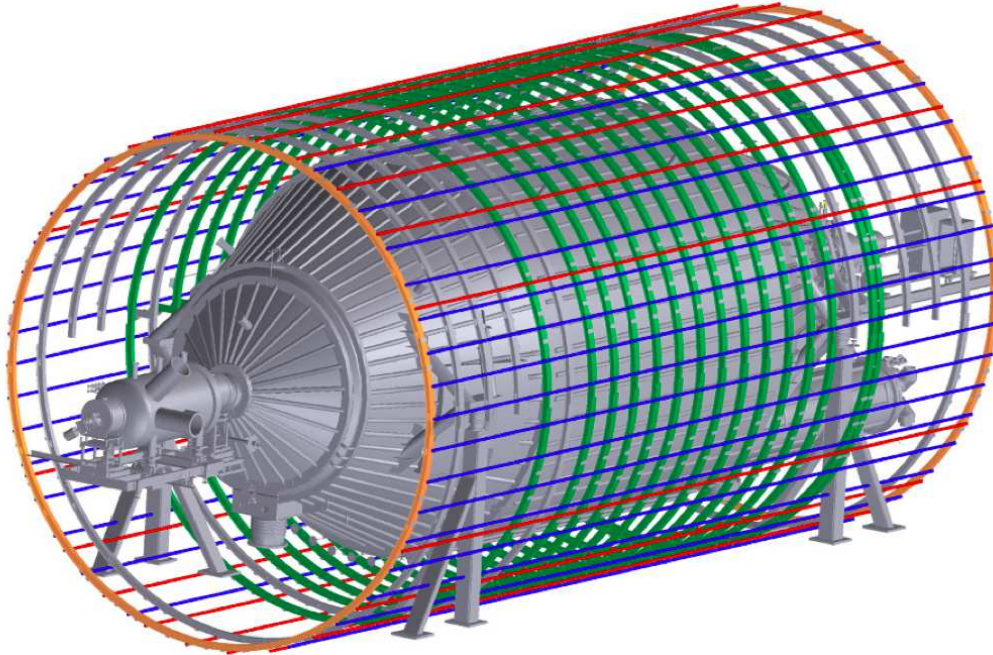


Figure 5.12: A diagram of KATRIN’s main spectrometer with the air coil system. The green air coils represent the low field correction system (LFCS), and the blue, red and orange air coils denote the elements that comprise the Earth magnetic field compensation system (EMCS). Image from (6).

The magnetostatic components of the main spectrometer consist of a superconducting magnet at either end of the spectrometer (the green components in Fig. 5.8), which produce the maximal magnetic field (up to  $6\text{ T}$ ) for MAC-E-Filtering. Additionally, the low field correction system (LFCS, colored green in Fig. 5.12) consists of 14 air coils coaxial to the spectrometer’s primary axis, and affects the axially symmetric magnetic field by providing finer control of the shape of the flux tube within the spectrometer. Finally, the Earth magnetic field compensation system (EMCS, colored blue, red and orange in Fig. 5.12) counteracts the magnetic field of the Earth (6).

### 5.3.2: Electrostatic & Magnetostatic Simulation

Using KGEOBAG, we have constructed a BEM model of KATRIN’s main spectrometer from its representation in CAD. The model contains 2166 parametrized surfaces and 9 parametrized surface types (KGCylinder, KGRotatedObject, KGExtrudedObject, KGPortHousing, KGConicSectPortHousing, KGRod, KGWireComb, KGWireArray and KGBeam). The generated mesh associated with this model is comprised of



$\sim 5M$  elements consisting of primitive shapes (rectangles, triangles and line segments) whose areas are tailored to better conform to sharp curvatures in the geometry (see Fig. 5.13).

It is important to accurately model the main spectrometer’s wire modules because of their primary role in setting the electrostatic potential within the spectrometer, and due to the axially asymmetric artifacts they may impart on the electrostatic field. To reproduce the complex structure of the wire combs in these modules, we modified *dxflib*, open-source C++ software designed to interpret geometries represented in AutoCad’s Drawing Exchange Format (DXF), to generate KGEOBAG surfaces (55). Figure 5.16 depicts the results of this technique on the six wire module types.

System	Technique	Hardware	Concurrency # (nodes or streams)	Problem Dimension	Wall Time (h)
Scorpion (local)	GPU	AMD FirePro W9000	2048	3.5 $M$	213
Killdevil (UNC)	Cluster & GPU	Intel 2.93 GHz & Nvidia M2070	$8 \times 448$	5 $M$	104

Table 5.2: Computation times for the charge density calculation of KATRIN’s main spectrometer on the GPU-enabled nodes of the Killdevil cluster at UNC, and on a local GPU-enabled workstation. On the Killdevil system, a hybrid MPI & GPU-parallel algorithm was used. On Scorpion, OpenCL-parallel algorithms were used.

Compared to that of the detector section, the linear algebraic system that results from the application of the BEM to the main spectrometer is an order of magnitude larger in dimension. To accommodate a large, dense system of this type, we developed a hybrid GPU and cluster-parallel Robin Hood linear algebraic solving algorithm (see Sec. 4.1.7). This new algorithm combines the hardware-acceleration and massive parallelism inherent to GPU calculations with the scalability and distributed memory paradigm of a dedicated cluster, facilitating the computation of the main spectrometer’s charge density profile on a GPU-enabled computer cluster (like UNC’s Killdevil cluster) in about three days of wall time (as opposed to the  $\mathcal{O}$ [weeks] predicted wall time of a supercomputer). Table 5.2 describes hardware configurations and wall times that contrast the GPU-parallel algorithm to the hybrid GPU & cluster-parallel algorithm on two different architectures. A pictorial result of a computation of the main spectrometer’s charge density profile is given in Figure 5.14.

### 5.3.3: Electrical Short Circuit Studies

One of the steps for preparing the main spectrometer for commissioning involved performing a bake-out of the spectrometer, where the vessel is heated to remove impurities on its surface. An accidental consequence of this bake-out was the formation of short circuits between wire module rings, and between wire arrays within



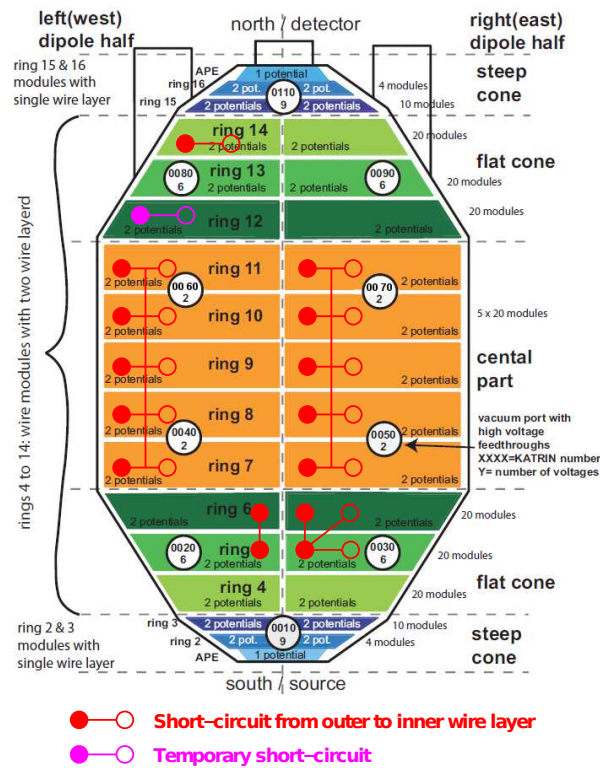


Figure 5.15: Diagram of the short circuits that resulted from bake-out. Image from (7).

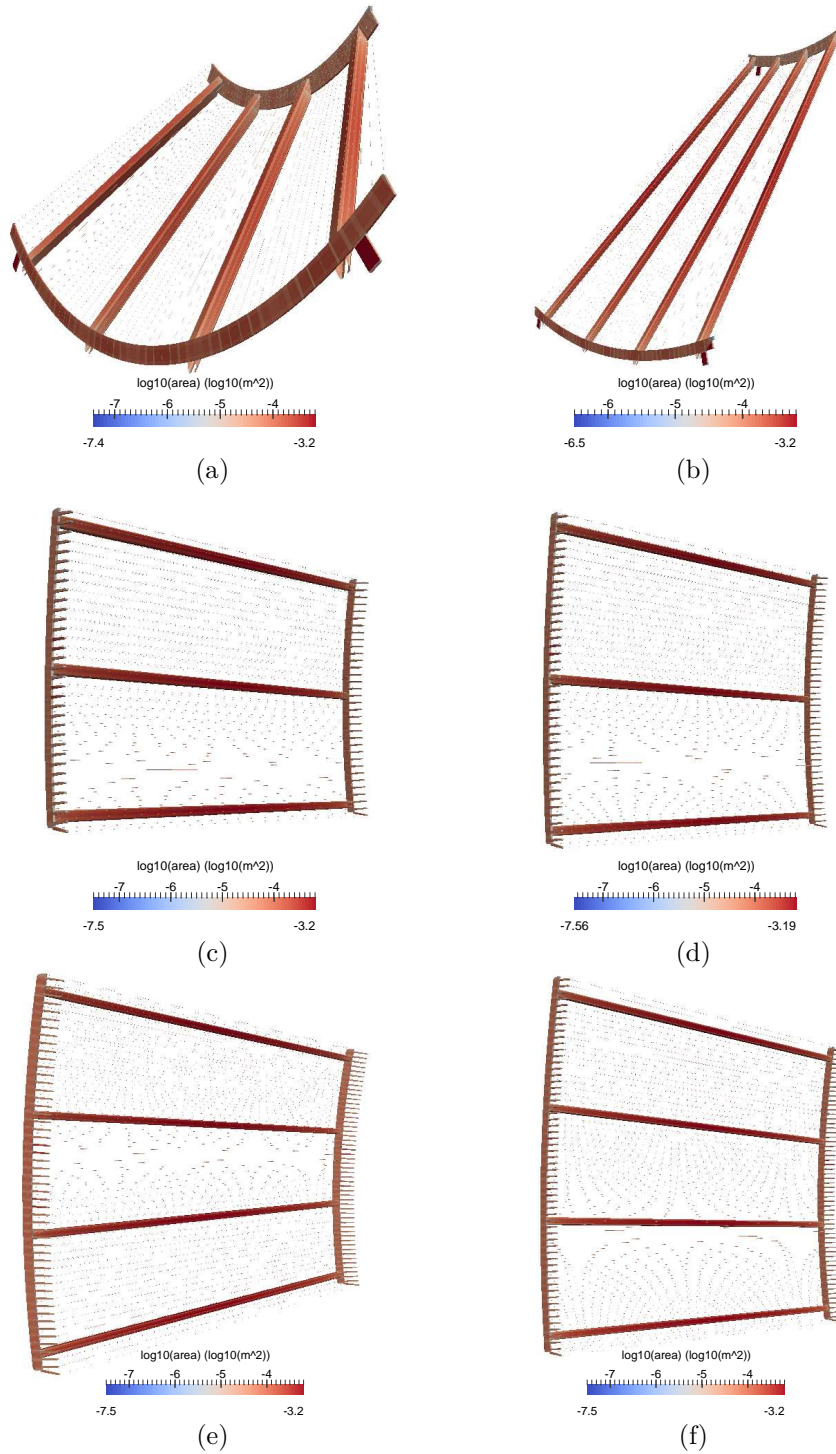


Figure 5.16: KGEOBAG representations of the (a) full metal, (b) steep cone, (c) small flat cone, (d) middle flat cone, (e) large flat cone and (f) cylinder wire modules.

single rings\* (see Fig. 5.15). In addition to reducing the efficiency of background reduction, the presence of short circuits in the wire modules produced unintended changes to the electrostatic potential within the spectrometer as compared to its intended configuration (i.e. without electrical short circuits, hereafter referred to as the *nominal* condition). Using KGEOBAG and KEMFIELD, we were able to produce models to quantify these effects (see Fig. 5.17), which could then be analyzed to determine how the KATRIN collaboration should proceed with the commissioning process. The following discussion of the electrostatic profile of main spectrometer in both the nominal and shorted conditions are direct results from the utilization of the software described in Chapter 4.

### Azimuthal and Radial Effects

As described in Section 5.3.1, the inner and outer wire arrays of each wire module are affixed to wire combs and C-profiles. In the nominal condition, these support structures are held at the outer wire potential. Because of this, their impact on the electrostatic potential within the spectrometer’s flux tube region is largely shielded by the more negative inner wire electrode system, resulting in an azimuthally uniform potential (see Fig. 5.18).

The radial profile of the electrostatic potential at the analyzing plane is determined for large radii by an effective potential composed of a superposition of the potentials of the outer and inner wire arrays (this is reflected in the overall scales of Fig. 5.18 (a) & (b)). For decreasing radii, the ground and anti-Penning electrodes at the entrance and exit of the spectrometer produce an increasingly prominent effect, resulting in a radial inhomogeneity at the analyzing plane of  $\sim 20 V$ .

The introduction of electrical connections between the inner and outer wire layers resulted in a reduction of the shielding of the support structures. As a result, discretely rotationally symmetric perturbations from the C-profiles can be observed near the wire arrays, but decrease in amplitude for smaller radii (see Fig. 5.19). Additionally, because the electrical shorts cause the inner and outer wire arrays to act as a more uniform electrode, there is an increase in the radial homogeneity at the analyzing plane to  $\sim 2 V$  (8).

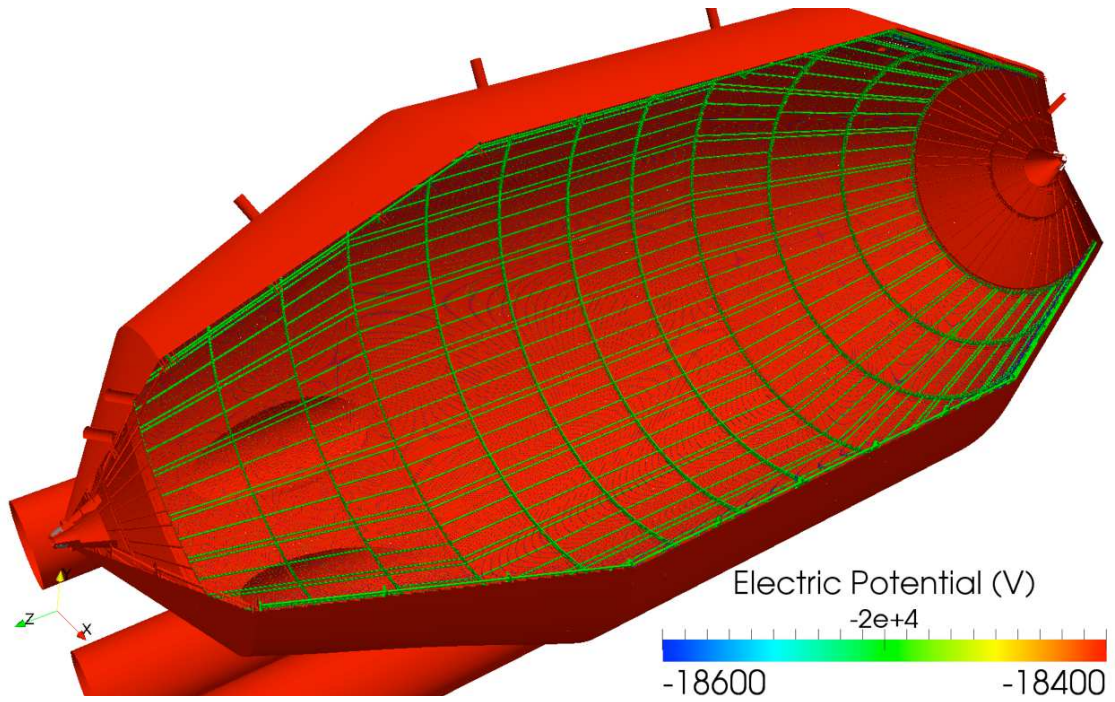
### Axial Effects

Because of the MAC-E-Filter requirement that the electrostatic minimum in the axial direction must be located at the minimum of the magnetic field (known as the *transmission condition*), understanding the profile of the electrostatic potential along a magnetic field line near the analyzing plane is of primary importance to the spectrometer’s efficacy. Prior to bake-out, simulation tools were developed to iteratively

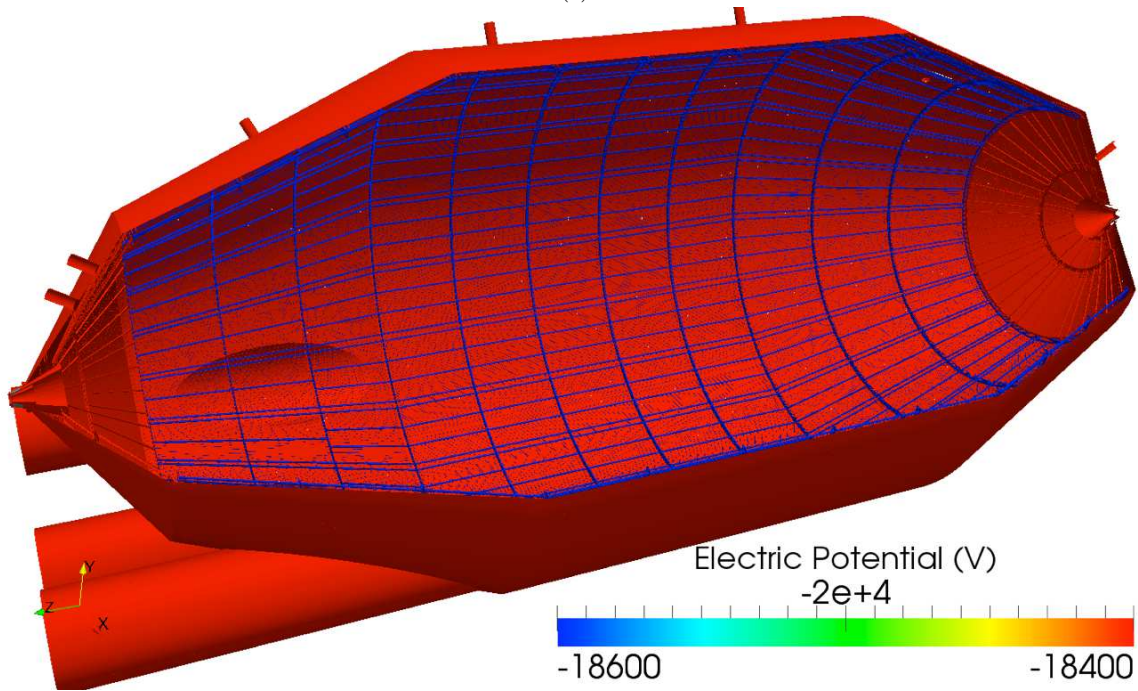
---

\*The short circuits were caused by the deformation of CuBe rods, used to electrically connect wire modules, at high temperatures. Most short circuits have since been repaired.





(a)



(b)

Figure 5.17: Potential profile of the main spectrometer for (a) the nominal condition, and (b) with short circuits. Figure (a) shows a  $\Delta U$  between the inner and outer wire electrodes of 100 V, while in Figure (b)  $\Delta U = 0$  V.

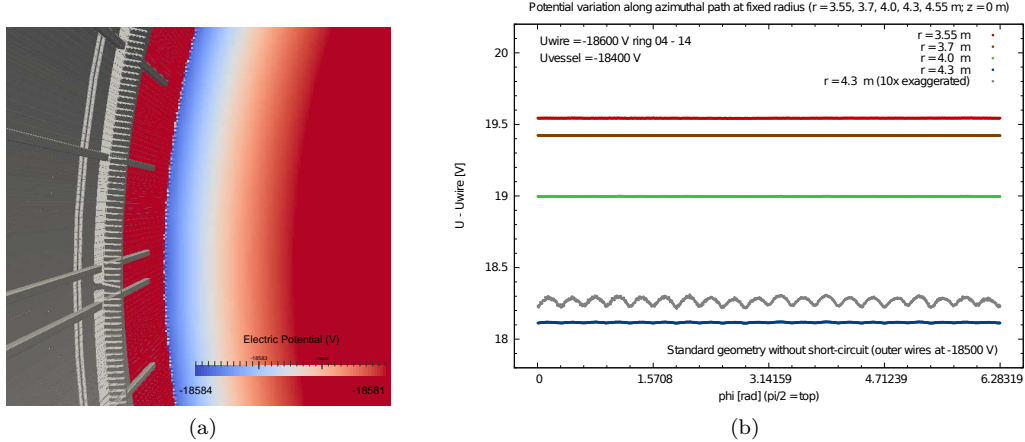


Figure 5.18: (a) Pictorial representation of the electrostatic potential at the analyzing plane near the wire modules for the nominal condition. For scale, the distance between the teeth of the wire module combs is  $25\text{ mm}$ . (b) Azimuthal dependence of the electrostatic potential at the analyzing plane of the main spectrometer at different fixed radii for the nominal condition. The plotted values are the differences between the potential at a field point and the potential of the inner wire electrode system. Image from (8).

converge on an optimized magnet configuration for the nominal electrostatic condition, where the wire combs are held at a more positive potential than the inner wire arrays (see Fig. 5.20 (a)).

As can be seen in Figure 5.20 (b), the presence of short circuits resulted in an increase in the electrostatic potential contribution from the wire combs and wire comb caps at large radii. As a result, the magnet configurations used for assessing the transmission properties of the main spectrometer during commissioning were recomputed with a stronger minimal field at the analyzing plane (from  $3.7\text{ G}$  at the analyzing plane to  $9\text{ G}$ ).

### 5.3.4: Vessel Deformation Studies

Prior to the installation of the wire modules, precise measurements of the radii of the as-built main spectrometer vessel were recorded (9). Results from the cylinder section of the vessel are depicted in Figure 5.21. These measurements showed a  $\mathcal{O}[10^{-2}] m$  deviation of radial uniformity from design specifications. To determine the effects of the vessel deformation on the electrostatic potential within the spectrometer's flux tube region, it was necessary to first convert the discrete set of measured points into a two-dimensional continuous function defined over the vessel's surface.

To construct a continuous deformation profile, we first affect an  $M^{th}$  order trigonometric interpolation over coplanar subsets of our measured data points (points sharing a common  $z$ -value, hereafter referred to

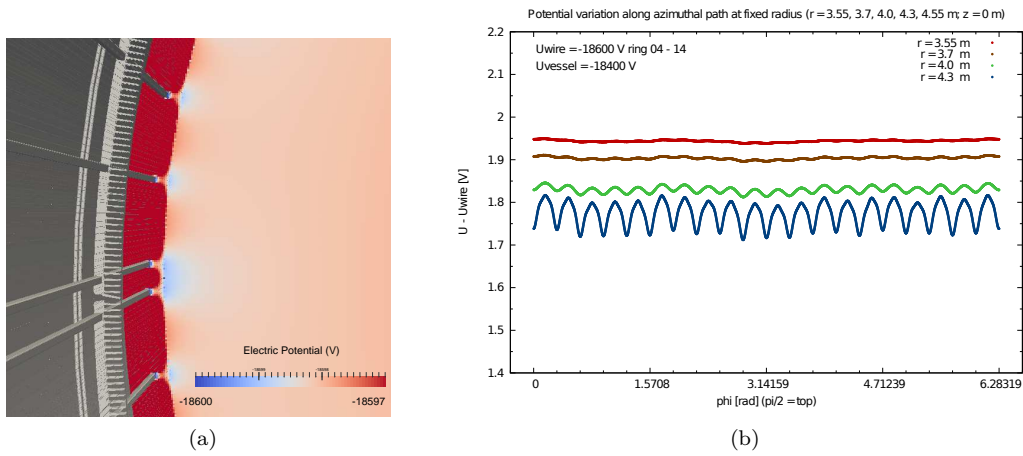


Figure 5.19: (a) Pictorial representation of the electrostatic potential at the analyzing plane near the wire modules for the shorted condition. For scale, the distance between the teeth of the wire module combs is  $25\text{ mm}$ . (b) Azimuthal dependence of the electrostatic potential at the analyzing plane of the main spectrometer at different fixed radii for the shorted condition. The plotted values are the differences between the potential at a field point and the potential of the inner wire electrode system. Image from (8).

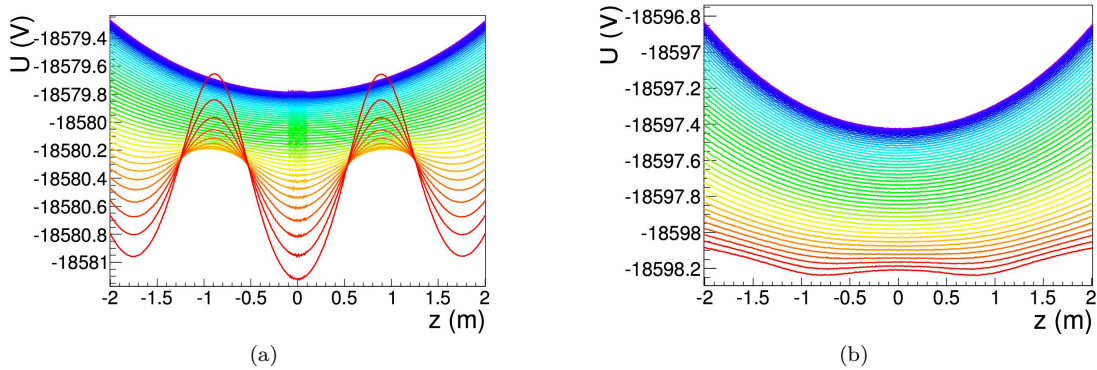
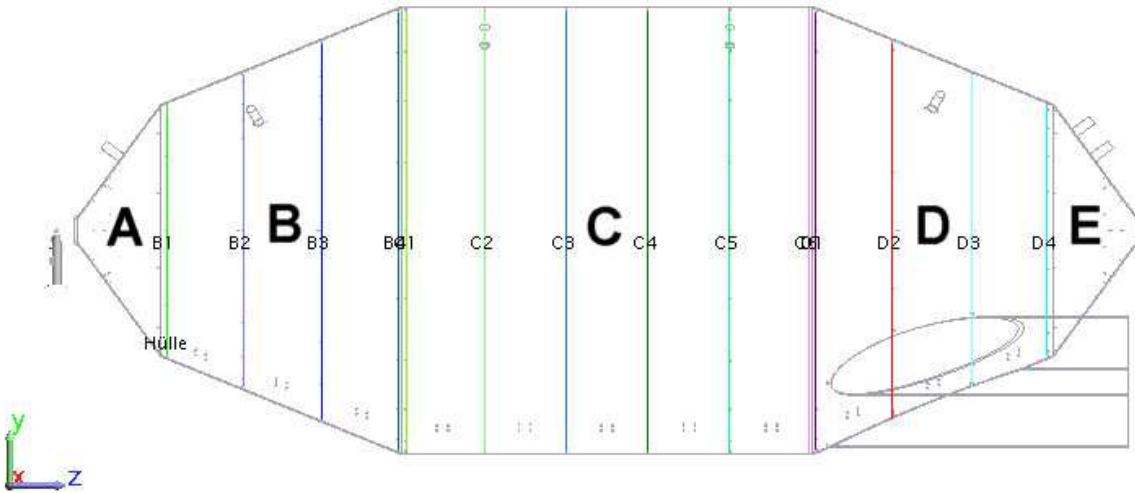
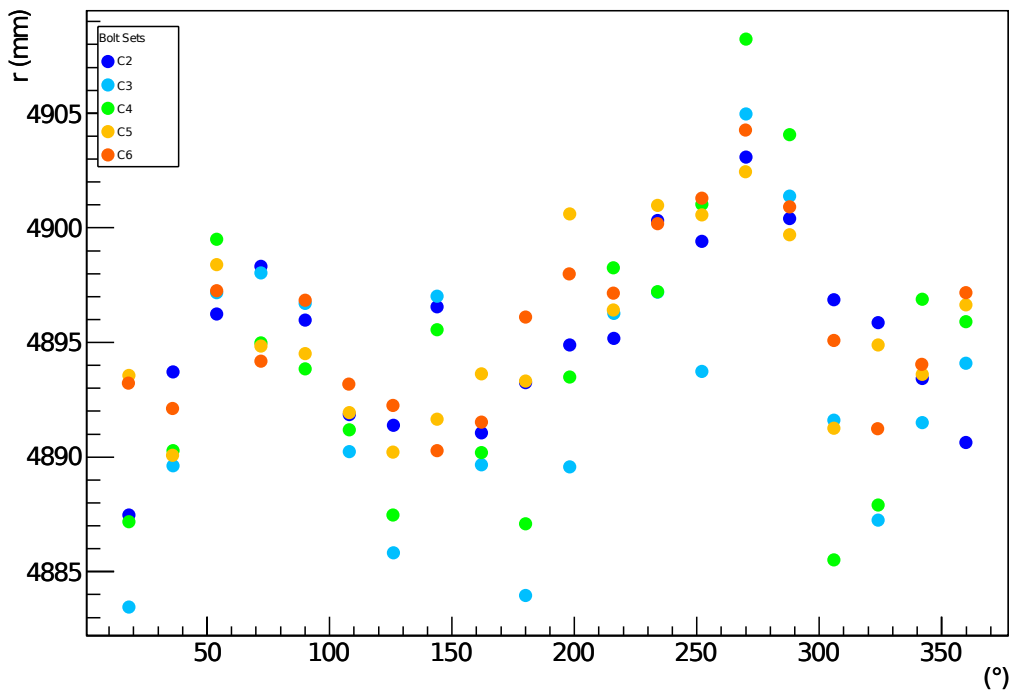


Figure 5.20: Electrostatic potential along magnetic field lines for a magnet configuration optimized for the nominal condition (a) in the intended nominal case, and (b) with short circuits. Magnetic field lines are colored from blue to red by increasing radius within the flux tube region. In (a), the more positive wire combs result in an increase in the electrostatic potential at  $z \approx \pm 0.9$ , even when partially offset by the wire comb caps. In (b), the wire combs and caps produce the opposite effect, creating two separate minima for larger radii that are no longer aligned with the minimum of the magnetic field. Images from (8).



(a)

### Radial values by section



(b)

Figure 5.21: Measured values for the center of the spectrometer vessel prior to wire installation. For reference, the design value for the radius of the middle of the spectrometer is  $4.9\text{ m}$ . Images from (9).

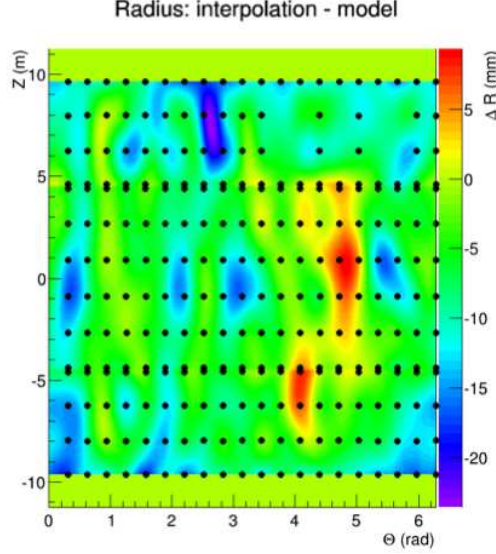


Figure 5.22: Two-dimensional interpolated vessel deformation profile. Measured values are represented by black dots.

as  $\mathcal{S}^i$  for the subset corresponding to the ring of points at  $z_i$ ):

$$R^i(\theta) = \sum_{k=0}^M a_k^i \sin(k\theta) + \sum_{k=0}^M b_k^i \cos(k\theta), \quad (5.1)$$

where  $a_j^i, b_j^i$ ,  $j \in \{0..M\}$  are determined by fitting to the data points in  $\mathcal{S}^i$ . A trigonometric interpolation technique was chosen for these subsets because it naturally yields a result that is  $C^\infty$  continuous and periodic. To compensate for the fact that this technique requires equidistant data points along its domain, we perform a linear interpolation between gaps to complete our data set.

Once we have obtained a discrete set of  $N$  azimuthal interpolation functions spanning a continuous region of the vessel, we can apply a cubic spline interpolation in the axial dimension:

$$R(\theta, z) = A_i(\theta)(z - z_i)^3 + B_i(\theta)(z - z_i)^2 + C_i(\theta)(z - z_i) + D_i(\theta) \quad (5.2)$$

for  $z \in [z_i, z_{i+1}]$ , where  $A_i, B_i, C_i$  and  $D_i$  are determined by fitting  $R^j(\theta)$ ,  $j \in \{1..N\}$ . The use of a cubic spline interpolation provides us with a reasonably continuous ( $C^2$ ) function and a fast ( $\mathcal{O}[N]$ ) algorithm for computing coefficients. This feature is important, since these coefficients must be recomputed at each function call. In the regions where the vessel is only  $C^0$  continuous (i.e. at the intersection of the conical and cylindrical sections), a linear spline interpolation is used to enforce only  $C^0$  continuity. The results of this technique for  $M = 16$  can be seen in Figure 5.22.

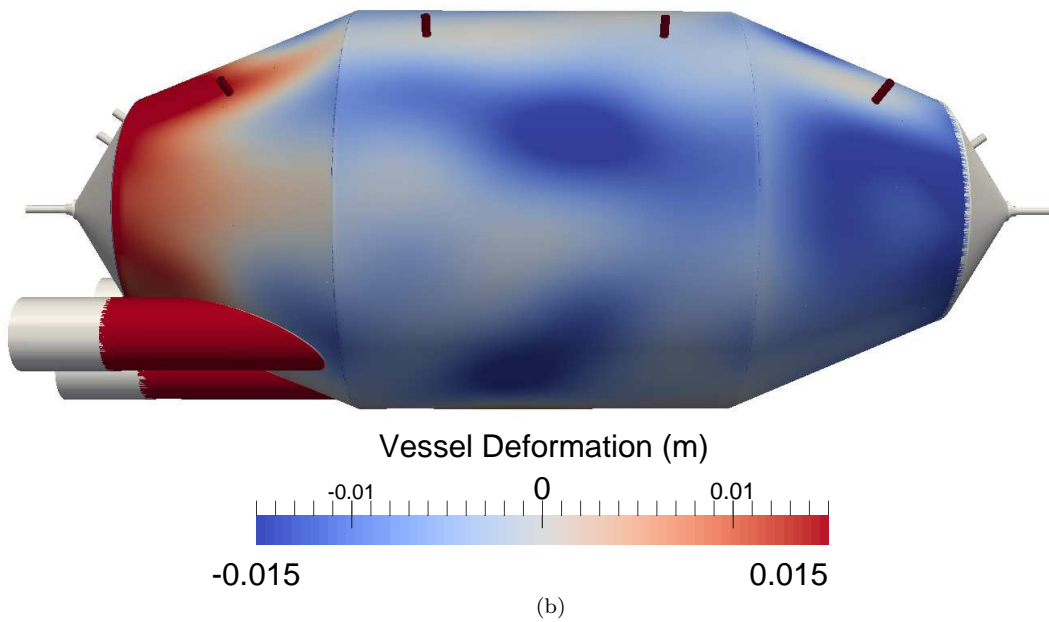
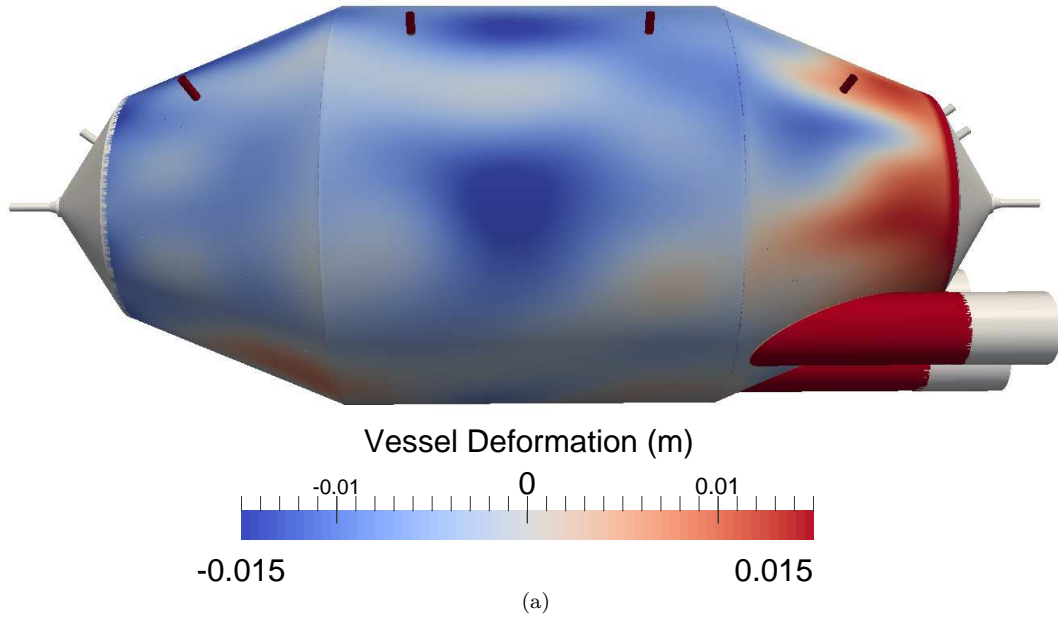


Figure 5.23: (a) East and (b) West sides of the main spectrometer model, with vessel deformation effects included (coloring only applies to the spectrometer vessel, not the ports).

With a continuous interpolation function for the vessel deformation in place, we were then able to modify the discretized elements that comprise the vessel to conform to this profile. Figure 5.23 depicts a graphical result of this application. A simulation containing these vessel deformations for a grounded spectrometer vessel and with the electrode system held at  $1\text{ kV}$  was then performed. As a result, we were able to determine that the perturbation of the electrostatic potential at the analyzing plane of the main spectrometer due to vessel deformation is a  $< 1\%$  effect (see Fig. 5.24).

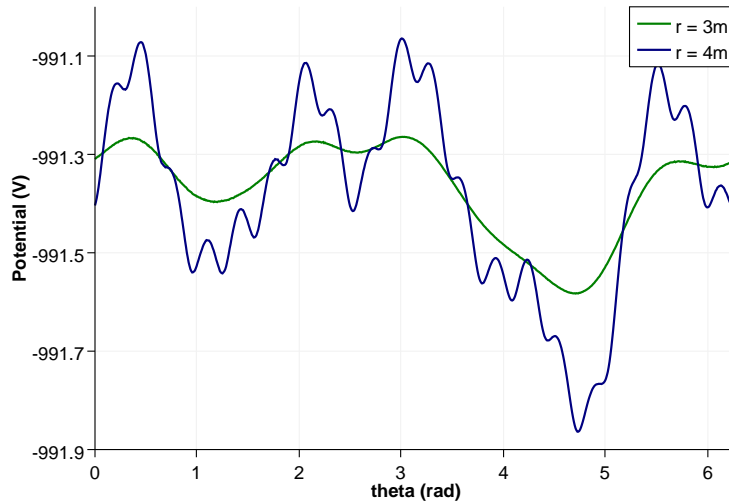


Figure 5.24: Simulated potential values for the main spectrometer at  $z = 0$ ,  $r = 3, 4\text{ m}$  with the deformed vessel held at ground, and the wire system held at  $1\text{ kV}$ . For this plot,  $\theta = 0$  corresponds to the West direction,  $\theta = \frac{\pi}{2}$  corresponds to the positive vertical direction,  $\theta = \pi$  corresponds to the East direction, and  $\theta = \frac{3\pi}{2}$  corresponds to the negative vertical direction. At  $r = 4\text{ m}$  (blue), both the effects from vessel deformation and the C-profiles of the wire modules can be observed. For  $r = 3\text{ m}$  (green), the effects from individual C-profiles has diminished, and the effects from vessel deformation become the dominant perturbative effect.

## Section 5.4: Conclusion

In this chapter, we demonstrated the application of KGEOBAG and KEMFIELD to the electromagnetically active components of KATRIN’s detector region and main spectrometer. By combining our knowledge of the geometric, electrostatic and magnetostatic profiles of these apparatus with the BEM technique and sufficient computational power, we were able to reconstruct these components and their resultant fields in simulation with a heretofore unprecedented degree of accuracy. With these results, we could both explain phenomena witnessed in measurement, and adapt our measurement strategies to improve future results. In summary, we have applied a theoretical understanding of potential theory to information about our system, thereby transforming this information into a form more readily applicable to analysis of KATRIN’s transport system. In the following chapter, we will build upon this information by incorporating a theoretical

framework for electron and ion optics, and using these results to analyze transmission profiles for KATRIN's main spectrometer.



## CHAPTER 6: Transmission Function Measurements in the KATRIN Main Spectrometer with Shifted Analyzing surfaces

### Section 6.1: Introduction

An integral part of commissioning KATRIN's main spectrometer involves validating its electromagnetic configuration via transmission function measurements. To perform these measurements, a well-characterized incident electron beam is passed through a targeted region of the spectrometer, and the filtering effects of the spectrometer in this region are then recorded as a function of the energy of the incident beam. Under standard MAC-E-Filtering conditions, this technique provides information about a two-dimensional plane transverse to the beam line and located at the center of the spectrometer (commonly referred to as the *analyzing plane*). While an electron source with positional selectivity facilitates probing the electromagnetic properties of our spectrometer across the analyzing plane, it does not provide much information about the electromagnetic system both upstream and downstream from this plane.

With different electromagnetic configurations, it is possible to change both the location and the shape of the two-dimensional analyzing plane (to which we hereafter refer more generally as the *analyzing surface*). Subsequent transmission function experiments under these new configurations facilitate the scanning of different regions of the spectrometer, allowing us to measure the electromagnetic fields in these regions. This chapter describes the measurements we performed using nonstandard electromagnetic configurations, and their comparison to our expected results obtained in simulation.

In order to compare our measured transmission values to simulation, we require both a well-characterized incident electron beam and understanding of the electromagnetic components of the spectrometer. As such, Section 6.2 contains a brief description of KATRIN's electron gun and the relevant properties of its generated electron beam for our measurements, and the electromagnetic conditions under which our *shifted analyzing surface* measurements were performed. In Section 6.3, we describe a technique for combining our geometric description of the KATRIN electromagnetic components described in Chapter 5 with the our electron gun characterization to compute simulated transmission function values under the same conditions as our measurements. Finally, in Section 6.4 we compare our simulated results to our measured results.

## Section 6.2: Experimental setup

### 6.2.1: Electron gun

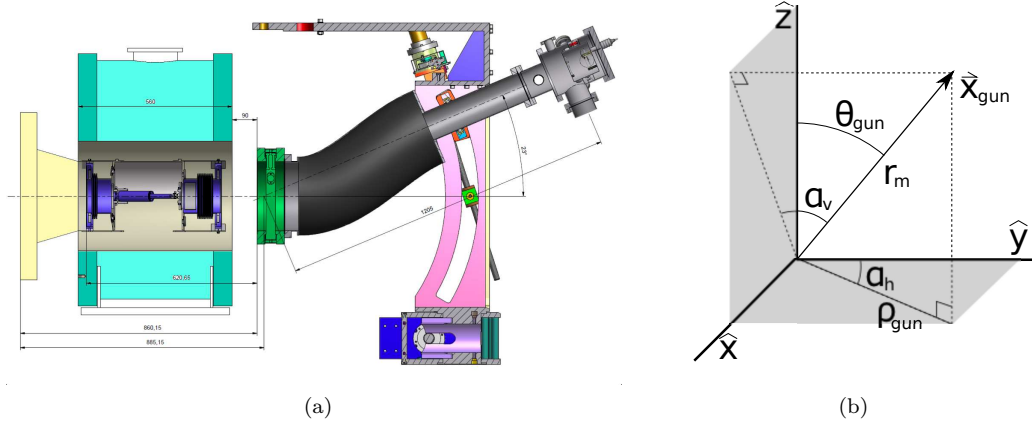


Figure 6.1: (a) CAD representation of the electron gun (with the beam axis from right to left). The cylinder on the right (grey) houses the gun’s cathode and anode, and the curved section (pink) depicts the angular selection mechanism. The gun is mounted to the main spectrometer entrance magnet (aqua). Image from (10). (b) Description of electron gun parameters ( $\alpha_v, \alpha_h$ ) and the parameters used in analysis ( $\rho_{gun}, \theta_{gun}$ ), with origin at  $\mathbf{x}_m$ .

For the commissioning of the main spectrometer, an electron gun was developed to provide a characterized mono-energetic electron beam with a tunable position, *pitch angle*\* and energy profile (see Fig. 6.1 (a)). The electron gun generates the emission of electrons via the photoelectric effect using a silver target exposed to an ultraviolet LED light source. These electrons are then accelerated to a user-defined kinetic energy through an axially symmetric anode before entering the flux tube region.

The position of the electron gun is defined with respect to intrinsic parameters of the electron gun as

$$\mathbf{x}_{gun} = (-r_m \cos(\alpha_v) \sin(\alpha_h) + x_m, r_m \sin(\alpha_v) + y_m, -r_m \cos(\alpha_v) \cos(\alpha_h) + z_m), \quad (6.1)$$

where  $r_m$  is the length of the electron gun’s manipulator arm,  $\alpha_h$  and  $\alpha_v$  are the horizontal and vertical angles of the manipulator arm, and  $\mathbf{x}_m = (x_m, y_m, z_m)$  is the positional offset of the apparatus with respect to global coordinates, where the center of the main spectrometer is the origin (see Fig. 6.1 (b)). These parameters have been determined in (10) and refined in (56), and are described in Table 6.1. To achieve angular selectivity, the gun’s cathode is designed to pivot about one of its primary axes. While this design is efficacious when the spectrometer and electron gun assembly is held at higher voltages ( $\sim 18.6$  kV),

---

\*The pitch angle of a particle is the angle between the momentum vector and the magnetic field; see Sec. 6.3.1.

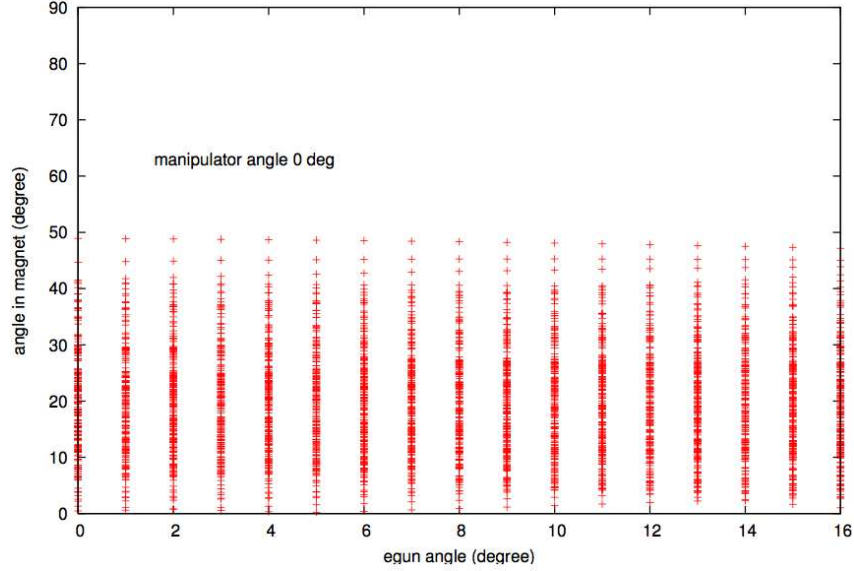


Figure 6.2: Simulation comparing the electron gun’s user-selected angle to the resultant pitch angle of ejected particles at the spectrometer’s entrance, for  $\Phi_{anode} - \Phi_{cathode} = 50 \text{ V}$ . Calculated for electron starting energies which are Gaussian distributed around 0.2 eV with a sigma of 0.2 eV. Image courtesy of M. Zacher (personal communication, June 26, 2014).

parameter	symbol	value
manipulator arm length	$r_m$	1.206 m
$x$ -coordinate of electron gun offset	$x_m$	-0.0157 m
$y$ -coordinate of electron gun offset	$y_m$	-0.0012 m
$z$ -coordinate of electron gun offset	$z_m$	-12.416 m

Table 6.1: Electron gun parameters.

no correlation between the electron gun angle  $\theta_{gun}$  and the resulting incident pitch angle  $\theta_0$  is observed in electron optics simulations in a low-energy configuration (with the anode at  $\sim 1 \text{ kV}$ , see Fig. 6.2). The energy distribution of the resultant electron beam for the low-energy configuration has been measured empirically to be normally distributed about a user-defined input energy  $e \cdot T_e$  (10). Using a UV LED with a peak wavelength of 295 nm, a standard deviation of 0.076 eV was observed.

### 6.2.2: Electrostatic configuration

For standard operating conditions, the main spectrometer’s electromagnetic configuration is chosen to form an electrostatic potential that is nearly axially symmetric, and containing an electrostatic minimum along the beam axis at the center of the spectrometer (the analyzing plane). To match this electrostatic profile, the magnetostatic fields are configured to be axially symmetric and to achieve maximum strength at the entrance and exit of the spectrometer, and minimum strength at the analyzing plane.

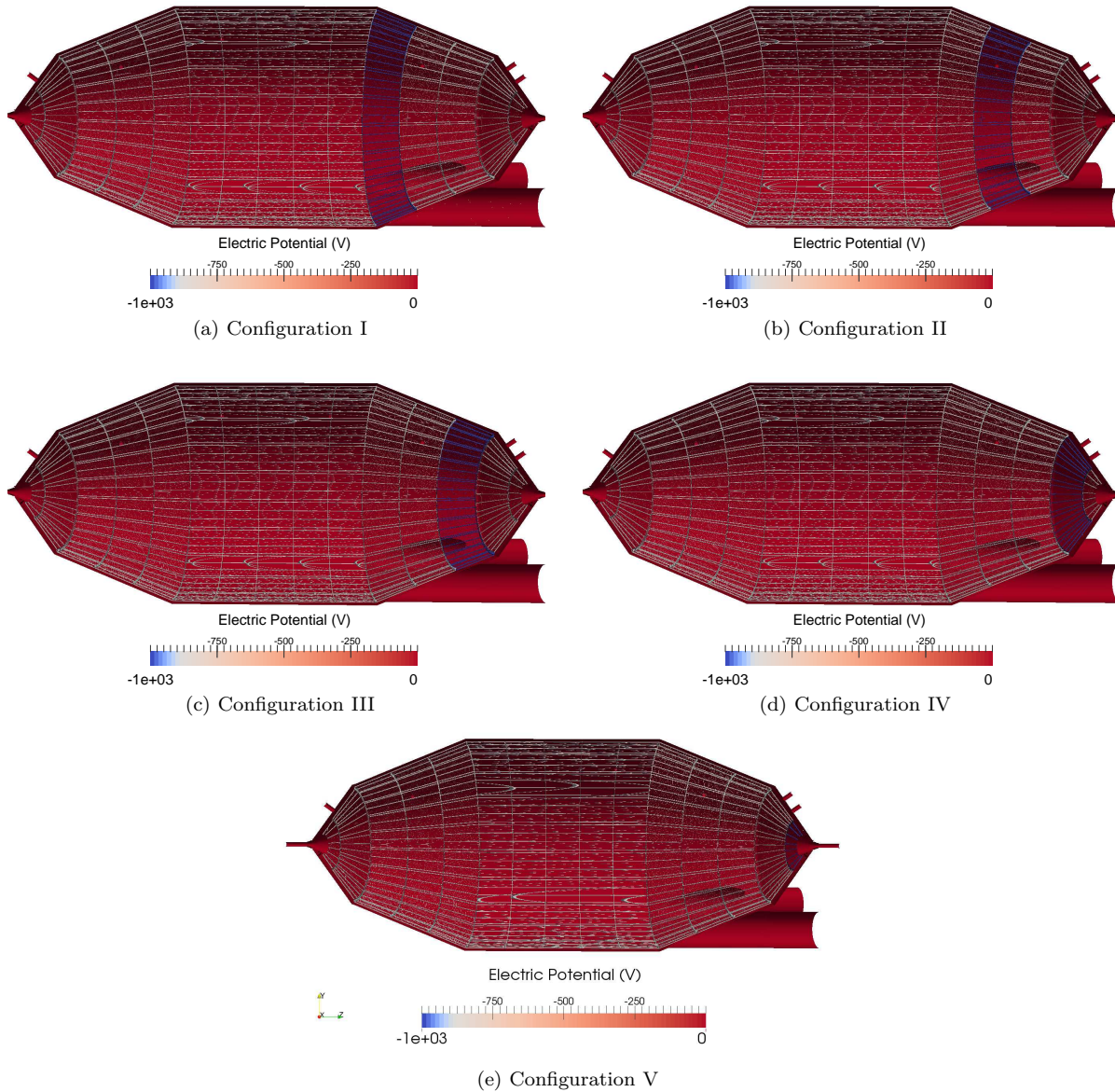


Figure 6.3: Electrostatic configurations for shifted analyzing plane measurements. Configurations I through V have a single downstream wire module ring (rings 12 through 16, respectively) held at  $-1\text{ kV}$ , with the remaining rings held at  $-900\text{ V}$ . For all measurements, the spectrometer vessel was held at ground.

For each of the shifted analyzing surface measurements, a single downstream electrode ring was held at a more negative potential than the remaining electrodes (see Fig. 6.3), with the intent of producing a potential minimum that is both translated away from the center of the spectrometer and deformed into a nonplanar surface. The magnetostatic configuration used for these measurements was unchanged from the standard condition, resulting in a misalignment of the electrostatic and magnetostatic minima. While this implies a sub-optimal overall transmission condition, the goal of these measurements to sample different regions of the spectrometer is largely insensitive to this misalignment, and the effects of misalignment on the overall transmission function can be accounted for in simulation (see Sec. 6.3).

### 6.2.3: Run settings

Table 6.2 describes the electron gun and spectrometer settings for the runs comprising the shifted analyzing plane measurements. For each of the five spectrometer settings, transmission function runs were performed with the electron gun having an azimuthal angle corresponding to a particle trajectory near the middle of a wire module (Run Sets 1 through 4), and subsequently corresponding to a trajectory in between two wire modules (Run Sets 5 through 8). For each of these two settings, four measurements were performed with the gun set to different radial offsets.

## Section 6.3: Simulation of transmission functions

A general expression for the expected transmission fraction given a configuration of the electron gun  $\mathbf{c}_e$  and spectrometer  $\mathbf{c}_s$  is given as

$$P(\mathbf{c}_e, \mathbf{c}_s) = \int_{\mathcal{I}} P_{occ}(\mathbf{c}_e, \chi) \times P_{trans}(\mathbf{c}_s, \chi) d\chi, \quad (6.2)$$

where  $\mathcal{I}$  defines the available phase space of initial particle states,  $P_{occ}(\mathbf{c}_e, \chi)$  is a probability density function describing the likelihood of the occurrence of state  $\chi$  given the electron gun parameters  $\mathbf{c}_e$ , and  $P_{trans}(\mathbf{c}_s, \chi)$  describes the probability that a particle with initial state  $\chi$  is successfully transmitted through the spectrometer with configuration  $\mathbf{c}_s$ . Our goal is then to determine functional forms for  $P_{trans}(\mathbf{c}_s, \chi)$  and  $P_{occ}(\mathbf{c}_e, \chi)$ , so that a numerical evaluation of Equation 6.2 can be computed and compared against empirical results. We will hereafter refer to these probability density functions as the *transmission probability* and *occurrence probability*, respectively.

Run #	$\alpha_v(deg)$	$\alpha_h(deg)$	Config.	Run #	$\alpha_v(deg)$	$\alpha_h(deg)$	Config.
Run Set 1				Run Set 5			
6101	14.00	13.60	I	6158	16.40	11.60	I
6103	14.00	13.60	II	6160	16.40	11.60	II
6005	14.00	13.60	III	6162	16.40	11.60	III
6107	14.00	13.60	IV	6164	16.40	11.60	IV
6109	14.00	13.60	V	6166	16.40	11.60	V
Run Set 2				Run Set 6			
6111	13.54	13.15	I	6172	14.40	10.22	I
6113	13.54	13.15	II	6174	14.40	10.22	II
6115	13.54	13.15	III	6176	14.40	10.22	III
6117	13.54	13.15	IV	6178	14.40	10.22	IV
6119	13.54	13.15	V	6180	14.40	10.22	V
Run Set 3				Run Set 3			
6125	12.95	12.60	I	6192	17.20	5.50	I
6127	12.95	12.60	II	6194	17.20	5.50	II
6129	12.95	12.60	III	6196	17.20	5.50	III
6131	12.95	12.60	IV	6198	17.20	5.50	IV
6133	12.95	12.60	V	6200	17.20	5.50	V
Run Set 4				Run Set 8			
5135	12.08	11.80	I	6214	15.20	4.85	I
6137	12.08	11.80	II	6216	15.20	4.85	II
6140	12.08	11.80	III	6218	15.20	4.85	III
6142	12.08	11.80	IV	6220	15.20	4.85	IV
6144	12.08	11.80	V	6222	15.20	4.85	V

Table 6.2: Run configurations for the shifted analyzing plane measurement.

### 6.3.1: Determination of the transmission probability

#### Definition of parameters

To acquire a description of the transmission probability as a function of initial particle states, we begin by analytically describing the parametrized trajectory of a single transmitted non-relativistic electron through an idealized MAC-E-Filter (i.e. a large evacuated vessel with adiabatically changing electrostatic and magnetostatic fields). Since our particle's trajectory is a one-dimensional path, it is possible to parametrize the state of the particle along this path by a unitless parameter  $s \in [0, 1]$  that spans the trajectory. We define the state variables of our particle's trajectory  $\mathbf{x}(s)$  and  $\mathbf{p}(s)$  as the parametrized position and momentum of the electron, respectively. Additionally, we define  $\mathbf{B}(s) = \mathbf{B}(\mathbf{x}(s))$  and  $\Phi(s) = \Phi(\mathbf{x}(s))$  to be the parametrized magnetic field and electrostatic potential along the electron's trajectory.

#### Decomposition of state variables into transverse and longitudinal components

We define  $\theta(s) = \cos^{-1}(\hat{\mathbf{p}}(s) \cdot \hat{\mathbf{B}}(s))$  as the angle between the particle's momentum and the magnetic field (referred to as the *pitch angle*), allowing us to recast our momentum vector into the local coordinates

of the magnetic field:  $\mathbf{p}(s) = \mathbf{p}_{\parallel}(s) + \mathbf{p}_{\perp}(s)$ , where

$$\mathbf{p}_{\parallel}(s) = (\mathbf{p} \cdot \hat{\mathbf{B}}) \hat{\mathbf{B}} = |\mathbf{p}| \cos \theta \hat{\mathbf{B}} \quad (6.3)$$

and

$$\mathbf{p}_{\perp}(s) = \mathbf{p} \times \hat{\mathbf{B}} = |\mathbf{p}| \sin \theta (\hat{\mathbf{p}} \times \hat{\mathbf{B}}). \quad (6.4)$$

We define the kinetic energy of our particle

$$T(s) = \frac{|\mathbf{p}|^2}{2m}, \quad (6.5)$$

and decompose it into longitudinal and transverse contributions as well:

$$T_{\parallel}(s) = \frac{\mathbf{p}_{\parallel}^2}{2m} = \frac{|\mathbf{p}|^2 \cos^2 \theta}{2m} \quad (6.6)$$

and

$$T_{\perp}(s) = \frac{\mathbf{p}_{\perp}^2}{2m} = \frac{|\mathbf{p}|^2 \sin^2 \theta}{2m}, \quad (6.7)$$

where  $T = T_{\parallel} + T_{\perp}$ .

In a similar fashion, we decompose our particle's trajectory  $\mathbf{x}(s)$  into a component along the magnetic field line (hereafter referred to as the *guiding center* component, or  $\mathbf{x}_{gc}(s)$ ) and a cyclotron precession about the guiding center (denoted  $\mathbf{x}_{cyc}(s)$ ), so that

$$\mathbf{x}(s) = \mathbf{x}_{gc}(s) + \mathbf{x}_{cyc}(s). \quad (6.8)$$

The zeroth-order magnitude of the cyclotron motion of our particle  $|\mathbf{x}_{cyc}(s)|$  is its cyclotron radius  $r_g(s)$ :

$$r_g(s) = \frac{|\mathbf{p}_{\perp}(s)|}{|e||\mathbf{B}(s)|} \quad (6.9)$$

with angular frequency

$$\omega_g(s) = \frac{|e||\mathbf{B}(s)|}{m}, \quad (6.10)$$

where  $e$  is the signed electron charge and  $m$  is the electron mass in SI units. We can define an additional azimuthal angle  $\phi(s)$  as a measure the cyclotron precession in the plane transverse to the magnetic field  $\mathbf{B}(s)$ ; however, it suffices for now to merely acknowledge that a unique  $\phi(s_1)$  corresponds to a single  $\phi(s_2)$  for all  $s_1, s_2 \in [0, 1]$ . The trajectory of our guiding center component can be computed by numerically solving

the ordinary differential equation

$$\frac{d}{ds} \mathbf{x}_{gc}(s) = \hat{\mathbf{B}}(\mathbf{x}_{gc}(s)) \quad (6.11)$$

using standard Runge-Kutta techniques (57), subject to the initial condition

$$\mathbf{x}_{gc}(0) = \mathbf{x}(0) + \left( \hat{\mathbf{p}}(0) \times \hat{\mathbf{B}}(0) \right) r_g(0). \quad (6.12)$$

### Adiabatic invariance and energy conservation

MAC-E-Filters are designed to exploit the conservation of the angular momentum of a particle's cyclotron motion (22). In the non-relativistic limit, this corresponds to an adiabatically invariant magnetic moment of the electron's cyclotron orbit:

$$|\mu| = \frac{T_{\perp}(s)}{|\mathbf{B}(s)|}. \quad (6.13)$$

This equality holds throughout the electron's trajectory through the filter:

$$\forall s_1, s_2 \in [0, 1] : \frac{T_{\perp}(s_1)}{|\mathbf{B}(s_1)|} = \frac{T_{\perp}(s_2)}{|\mathbf{B}(s_2)|}. \quad (6.14)$$

Incorporating the effects of an electrostatic potential in the MAC-E-Filter yields the energy relation

$$\forall s_1, s_2 \in [0, 1] : T(s_1) + e \cdot \Phi(s_1) = T(s_2) + e \cdot \Phi(s_2). \quad (6.15)$$

By combining Equations 6.14 and 6.15 into

$$\forall s_1, s_2 \in [0, 1] : T_{\parallel}(s_2) = T(s_1) \left( 1 - \frac{|\mathbf{B}(s_2)|}{|\mathbf{B}(s_1)|} \cdot \sin^2 \theta(s_1) \right) - e \cdot (\Phi(s_2) - \Phi(s_1)), \quad (6.16)$$

and by enforcing the condition that the particle be transmitted (i.e. we require that  $T_{\parallel}(s) > 0 \forall s$ ), we arrive at an inequality to describe the transmission condition

$$\forall s_1, s_2 \in [0, 1] : T(s_1) > H(s_1, s_2), \quad (6.17)$$

where

$$H(s_1, s_2) = \frac{e \cdot (\Phi(s_2) - \Phi(s_1))}{\left( 1 - \frac{|\mathbf{B}(s_2)|}{|\mathbf{B}(s_1)|} \cdot \sin^2 \theta(s_1) \right)}. \quad (6.18)$$

While Equation 6.17 holds for any two points on the particle's trajectory, the condition is most restrictive when  $s_1$  is chosen to identify the incident particle's initial state (i.e.  $s_1 = 0$ ), and when  $s_2$  is selected to



maximize Equation 6.18:

$$H(0, s^*) = \max_s [H(0, s)]. \quad (6.19)$$

Given a distribution of initial particle states, the locus of corresponding positions  $\mathbf{x}(s^*)$  define a surface within the spectrometer called the *analyzing surface*. Using the above definitions in tandem with the equations from Section 6.3.1, we can construct a method for adiabatically propagating a distribution of initial particle states to the analyzing surface, and evaluating the resulting transmission condition.

### Computing the intersection of the guiding center with the analyzing surface

Our first step in adiabatically propagating an initial particle state to the analyzing surface is to compute the intersection of a particle's guiding center with the analyzing surface. We do this as follows:

- Given an initial condition  $\mathbf{x}_0, \mathbf{p}_0$ , we compute the magnetic field  $\mathbf{B}_0 = \mathbf{B}(\mathbf{x}_0)$  and electrostatic potential  $\Phi_0 = \Phi(\mathbf{x}_0)$ .
- Our initial pitch angle can now be evaluated as  $\theta_0 = \cos^{-1}(\hat{\mathbf{p}}_0 \times \hat{\mathbf{B}}_0)$ .
- We then use these values to compute  $\mathbf{x}_{gc}(0) = \mathbf{x}_0 + (\hat{\mathbf{p}}_0 \times \hat{\mathbf{B}}_0) \cdot r_g(0)$ , where  $r_g(0) = \frac{|\mathbf{p}_0| \sin \theta_0}{|e| |\mathbf{B}_0|}$ .
- Using the initial condition  $\mathbf{x}_{gc}(0)$ , we obtain an expression for  $\mathbf{x}_{gc}(s)$  by numerically solving Equation 6.11.
- We perform a maximization over  $H_{gc}(0, s)$  to find  $\mathbf{x}_{gc}^* = \mathbf{x}_{gc}(s^*)$ , where

$$\mathbf{H}_{gc}(0, s^*) = \max_s \frac{e \cdot (\Phi(\mathbf{x}_{gc}(s)) - \Phi_0)}{\left(1 - \frac{|\mathbf{B}(\mathbf{x}_{gc}(s))|}{|\mathbf{B}_0|} \cdot \sin^2 \theta_0\right)}. \quad (6.20)$$

### Generalization to a distribution of initial conditions

Since we have not resolved the azimuthal angle  $\phi(s)$  of the particle's cyclotron progression, we only know that our particle lies somewhere on a circle transverse to our guiding center, whose radius is given by the cyclotron radius at the analyzing surface. By combining Equations 6.7, 6.9 and 6.14, we can solve for this cyclotron radius in terms of initial conditions to be

$$r_g(s) = \frac{|\mathbf{p}_0| \sin \theta_0}{|e| \sqrt{|\mathbf{B}_0| |\mathbf{B}(\mathbf{x}_{gc}(s))|}}. \quad (6.21)$$

It turns out that, for a continuous statistical distribution of initial momenta  $\mathbf{p}_0$ , this scope of resolution is sufficient for calculating the rate of transmitted particles for a given configuration. This result is due to the strong dependence of the integrated angular frequency on the initial energy. We can confirm this in

simulation by numerically computing the approximate number of cyclotron orbits completed by a trajectory from its initial position to the analyzing surface:

$$\begin{aligned}
\frac{\phi(s^*)}{2\pi} &= \frac{1}{2\pi} \int_0^{s^*} ds \cdot \omega_g(s) \frac{dt}{ds} \approx \\
&\approx \frac{|e|}{2\pi} \int_0^{s^*} ds \cdot \frac{|\mathbf{B}(\mathbf{x}_{gc}(s))|}{|\mathbf{p}_{\parallel}(s)|} = \\
&= \frac{|e|}{2\pi\sqrt{2m}} \int_0^{s^*} \frac{|\mathbf{B}(\mathbf{x}_{gc}(s))| ds}{\sqrt{T_0 \left(1 - \frac{|\mathbf{B}(\mathbf{x}_{gc}(s))|}{|\mathbf{B}_0|} \cdot \sin^2 \theta_0\right) - e \cdot (\Phi(\mathbf{x}_{gc}(s)) - \Phi_0)}}. \tag{6.22}
\end{aligned}$$

Using Equation 6.22 with specified initial conditions just above the transmission threshold and varying the initial kinetic energy by  $\Delta T$ ,  $\frac{\Delta T}{T_0} \sim \mathcal{O}[10^{-5}]$ , we have numerically obtained an order-of-magnitude estimate for the sensitivity of the azimuthal angle of our particle at the analyzing surface with respect to fluctuations in the initial kinetic energy:

$$\frac{\phi(s^*; \mathbf{x}_0, T_0 + \Delta T, \theta_0) - \phi(s^*; \mathbf{x}_0, T_0, \theta_0)}{2\pi} \sim \mathcal{O}[10^2]. \tag{6.23}$$

Since  $\mathcal{O}[10^2] \gg 1$ , we can well approximate the distribution of final particle states at the analyzing surface as azimuthally uniformly distributed about the intersection of the guiding center and the analyzing surface.

### Determining the Surface of Intersection on the Analyzing Surface

We now have a point on our analyzing surface  $\mathbf{x}_{gc}^*$ , and a unit vector orthogonal to the analyzing surface  $\hat{\mathbf{B}}(\mathbf{x}_{gc}^*)$  (hereafter referred to as  $\hat{\mathbf{B}}^*$ ). We can construct a pair of mutually orthogonal vectors  $\hat{\mathbf{C}}^*$  and  $\hat{\mathbf{D}}^*$ ,  $\hat{\mathbf{B}}^* \cdot \hat{\mathbf{C}}^* = \hat{\mathbf{B}}^* \cdot \hat{\mathbf{D}}^* = \hat{\mathbf{C}}^* \cdot \hat{\mathbf{D}}^* = 0$ :

$$\begin{aligned}
\hat{\mathbf{B}}^* &= B_x \hat{x} + B_y \hat{y} + B_z \hat{z}, \\
\hat{\mathbf{C}}^* &= \frac{1}{\sqrt{1 - B_y^2}} (-B_z \hat{x} + B_x \hat{z}), \\
\hat{\mathbf{D}}^* &= \frac{1}{\sqrt{1 - B_y^2}} (B_x B_y \hat{x} - (1 - B_y^2) \hat{y} + B_y B_z \hat{z}), \tag{6.24}
\end{aligned}$$

and express our particle's location at the analyzing surface in terms of Equations 6.8 and 6.24 and a unique azimuthal phase  $\phi'$ :

$$\mathbf{y}(s^*, \phi') = \mathbf{x}_{gc}(s^*) + r_g(s^*) \left( \hat{\mathbf{C}}^* \cos \phi' + \hat{\mathbf{D}}^* \sin \phi' \right), \tag{6.25}$$

where

$$r_g(s^*) = \frac{\sqrt{2mT_0} \sin \theta_0}{|e| \sqrt{|\mathbf{B}_0| |\mathbf{B}(\mathbf{x}_{gc}(s^*))|}}. \quad (6.26)$$

In the event that our analyzing surface has nonzero curvature, the result of Equation 6.25 must be projected back onto the analyzing surface. To perform this projection, we modify Equation 6.18 to account for the offset of the gyroradius:

$$G(s_1, s_2) = \frac{e \cdot (\Phi(\mathbf{y}(s_2)) - \Phi(\mathbf{y}(s_1)))}{\left(1 - \frac{|\mathbf{B}(\mathbf{y}(s_2))|}{|\mathbf{B}(\mathbf{y}(s_1))|} \cdot \sin^2 \theta(s_1)\right)} \quad (6.27)$$

and perform our maximization over this function:

$$G(0, s^*) = \max_s [G(0, s)]. \quad (6.28)$$

We now have a numerically soluble description for our transmission probability in terms of the spectrometer properties  $\mathbf{c}_s$ , and initial particle conditions  $\mathbf{x}_0$  and  $T_0$  and  $\theta_0$ , as well as our final azimuthal angle at the analyzing plane  $\phi$ :

$$P_{trans}(\mathbf{x}_0, T_0, \theta_0, \phi; \mathbf{c}_s) = \begin{cases} 1 & T_0 \geq G(\mathbf{x}_0, T_0, \theta_0, \phi; \mathbf{c}_s) \\ 0 & T_0 < G(\mathbf{x}_0, T_0, \theta_0, \phi; \mathbf{c}_s) \end{cases}, \quad (6.29)$$

where

$$G(\mathbf{x}_0, T_0, \theta_0, \phi; \mathbf{c}_s) = \frac{e \cdot (\Phi(\mathbf{y}^*) - \Phi(\mathbf{x}_0))}{\left(1 - \frac{|\mathbf{B}(\mathbf{y}^*)|}{|\mathbf{B}(\mathbf{x}_0)|} \cdot \sin^2 \theta_0\right)} \quad (6.30)$$

and the magnetic field and electrostatic potential are implicitly dependent upon the spectrometer configuration  $\mathbf{c}_s$ . Since the distribution of azimuthal angles at the analyzing plane is uniform, we can integrate Equation 6.29 over the final azimuthal angles to obtain our desired expression for the transmission probability as a function of spectrometer properties and initial particle conditions:

$$P_{trans}(\mathbf{x}_0, T_0, \theta_0; \mathbf{c}_s) = \int_0^{2\pi} d\phi \cdot P_{trans}(\mathbf{x}_0, T_0, \theta_0, \phi; \mathbf{c}_s). \quad (6.31)$$

### 6.3.2: Determination of the occurrence probability

The occurrence probability is intrinsically derived from a statistical description of the electron gun. As such, a natural basis of state variables for this probability density function is linked to the free parameters of the electron gun: the position  $\mathbf{x}$ , the energy  $T$ , pitch angle  $\theta$  and azimuthal angle  $\phi$  of the ejected

particle. Due to the strong electrostatic fields responsible for particle acceleration within the electron gun, the trajectories of the ejected particles are ill-suited to an adiabatic approximation in this region. As a result, we rely on Monte-Carlo simulation and empirically measured parameters to obtain a statistical description of initial particle states at the entrance to the spectrometer, where the assumption of adiabatic particle transport is valid.

For a given angular setting  $\alpha_v, \alpha_h$ , the location of the electron gun's ejected particles is given by Equation 6.1 as  $\mathbf{x}_{gun}$ . Particles originating from this position will precess about the magnetic field line crossing through  $\mathbf{x}_{gun}$ , allowing us to apply the same technique we employed in Section 6.3.1: we approximate the initial position of the particle by propagating a guiding center from  $\mathbf{x}_{gun}$  to the entrance of the spectrometer and apply an offset for the gyroradius. If we treat the initial particle position as exact<sup>†</sup>, our goal is then to represent the initial momentum states as a statistical distribution

$$P_{occ}(T_0, \theta_0, \phi_0) \tag{6.32}$$

describing the likelihood of obtaining an initial particle with a given state configuration.

Assuming that the energy, pitch angle and azimuthal angle are uncorrelated, Equation 6.32 can be decomposed into the product of three probability density functions:

$$P_{occ}(T_0, \theta_0, \phi_0) = P(T_0) \times P(\theta_0) \times P(\phi_0). \tag{6.33}$$

We can immediately substitute  $P(\phi_0) = \frac{1}{2\pi}$ , since the ejected particles are uniformly distributed in the azimuthal direction. At low energies, our pitch angle at the spectrometer's entrance  $\theta_0$  has been measured in simulation to have mean value and standard deviation

$$\mu_\theta = 0.12 \text{ rad}, \tag{6.34}$$

$$\sigma_\theta = 0.10 \text{ rad}, \tag{6.35}$$

respectively. If we assume a truncated normal distribution for  $\theta$  confined to  $[0, \pi]$ , our dependence on  $\theta$  becomes

$$P(\theta_0; \mu_\theta, \sigma_\theta) = \frac{1}{Z(\mu_\theta, \sigma_\theta)} \cdot \frac{1}{\sigma_\theta \sqrt{2\pi}} e^{-\frac{(\theta_0 - \mu_\theta)^2}{2\sigma_\theta^2}}, \tag{6.36}$$

where  $Z(\mu_\theta, \sigma_\theta)$  is a normalization constant to account for the finite domain. Finally, we define  $P(T_0)$  as a

---

<sup>†</sup>This assumption is predicated upon the hypothesis that the broadening effects of the transmission edge due to the spatial distribution of the particle beam are subdominant to those from the momentum distribution.

normal distribution with a mean value  $T_e$  chosen to be the user-selected electron gun energy, and empirically measured standard deviation  $\sigma_T = 0.076 \text{ eV}$ :

$$P(T_0; T_e, \sigma_T) = \frac{1}{\sigma_T \sqrt{2\pi}} e^{-\frac{(T_0 - T_e)^2}{2\sigma_T^2}}. \quad (6.37)$$

Combining the above formulae, we arrive at our final probability density function for the initial momentum states:

$$\begin{aligned} P_{occ}(T_0, \theta_0, \phi_0; T_e, \sigma_T, \mu_\theta, \sigma_\theta) &= \frac{1}{T_e \sqrt{2\pi}} e^{-\frac{(T_0 - T_e)^2}{2\sigma_T^2}} \times \\ &\times \frac{1}{Z(\mu_\theta, \sigma_\theta)} \cdot \frac{1}{\sigma_\theta \sqrt{2\pi}} e^{-\frac{(\theta_0 - \mu_\theta)^2}{2\sigma_\theta^2}} \times \\ &\times \frac{1}{2\pi}. \end{aligned} \quad (6.38)$$

### 6.3.3: Numerical Calculation of Transmission Function

By combining Equations 6.31 and 6.38, we arrive at an equation for the transmission fraction given both a spectrometer and an electron gun configuration:

$$P(\mathbf{c}_e, \mathbf{c}_s) = \int_0^\infty dT_0 \int_0^\pi d\theta_0 \int_0^{2\pi} d\phi_0 P_{occ}(T_0, \theta_0, \phi_0; \mathbf{c}_e) \times P_{trans}(T_0, \theta_0; \mathbf{c}_e, \mathbf{c}_s). \quad (6.39)$$

The integrations in Equation 6.39 can be computed numerically for discrete electron gun mean energies  $T_e$  sweeping through a configuration's transmission region (where  $P(\mathbf{c}_e, \mathbf{c}_s)$  increases from zero to one), yielding a set of points relating the particle beam's mean energy to the transmission fraction, in analogue to our measured data points.

## Section 6.4: Comparison of experimental data to simulation

### 6.4.1: Parametrized fits for measured and simulated data

During data taking, the number of transmitted electrons is recorded over a fixed time interval for discrete values of the electron gun voltage  $U_{egun} \equiv \frac{T_e}{e}$  that span the dynamic portion<sup>‡</sup> of the transmission function. Average values of the count rate are then taken for energies below and above the transmission edge, corresponding to a background rate and saturation rate of transmission, respectively. These values yield a

---

<sup>‡</sup>where the transmission function rises from zero to one

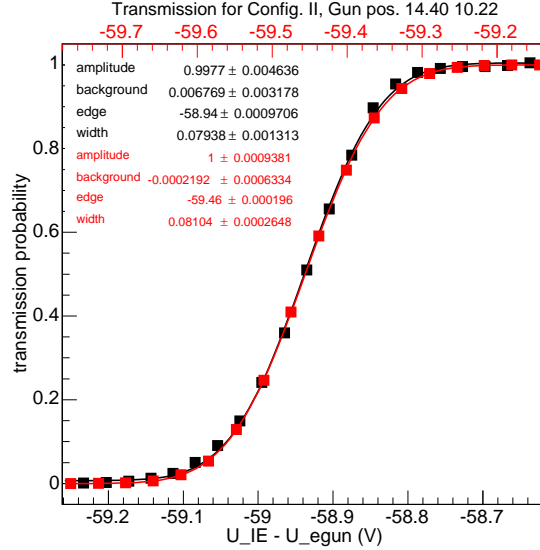


Figure 6.4: Measured (black) and simulated (red) transmission function profiles for Run 6176. Prior to simulation, the electron gun’s position was fit to minimize the difference in the measured and simulated energy edge for measurements corresponding to Configurations I and II (see Sec. 6.2.3).

constant offset and a linear scale with which the count rate can be normalized to a transmission fraction ranging from zero to one. Finally, the transmission fraction is plotted against the difference between the minimum potential of the main spectrometer’s electrode system (denoted  $U_{IE}$ , for inner electrode potential) and the electron gun voltage.

Once discrete values correlating the transmission fraction and the electron gun’s potential are obtained, we quantify the transmission function’s profile by fitting it to a parametrized function. Because MAC-E-Filters are integrating filters and our incident particle beam is normally distributed in energy, a reasonable choice for a parametrized fit function  $\mathcal{T}(U_{IE} - U_{egun})$  for our transmission points is

$$\mathcal{T}(U; a, b, \mu, \sigma) = \frac{a}{2} \left( 1 + \operatorname{erf} \left( \frac{U - \mu}{\sqrt{2}\sigma} \right) \right) + b, \quad (6.40)$$

where  $a$  parametrizes the amplitude,  $b$  is a constant background offset,  $\mu$  represents the midpoint of transmission (i.e. where 50% of the incident particles are transmitted),  $\sigma$  is a measure of the function’s width, and the error function is related to the integral of a normal distribution (10). As an example, Figure 6.4 depicts the measured and simulated transmission functions for Run 6176 in black and red, respectively. A complete set of measured and simulated transmission functions is provided in Appendix E.

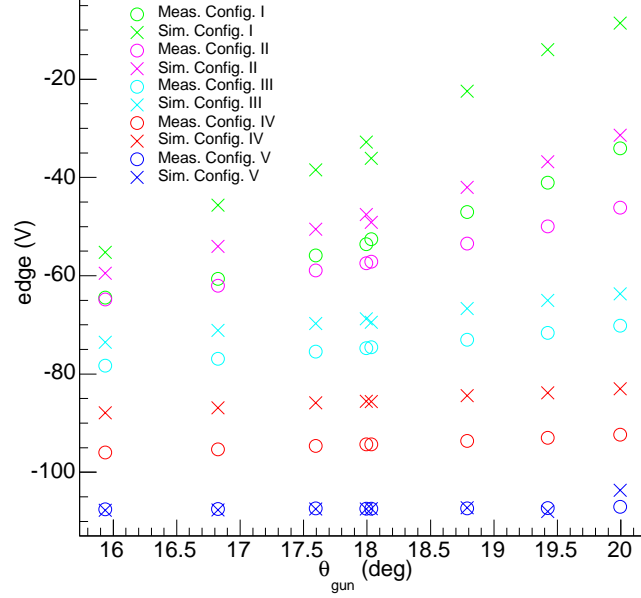


Figure 6.5: A comparison of the measured and simulated edge fit values with respect to  $\theta_{gun}$ , the angle between the electron gun’s manipulator arm and the beam axis. Simulations were performed with the electron gun parameters described in Table 6.1.

#### 6.4.2: Comparison of the transmission edge parameter

Figure 6.5 depicts a comparison of the fitted edge data (corresponding to the midpoint of the transmission threshold) using the values described in Table 6.1 for the electron gun position. The gun’s angular position is described by  $\theta_{gun}$ , the angle between the electron gun’s manipulator arm and the beam axis (see Fig. 6.1 (b)), given as

$$\theta_{gun} = \cos^{-1}(\cos \alpha_v \cos \alpha_h). \quad (6.41)$$

While it appears that the simulated edge values trend correctly with the gun angle, the offset between simulated and measured values suggests a possible misalignment in the simulated electron gun’s position. This misalignment does not appear to similarly affect the simulated values for Configuration V, however, implying that the transmission threshold for this configuration is caused by a different process.

#### 6.4.3: Mapping the analyzing surfaces

To better understand the transmission surfaces for each configuration, Figure 6.6 depicts the results of computing points on the analyzing surfaces for each configuration. From this simulation, we see that the analyzing surface for Configuration V is not caused by a potential minimum from the full metal electrode ring,

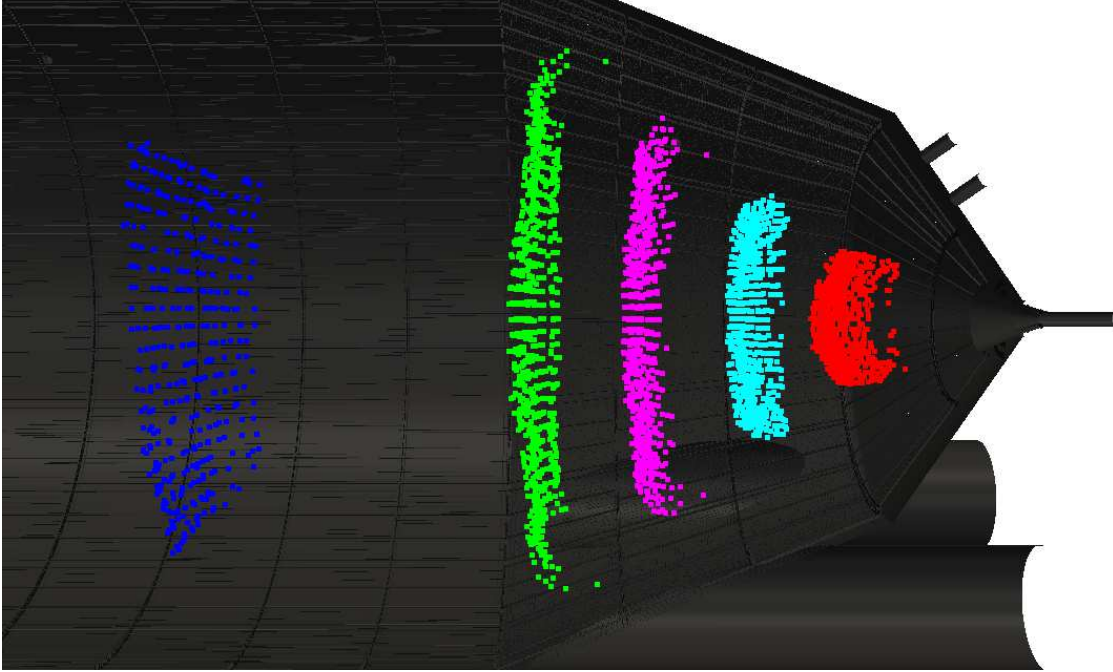


Figure 6.6: Simulated transmission surfaces from left to right: Configuration V (blue), I (green), II (magenta), III (cyan), IV (red).

but rather from a minimum in the magnetic field at the spectrometer's center. This implies that the proximity of the full metal electrode to the grounded anti-Penning electrode at the spectrometer's entrance prevents the formation of an electrostatic minimum in the downstream section of the spectrometer in Configuration V. Because of the relatively small variations in the electrostatic potential with respect to radial changes at the center of the spectrometer, the resultant transmission threshold for Configuration V is only weakly dependent upon the physical displacement of the electron gun.

#### 6.4.4: Fitting for the optimal gun position

Using the transmission function calculation routines described in Section 6.3, we can fit for the ideal offsets for the electron gun ( $x_m$  and  $y_m$  from Table 6.1). The technique we used to perform this fit is outlined below:

- For each electron gun configuration, we propagate along the magnetic field line that crosses through  $\mathbf{x}_{gun}$  to the entrance of the spectrometer, and label this point  $\mathbf{x}_0$ .
- Additionally, we propagate along the magnetic field line for the electron gun condition  $\alpha_v = \alpha_h = 0$  to the entrance of the spectrometer, and label this point  $\mathbf{x}_{origin}$ .
- For each transmission function measurement, we iteratively move our trajectory's initial position between



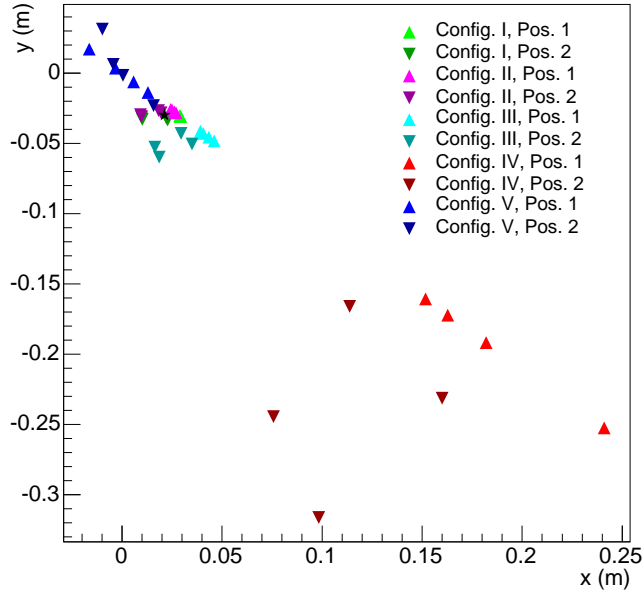


Figure 6.7: Starting positions for fixed threshold and  $\theta_{gun}$  for each run. The average position of Configurations I and II is represented by a black star.

$\mathbf{x}_0$  and  $\mathbf{x}_{origin}$  until the simulated and measured transmission thresholds agree to within a given tolerance.

- Once a position is found that reproduces the measured transmission threshold, we propagate backwards along the magnetic field line to identify its corresponding gun position.

parameter	symbol	value
$x$ -coordinate of electron gun offset	$x_m$	0.0056 m
$y$ -coordinate of electron gun offset	$y_m$	-0.0310 m

Table 6.3: Fitted electron gun parameters from Configurations I and II.

Figure 6.7 depicts the resulting starting positions for each measured transmission function. From Figure 6.5, we can see that the threshold fits for Configurations I and II are comparatively much more sensitive to variations in the electron gun’s initial position than Configurations III, IV and V (as evidenced by the span of the range for each configuration). As such, the results from fitting to the first two configurations were used to select an electron gun offset. Table 6.3 shows the results of this fit, and Figure 6.8 depicts the updated comparison between simulated and measured transmission thresholds after applying this offset correction.

While our fitted correction to the electron gun position results in a marked improvement in the comparison of simulated and measured transmission thresholds, we still see a substantial disagreement between the simulated and measured threshold values for Configuration IV. This discrepancy could be attributed to

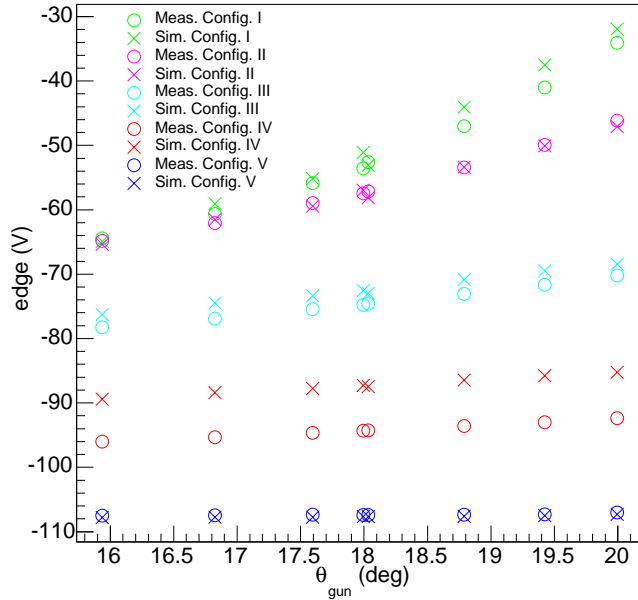


Figure 6.8: A comparison of the measured and simulated edge fit values with respect to  $\theta_{gun}$ , the angle between the electron gun’s manipulator arm and the beam axis. Simulations were performed with the electron gun parameters described in Table 6.3.

deviations in the as-built dimensions of the spectrometer compared to its corresponding CAD models. Were such a discrepancy to exist, its affect on the accuracy of the simulated electrostatic potential inside the flux tube would be most dramatic at the entrance and exit of the spectrometer, where the distances to surfaces are relatively smaller.

### Section 6.5: Conclusion

In this chapter, we analyze the results of experimentally measuring transmission functions for several non-standard electrostatic configurations of KATRIN’s main spectrometer, using an electron gun with position and energy selectivity. We began with a description of the experimental conditions under which the measurements were performed. We then derived a means for numerically computing the expectant transmission function using the main spectrometer model described in Chapter 5. Finally, we presented our experimental data in juxtaposition to our simulated results, fit for the position of the electron gun, and applied these corrections to our model. Our resultant comparison of measured to simulated data shows nice agreement for analyzing surfaces near  $z = 0$ , thus verifying our simulation’s ability to predict electrostatic fields inside the main spectrometer for standard run configurations (i.e. with symmetric electrostatic profiles). We posit that a discrepancy between CAD and as-built values for the dimensions of the spectrometer may explain

discrepancies observed for analyzing surfaces far from the center of the spectrometer.

## CHAPTER 7: Conclusion and Outlook

The KATRIN experiment employs electrostatic and magnetostatic fields with ubiquity throughout its apparatus to reach the scientific goal of probing the neutrino mass with a sensitivity of  $0.2\text{ eV}$  (90% C.L.). To generate these fields, large electrodes of complex design and multiple superconducting magnets have been built around KATRIN’s main spectrometer, one of the largest vessels at ultra-high vacuum in the world. We have developed several computational techniques to meet the challenges of performing simulations with the extreme range of geometric sizes and field strengths within the KATRIN spectrometer and detector systems.

To solve for electrostatic fields constrained by complicated surfaces, we have developed a Boundary Element Method that accepts Dirichlet, Neumann and mixed boundary conditions. This technique relies on the use of analytic solutions to discrete boundary integrals, which we present in Appendices A and B. The derivation of this method in Chapter 2 is intended to be sufficiently general enough to apply to other problems in potential theory, such as magnetostatics and the steady-state heat equation.

Complementing our BEM technique, we have derived the Robin Hood nonstationary linear algebraic solver. The Robin Hood solver is readily adapted to a high-performance computing environment, and can be implemented with a memory footprint that scales linearly with the dimension of the system. In comparison with other stationary and nonstationary solvers, we have demonstrated Robin Hood to be well suited to solving electrostatic BEM systems.

These methods have been implemented in the C++ software `KEMField`. `KEMField` is designed to be a flexible framework that is extensible to a broad class of linear partial differential equations. `KEMField` can operate independently with no required external dependencies; its functionality is extended by third-party software via an optional plugin model. Through this plugin design, support for cluster computing via MPI, GPU computing with OpenCL, and hybrid MPI-OpenCL are provided. There is also a plugin for `KGeoBag`, software we have designed to handle such geometry-related tasks as navigation and discretization.

In application of `KEMField` and `KGeoBag` to the KATRIN experiment, we have constructed full 3-dimensional models for both the detector section and main spectrometer, and have applied the BEM to these models on several high performance computing systems. As a result, simulations using these models have been successfully used to further KATRIN’s scientific goals via design validation and parameter optimization.

As a validation of our models, we have performed measurements designed to probe the electrostatic

properties of several locations within the main spectrometer. To analyze these measurements, we constructed a technique for reproducing these measurements in simulation. As a result of applying this technique to our measured results, we were able to identify potential deviations in our model from the as-built configuration.

There are several directions in which this research can be continued in order to further assist KATRIN in reaching its scientific goal. First (and perhaps most importantly), additional measurements like those described in Chapter 6 should be performed with a larger span of electron gun values. Currently, the measurement of transmission functions is the most precise technique available for characterizing the main spectrometer's electrostatic properties and, with enough data, our model could be parametrically fit to replicate the results of these measurements. Additionally, `KEMField`'s high performance BEM solvers can be applied to magnetostatic simulations, providing the KATRIN collaboration with the ability to more accurately model magnetic fields within the apparatus. Finally, the method of constructing meshes for KATRIN's apparatus could be improved by the implementation of iterative mesh refinement, allowing the results of a BEM computation to influence the sizes of mesh elements for subsequent BEM iterations.

## APPENDIX A: Analytic Integral Evaluation of Green's Functions over a Triangular Surface

### Section A.1: Definition of Initial Parameters

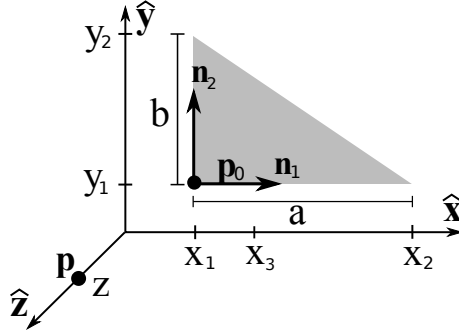


Figure A.1: A right triangular sub-element defined by the position of the corner opposite the hypotenuse  $\mathbf{p}_0$ , the lengths of the sides  $a$  and  $b$ , and the unit vectors in the directions of sides  $a$  and  $b$ , labeled  $\mathbf{n}_1$  and  $\mathbf{n}_2$ . The field point is defined as  $\mathbf{p}$ , with local coordinates  $(0, 0, z)$ . The corners of the triangle are recast into local coordinates to facilitate integration.

A right triangular surface  $\Delta\partial\Sigma$  is defined by the position of the vertex opposite the hypotenuse  $\mathbf{p}_0$ , the lengths of its sides  $a$  and  $b$ , and the unit vectors defining its sides  $\mathbf{n}_1$  and  $\mathbf{n}_2$  (see Fig. A.1). For the computation of the Green's function integrals at an observation point  $\mathbf{p}$ , it is necessary to transform into a local coordinate frame, where the triangle lies in the  $\hat{x}$ - $\hat{y}$  plane and the field point lies along the  $\hat{z}$ -axis, as depicted in Figure A.1. In the local coordinate system, the parameters necessary for the calculation are:

$$z = (\mathbf{p} - \mathbf{p}_0) \cdot \mathbf{n}_3, \quad (\text{A.1})$$

$$x_1 = (\mathbf{p}_0 - \mathbf{p}) \cdot \mathbf{n}_1, \quad (\text{A.2})$$

$$x_2 = x_1 + a, \quad (\text{A.3})$$

$$y_1 = \frac{z}{|z|} \cdot (\mathbf{p}_0 - \mathbf{p}) \cdot \mathbf{n}_2, \quad (\text{A.4})$$

$$y_2 = y_1 + \frac{z}{|z|} \cdot b, \quad (\text{A.5})$$

where  $\mathbf{n}_3 = \mathbf{n}_1 \times \mathbf{n}_2$ .

## Section A.2: Dirichlet Boundary Condition

The analytic calculation of the Dirichlet Green's function over a right triangular surface is performed as follows: the integral equation in terms of the local coordinates described in Figure A.1 is

$$\int_{\Delta\partial\Sigma} G(\mathbf{p}, \mathbf{x}') \cdot dS' = \int_{y_1}^{y_2} \int_{x_1}^{a+by} \frac{1}{\sqrt{x^2 + y^2 + z^2}} \cdot dx \cdot dy, \quad (\text{A.6})$$

where the upper limit of integration in  $x$ ,  $a + by$ , is the line describing the hypotenuse of the triangle. Using basic algebra, it can be seen that  $a = \frac{x_2 y_2 - x_1 y_1}{y_2 - y_1}$  and  $b = \frac{x_1 - x_2}{y_2 - y_1}$ . The inner integral can be evaluated as follows:

we first manipulate the equation into a more soluble form:

$$\begin{aligned} \int_{\Delta\partial\Sigma} G(\mathbf{p}, \mathbf{x}') \cdot dS' &= \int_{y_1}^{y_2} \int_{x_1}^{a+by} \frac{dx \cdot dy}{\sqrt{x^2 + (y^2 + z^2)}} = \\ &= \int_{y_1}^{y_2} dy \cdot \frac{1}{\sqrt{y^2 + z^2}} \int_{x_1}^{a+by} dx \cdot \frac{1}{\sqrt{\left(\frac{x}{\sqrt{y^2 + z^2}}\right)^2 + 1}}. \end{aligned} \quad (\text{A.7})$$

From here it is possible to substitute  $\frac{x}{\sqrt{y^2 + z^2}} = \sinh(u)$  and  $dx = \sqrt{y^2 + z^2} \cdot \cosh(u) \cdot du$ . Equation A.7 then becomes

$$\int_{\Delta\partial\Sigma} G(\mathbf{p}, \mathbf{x}') \cdot dS' = \int_{y_1}^{y_2} dy \int_{u_1}^{u_2} \frac{\cosh(u) \cdot du}{\sqrt{\sinh^2(u) + 1}}, \quad (\text{A.8})$$

where  $u_1 = \sinh^{-1}\left(\frac{x_1}{\sqrt{y^2 + z^2}}\right)$  and  $u_2 = \sinh^{-1}\left(\frac{a+by}{\sqrt{y^2 + z^2}}\right)$ . Using the identity

$$\cosh^2(x) - \sinh^2(x) = 1, \quad (\text{A.9})$$

Equation A.8 becomes

$$\begin{aligned} \int_{\Delta\partial\Sigma} G(\mathbf{p}, \mathbf{x}') \cdot dS' &= \int_{y_1}^{y_2} dy \int_{u_1}^{u_2} du = \\ &= \int_{y_1}^{y_2} dy \left[ \sinh^{-1}\left(\frac{a+by}{\sqrt{y^2 + z^2}}\right) - \sinh^{-1}\left(\frac{x_1}{\sqrt{y^2 + z^2}}\right) \right]. \end{aligned} \quad (\text{A.10})$$

After dividing by  $z$  to make the integral dimensionless, Equation A.10 becomes

$$\int_{\Delta\partial\Sigma} G(\mathbf{p}, \mathbf{x}') \cdot dS' = z \cdot \left[ \int_{u_1}^{u_2} du \cdot \sinh^{-1}\left(\frac{a' + bu}{\sqrt{u^2 + 1}}\right) - \int_{u_1}^{u_2} du \cdot \sinh^{-1}\left(\frac{x'_1}{\sqrt{u^2 + 1}}\right) \right], \quad (\text{A.11})$$

where  $a' = \frac{a}{z}$ ,  $u = \frac{y}{z}$ ,  $u_i = \frac{y_i}{z}$ , and  $x'_1 = \frac{x_1}{z}$ . If we define the following indefinite integrals

$$I_1(a, b, u) = \int \sinh^{-1} \left( \frac{a + bu}{\sqrt{u^2 + 1}} \right) \cdot du \quad (\text{A.12})$$

and

$$I_2(x, u) = \int \sinh^{-1} \left( \frac{x}{\sqrt{u^2 + 1}} \right) \cdot du, \quad (\text{A.13})$$

Equation A.11 can be rewritten as

$$\int_{\Delta\partial\Sigma} G(\mathbf{p}, \mathbf{x}') \cdot dS' = z \cdot [I_1(a', b, u_2) - I_1(a', b, u_1) - I_2(x'_1, u_2) + I_2(x'_1, u_1)]. \quad (\text{A.14})$$

### A.2.1: Integral $I_1(a, b, u)$

Integral  $I_1$  can be solved by following the steps outlined in (58). The steps are as follows:

Integral  $I_1$  can be converted into a more soluble integral by integrating by parts:

$$I_1(a, b, u) = \quad (\text{A.15})$$

$$= \int \sinh^{-1} \left( \frac{a + bu}{\sqrt{u^2 + 1}} \right) du = \quad (\text{A.16})$$

$$= u \cdot \sinh^{-1} \left( \frac{a + bu}{\sqrt{u^2 + 1}} \right) + \int \frac{(au^2 - bu) \cdot du}{((1 + a^2) + 2(ab)u + (1 + b^2)u^2)^{\frac{1}{2}} (u^2 + 1)}, \quad (\text{A.17})$$

or

$$I_1(a, b, u) = F_1(a, b, u) + I_3(a, b, u) - I_4(a, b, u), \quad (\text{A.18})$$

where

$$F_1(a, b, u) = u \cdot \sinh^{-1} \left( \frac{a + bu}{\sqrt{u^2 + 1}} \right), \quad (\text{A.19})$$

$$I_3(a, b, u) = \int \frac{au^2 \cdot du}{U^{\frac{1}{2}}(u^2 + 1)}, \quad (\text{A.20})$$

$$I_4(a, b, u) = \int \frac{bu \cdot du}{U^{\frac{1}{2}}(u^2 + 1)}, \quad (\text{A.21})$$

and the substitution

$$U = ((1 + a^2) + 2(ab)u + (1 + b^2)u^2) \quad (\text{A.22})$$



has been made merely to clarify the equations. By noting that  $I_3$  can be rewritten as

$$I_3(a, b, u) = a \cdot \left( \int \frac{du}{U^{\frac{1}{2}}} - \int \frac{du}{U^{\frac{1}{2}}(u^2 + 1)} \right), \quad (\text{A.23})$$

we can move the second term into  $I_4$ , leaving us with

$$I_1(a, b, u) = F_1(a, b, u) + \tilde{I}_3(a, b, u) - \tilde{I}_4(a, b, u), \quad (\text{A.24})$$

where

$$\tilde{I}_3(a, b, u) = \int \frac{a \cdot du}{U^{\frac{1}{2}}}, \quad (\text{A.25})$$

$$\tilde{I}_4(a, b, u) = \int \frac{(bu + a) \cdot du}{U^{\frac{1}{2}}(u^2 + 1)}, \quad (\text{A.26})$$

#### A.2.2: Integral $\tilde{I}_3(a, b, u)$

By affecting a change in variables,

$$a' = 1 + b^2, \quad (\text{A.27})$$

$$b' = 2ab, \quad (\text{A.28})$$

$$c' = 1 + a^2, \quad (\text{A.29})$$

$\tilde{I}_3$  can be cast into a form readily found in tables of integrals:

$$\frac{\tilde{I}_3}{a} = \int \frac{du}{\sqrt{a'u^2 + b'u + c'}}. \quad (\text{A.30})$$

The general solution to this integral for  $a' > 0$  is taken from (59) to be

$$\int \frac{du}{\sqrt{a'u^2 + b'u + c'}} = \frac{1}{\sqrt{a'}} \ln \left( 2a'u + b' + 2\sqrt{a'} \sqrt{a'u^2 + b'u + c'} \right). \quad (\text{A.31})$$

Recast into our variables of interest, we arrive at an equation for  $\tilde{I}_3$ :

$$\tilde{I}_3(a, b, u) = \frac{a \ln \left( 2 \left( \sqrt{b^2 + 1} \sqrt{a^2 + 2abu + (b^2 + 1)u^2 + 1} + b(a + bu) + u \right) \right)}{\sqrt{b^2 + 1}}. \quad (\text{A.32})$$

A.2.3: Integral  $\tilde{I}_4(a, b, u)$

Integral  $\tilde{I}_4$  is in a form that can be solved analytically by performing the following change of variables:

$$a' = 1 + b^2, \quad (\text{A.33})$$

$$b' = ab, \quad (\text{A.34})$$

$$c' = 1 + a^2, \quad (\text{A.35})$$

$$h = b, \quad (\text{A.36})$$

$$k = a. \quad (\text{A.37})$$

The integral is now

$$\tilde{I}_4 = \int \frac{(hu + k)du}{(u^2 + 1)\sqrt{a'u^2 + 2b'u + c'}}, \quad (\text{A.38})$$

and can be solved using the technique outlined in (60):

Making the substitutions

$$u \rightarrow \frac{\lambda t + 1}{t - \lambda}, \quad du \rightarrow -\frac{(\lambda^2 + 1)}{(t - \lambda)^2} dt \quad (\text{A.39})$$

in the equation and recovering the form

$$\tilde{I}_4 = \int \frac{(lt + m)dt}{(t^2 + 1)\sqrt{\alpha t^2 + 2\beta t + \gamma}} \quad (\text{A.40})$$

goes as follows:

$$\tilde{I}_4 = \int \frac{\left(h \frac{(\lambda t + 1)}{(t - \lambda)} + k\right) \frac{-(\lambda^2 + 1)}{(t - \lambda)^2} dt}{\left(\frac{(\lambda t + 1)^2}{(t - \lambda)^2} + 1\right) \sqrt{a' \frac{(\lambda t + 1)^2}{(t - \lambda)^2} + 2b' \frac{(\lambda t + 1)}{(t - \lambda)} + c'}} = \quad (\text{A.41})$$

$$= \int \frac{\frac{-(\lambda^2 + 1)}{(t - \lambda)^3} (h(\lambda t + 1) + k(t - \lambda)) dt}{\left(\frac{(\lambda t + 1)^2}{(t - \lambda)^2} + 1\right) \sqrt{a' \frac{(\lambda t + 1)^2}{(t - \lambda)^2} + 2b' \frac{(\lambda t + 1)}{(t - \lambda)} + c'}} = \quad (\text{A.42})$$

$$= \int \frac{(\lambda^2 + 1) (-(h\lambda + k)t + (k\lambda - h)) dt}{(t - \lambda)^3 \left(\frac{(\lambda t + 1)^2}{(t - \lambda)^2} + 1\right) \sqrt{a' \frac{(\lambda t + 1)^2}{(t - \lambda)^2} + 2b' \frac{(\lambda t + 1)}{(t - \lambda)} + c'}} = \quad (\text{A.43})$$

$$= \int \frac{(\lambda^2 + 1) (-(h\lambda + k)t + (k\lambda - h)) dt}{((\lambda t + 1)^2 + (t - \lambda)^2) \sqrt{a'(\lambda t + 1)^2 + 2b'(\lambda t + 1)(t - \lambda) + c'(t - \lambda)^2}} = \quad (\text{A.44})$$

$$= \int \frac{(\lambda^2 + 1) (-(h\lambda + k)t + (k\lambda - h)) dt}{(\lambda^2 t^2 + 1 + t^2 + \lambda^2) \sqrt{\lambda^2 t^2 a' + 2\lambda t a' + a' + 2b' \lambda t^2 - 2b' \lambda^2 t + t b' t - 2b' \lambda + c' t^2 - 2c' \lambda t + c' \lambda^2}} =$$

$$= \int \frac{(-(h\lambda + k)t + (k\lambda - h)) dt}{(t^2 + 1) \sqrt{(\lambda^2 a' + 2b' \lambda + c') t^2 + 2(-b' \lambda^2 + (a' - c') \lambda + b') t + (a' - 2b' \lambda + c' \lambda^2)}} \quad (\text{A.45})$$

We can see from the Equation A.45 that

$$l = -h\lambda - k = -b\lambda - a, \quad (\text{A.46})$$

$$m = k\lambda - h = a\lambda - b, \quad (\text{A.47})$$

$$\alpha = \lambda^2 a' + 2b'\lambda + c' = (1+b^2)\lambda^2 + 2(ab)\lambda + (1+a^2), \quad (\text{A.48})$$

$$\beta = -b'\lambda^2 + (a' - c')\lambda + b', \quad (\text{A.49})$$

$$\gamma = a' - 2b'\lambda + c'\lambda^2 = (1+b^2) - 2(ab)\lambda + (1+a^2)\lambda^2. \quad (\text{A.50})$$

Now, if we let  $\lambda$  equal one of the roots of  $\beta$ ,

$$\lambda = \frac{(a' - c') \pm \sqrt{(c' - a')^2 + 4b'^2}}{2b'} = \quad (\text{A.51})$$

$$= \left(\frac{b}{a}\right) \text{ or } \left(-\frac{a}{b}\right), \quad (\text{A.52})$$

we can remove  $\beta$  from Equation A.40 and split the integral into two parts:

$$\tilde{I}_4 = \int \frac{t dt}{(t^2 + 1)\sqrt{\alpha t^2 + \gamma}} + \int \frac{m dt}{(t^2 + 1)\sqrt{\alpha t^2 + \gamma}}. \quad (\text{A.53})$$

The second integral can be put in the same form as the first if we affect another change of variables,  $t \rightarrow \frac{1}{s}$ , and take  $t > 0$ ,  $s > 0$ :

$$\tilde{I}_4 = \int \frac{t dt}{(t^2 + 1)\sqrt{\alpha t^2 + \gamma}} - \int \frac{m ds}{(s^2 + 1)\sqrt{\gamma s^2 + \alpha}}. \quad (\text{A.54})$$

Solutions to integrals of this form are as defined as

$$\int \frac{t dt}{(t^2 + 1)\sqrt{\xi t^2 + \zeta}} = \frac{\tan^{-1}\left(\sqrt{\frac{\xi t^2 + \zeta}{\xi - \zeta}}\right)}{\sqrt{\xi - \zeta}}. \quad (\text{A.55})$$

Using Equation A.55 and taking the more positive root of  $\beta$  ( $\lambda = \frac{b}{a}$ ), we arrive at a closed form solution for  $\tilde{I}_4$ :

$$\tilde{I}_4(a, b, u) = -\left(\frac{b^2}{a} + a\right) \cdot \frac{1}{\sqrt{\alpha - \gamma}} \cdot \tan^{-1}\left(\sqrt{\frac{\alpha t^2 + \gamma}{\alpha - \gamma}}\right), \quad (\text{A.56})$$

where

$$\begin{aligned}
\alpha &= \frac{(a^2 + b^2)(a^2 + b^2 + 1)}{a^2}, \\
\gamma &= 1 + \frac{b^2}{a^2}, \\
t &= -\left(\frac{bu + a}{au - b}\right).
\end{aligned} \tag{A.57}$$

For consistency, the solution to  $I_3$  using the more negative root of  $\beta$  ( $\lambda = -\frac{a}{b}$ ) is

$$\tilde{I}_4(a, b, u) = \left(\frac{a^2}{b} + b\right) \cdot \frac{1}{\sqrt{\gamma' - \alpha'}} \cdot \tan^{-1} \left( \sqrt{\frac{\gamma' s^2 + \alpha'}{\gamma' - \alpha'}} \right), \tag{A.58}$$

where

$$\begin{aligned}
\alpha' &= 1 + \frac{a^2}{b^2} = \frac{a^2}{b^2} \gamma, \\
\gamma' &= \frac{(a^2 + b^2)(a^2 + b^2 + 1)}{b^2} = \frac{a^2}{b^2} \alpha, \\
s &= \frac{bu + a}{au - b} = -t.
\end{aligned} \tag{A.59}$$

As expected, the answers derived from using the two roots of  $\beta$  are equivalent. Since  $a$  corresponds to the  $x$ -intercept of the hypotenuse and  $b$  represents the inverted slope, it is safer to use Equation A.58, ensuring that there is never a division by zero.

To further reduce the number of necessary computations, it is possible to obtain an analytic solution for  $(\tilde{I}_4(a, b, u_2) - \tilde{I}_4(a, b, u_1))$ , as is explained in the next subsection.

#### A.2.4: $\tilde{I}_4(a, b, u_2) - \tilde{I}_4(a, b, u_1)$

First, we shall take the solution of  $\tilde{I}_4(a, b, u)$  described in Equation A.56 (since we have shown that Equations A.56 and A.58 are equivalent, we lose no generality in this assumption). We then have

$$\tilde{I}_4(a, b, u_2) - \tilde{I}_4(a, b, u_1) = \left( \left( \frac{a^2}{b} + b \right) \cdot \frac{1}{\sqrt{\gamma' - \alpha'}} \right) \cdot \left( \tan^{-1} \left( \sqrt{\frac{\alpha t_2^2 + \gamma}{\alpha - \gamma}} \right) - \tan^{-1} \left( \sqrt{\frac{\alpha t_1^2 + \gamma}{\alpha - \gamma}} \right) \right), \tag{A.60}$$

where  $\alpha, \gamma, t_1$ , and  $t_2$  are described by Equations A.57. Using the formulas

$$\begin{aligned}
\tan^{-1}(u) + \tan^{-1}(v) &= \tan^{-1} \left( \frac{u + v}{1 - uv} \right), \\
\tan^{-1}(-v) &= -\tan^{-1}(v),
\end{aligned} \tag{A.61}$$

Equation A.60 can be rewritten as

$$\begin{aligned}
\tilde{I}_4(a, b, u_2) - \tilde{I}_4(a, b, u_1) &= - \left( \left( \frac{b^2}{a} + a \right) \cdot \frac{1}{\sqrt{\alpha - \gamma}} \right) \cdot \left( \tan^{-1} \left( \frac{\sqrt{\frac{\alpha t_2^2 + \gamma}{\alpha - \gamma}} - \sqrt{\frac{\alpha t_1^2 + \gamma}{\alpha - \gamma}}}{1 + \frac{\sqrt{\alpha t_2^2 + \gamma} \cdot \sqrt{\alpha t_1^2 + \gamma}}{\alpha - \gamma}} \right) \right) = \\
&= - \left( \left( \frac{b^2}{a} + a \right) \cdot \frac{1}{\sqrt{\alpha - \gamma}} \right) \cdot \left( \tan^{-1} \left( \frac{\sqrt{\alpha - \gamma} \cdot \left( \sqrt{\alpha t_2^2 + \gamma} - \sqrt{\alpha t_1^2 + \gamma} \right)}{(\alpha - \gamma) + \sqrt{\alpha t_2^2 + \gamma} \cdot \sqrt{\alpha t_1^2 + \gamma}} \right) \right)
\end{aligned}$$

### A.2.5: Integral $I_2(x, u)$

The techniques used to solve  $I_2(x, u)$  are similar to the ones described in Section A.2.1. We begin by first integrating by parts:

$$I_2(x, u) = \int \sinh^{-1} \left( \frac{x}{\sqrt{u^2 + 1}} \right) \cdot du = \tag{A.62}$$

$$= u \cdot \sinh^{-1} \left( \frac{x}{\sqrt{u^2 + 1}} \right) + \int \frac{u^2 x \cdot du}{(u^2 + 1) \sqrt{u^2 + (x^2 + 1)}} = \tag{A.63}$$

$$= F_1(x, 0, u) + I_5(x, u), \tag{A.64}$$

where  $F_1$  is defined by Equation A.19, and

$$I_5(x, u) = \int \frac{u^2 x \cdot du}{(u^2 + 1) \sqrt{u^2 + (x^2 + 1)}}. \tag{A.65}$$

By noting that

$$I_5(x, u) = x \cdot \left( \int \frac{du}{\sqrt{u^2 + (x^2 + 1)}} - \int \frac{du}{(u^2 + 1) \sqrt{u^2 + (x^2 + 1)}} \right) = \tag{A.66}$$

$$= x \cdot (I_6(x, u) + I_7(x, u)), \tag{A.67}$$

we can apply Equation A.31 to  $I_6$  and, after affecting a change of variables  $u \rightarrow \frac{1}{t}$  and keeping  $u, t > 0$ , we can apply Equation A.55 to  $I_7$ , as demonstrated below:

$$I_6(x, u) = \ln \left( 2 \left( \sqrt{u^2 + x^2 + 1} + u \right) \right), \tag{A.68}$$

and

$$I_7(x, u) = - \int \frac{du}{(u^2 + 1)\sqrt{u^2 + (x^2 + 1)}} = \quad (\text{A.69})$$

$$= \int \frac{t \cdot dt}{(t^2 + 1)\sqrt{(x^2 + 1)t^2 + 1}} = \quad (\text{A.70})$$

$$= \frac{\tan^{-1} \left( \sqrt{\frac{(x^2 + 1)t^2 + 1}{x^2}} \right)}{|x|}. \quad (\text{A.71})$$

### A.2.6: Limiting Case: $z = 0$

When  $z = 0$ , the above formalism cannot be applied, since it would involve a division by zero. Instead, we start with a modified version of Equation A.10:

$$\int_{\Delta\partial\Sigma} G(\mathbf{p}, \mathbf{x}') \cdot dS' = \int_{y_1}^{y_2} dy \left[ \sinh^{-1} \left( \frac{a + by}{|y|} \right) - \sinh^{-1} \left( \frac{x_1}{|y|} \right) \right], \quad (\text{A.72})$$

where the parameters are defined in the same way as in Section B.1. These two integrals can be made more soluble by integrating by parts:

$$\begin{aligned} \int_{\Delta\partial\Sigma} G(\mathbf{p}, \mathbf{x}') \cdot dS' &= \left[ y \cdot \sinh^{-1} \left( \frac{a + by}{|y|} \right) + \int_{y_1}^{y_2} \frac{dy}{\sqrt{(1 + b^2)y^2 + (2ab)y + a^2}} - \right. \\ &\quad \left. - y \cdot \sinh^{-1} \left( \frac{x_1}{|y|} \right) - \int_{y_1}^{y_2} \frac{x_1 \cdot dy}{\sqrt{y^2 + x_1^2}} \right]. \end{aligned} \quad (\text{A.73})$$

The first integral in Equation A.73 can be performed using Equation A.31, while the second integral can be performed via trigonometric substitution. The resulting formula at  $z = 0$  is

$$\begin{aligned} \int_{\Delta\partial\Sigma} G(\mathbf{p}, \mathbf{x}') \cdot dS' &= \left[ y \cdot \sinh^{-1} \left( \frac{a + by}{|y|} \right) + \right. \\ &\quad \frac{a}{\sqrt{1 + b^2}} \cdot \ln \left( 2(1 + b^2)y + 2ab + 2\sqrt{1 + b^2} \sqrt{(1 + b^2)y^2 + 2aby + a^2} \right) - \\ &\quad \left. - y \cdot \sinh^{-1} \left( \frac{x_1}{|y|} \right) - x_1 \cdot \sinh^{-1} \left( \frac{y}{|x_1|} \right) \right]_{y_1}^{y_2}. \end{aligned} \quad (\text{A.74})$$

### Section A.3: Extension to Non-Right triangles

To extend our previous results to include non-right triangles, we must first define a general triangle in local coordinates:

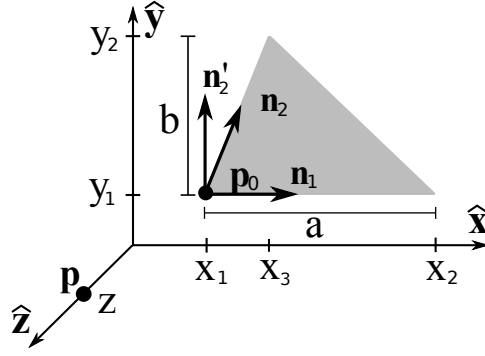


Figure A.2: A non-right triangular sub-element defined by a corner  $\mathbf{p}_0$ , the length of the longest side  $a$  and corresponding height  $b$ , and the unit vectors in the directions of the sides connected to  $\mathbf{p}_0$ , labeled  $\mathbf{n}_1$  and  $\mathbf{n}_2$  ( $\mathbf{n}_1$  always points in the direction of  $a$ ). The field point is defined as  $\mathbf{p}$ , with local coordinates  $(0,0,z)$ . The corners of the triangle are recast into local coordinates to facilitate integration.

$$z = (\mathbf{p} - \mathbf{p}_0) \cdot \mathbf{n}_3, \quad (\text{A.75})$$

$$x_1 = (\mathbf{p}_0 - \mathbf{p}) \cdot \mathbf{n}_1, \quad (\text{A.76})$$

$$x_2 = x_1 + a, \quad (\text{A.77})$$

$$x_3 = x_1 + (\mathbf{n}_1 \cdot \mathbf{n}_2) \cdot b, \quad (\text{A.78})$$

$$y_1 = \frac{z}{|z|} \cdot (\mathbf{p}_0 - \mathbf{p}) \cdot \mathbf{n}'_2, \quad (\text{A.79})$$

$$y_2 = y_1 + \frac{z}{|z|} \cdot b, \quad (\text{A.80})$$

where  $\mathbf{n}_3 = \mathbf{n}_1 \times \mathbf{n}_2$ , and  $\mathbf{n}'_2$  is the unit normal to  $\mathbf{n}_1$  in the direction of  $\mathbf{n}_2$  ( $\mathbf{n}'_2 = \frac{\mathbf{n}_2 - (\mathbf{n}_2 \cdot \mathbf{n}_1) \mathbf{n}_1}{|\mathbf{n}_2 - (\mathbf{n}_2 \cdot \mathbf{n}_1) \mathbf{n}_1|}$ ).

The analytic calculation of the Dirichlet Green's function integral over this triangle can be computed as the sum of the potentials from two right triangles: applying Equation A.6 using the local coordinates described in Figure A.2, we get

$$\begin{aligned} \int_{\Delta\partial\Sigma} G(\mathbf{p}, \mathbf{x}') \cdot dS' &= \left( \int_{y_1}^{y_2} \int_{a_1+b_1y}^{x_3} \frac{1}{\sqrt{x^2 + y^2 + z^2}} \cdot dx \cdot dy + \right. \\ &\quad \left. + \int_{y_1}^{y_2} \int_{x_3}^{a_2+b_2y} \frac{1}{\sqrt{x^2 + y^2 + z^2}} \cdot dx \cdot dy \right) = \\ &= \left( \int_{y_1}^{y_2} \int_{a_1+b_1y}^{a_2+b_2y} \frac{1}{\sqrt{x^2 + y^2 + z^2}} \cdot dx \cdot dy \right), \end{aligned} \quad (\text{A.81})$$

where  $a_1 = \frac{x_1 y_2 - x_3 y_1}{(y_2 - y_1)}$ ,  $a_2 = \frac{x_2 y_2 - x_3 y_1}{(y_2 - y_1)}$ ,  $b_1 = \frac{x_3 - x_1}{y_2 - y_1}$  and  $b_2 = \frac{x_3 - x_2}{y_2 - y_1}$ . Evaluating the first integral, we use

Equation A.11 to get

$$\int_{\Delta\partial\Sigma} G(\mathbf{p}, \mathbf{x}') \cdot dS' = z \cdot \left[ \int_{u_1}^{u_2} du \cdot \sinh^{-1} \left( \frac{a'_2 + b_2 u}{\sqrt{u^2 + 1}} \right) - \int_{u_1}^{u_2} du \cdot \sinh^{-1} \left( \frac{a'_1 + b_1 u}{\sqrt{u^2 + 1}} \right) \right], \quad (\text{A.82})$$

where  $a'_1 = \frac{a_1}{z}$ ,  $a'_2 = \frac{a_2}{z}$ ,  $u = \frac{y}{z}$  and  $u_i = \frac{y_i}{z}$ . Using Equation A.12, the solution to this integral is

$$\int_{\Delta\partial\Sigma} G(\mathbf{p}, \mathbf{x}') \cdot dS' = z \cdot [I_1(a'_2, b_2, u_2) - I_1(a'_2, b_2, u_1) - I_1(a'_1, b_1, u_2) + I_1(a'_1, b_1, u_1)]. \quad (\text{A.83})$$

For the case  $z \rightarrow 0$ , our solution becomes

$$\begin{aligned} \int_{\Delta\partial\Sigma} G(\mathbf{p}, \mathbf{x}') \cdot dS' &= \left[ y \cdot \sinh^{-1} \left( \frac{a + by}{|y|} \right) + \right. \\ &\quad \left. \frac{a}{\sqrt{1+b^2}} \cdot \ln \left( 2(1+b^2)y + 2ab + 2\sqrt{1+b^2} \sqrt{(1+b^2)y^2 + 2aby + a^2} \right) - \right. \\ &\quad \left. - y \cdot \sinh^{-1} \left( \frac{x_1}{|y|} \right) - x_1 \cdot \sinh^{-1} \left( \frac{y}{|x_1|} \right) \right]_{y_1}^{y_2}. \end{aligned} \quad (\text{A.84})$$

#### Section A.4: Neumann Boundary Condition

Using the same local parameters as in Section B.1, the integral equation for the Neumann boundary condition is given by

$$\int_{\Delta\partial\Sigma} \nabla G(\mathbf{p}, \mathbf{x}') \cdot dS' = \int_{y_1}^{y_2} dy \int_{x_1}^{a+by} dx \cdot \frac{x\hat{\mathbf{x}} + y\hat{\mathbf{y}} - z\hat{\mathbf{z}}}{(x^2 + y^2 + z^2)^{\frac{3}{2}}}. \quad (\text{A.85})$$

From Equation A.85, we begin by computing the x-component:

$$\begin{aligned} \int_{\Delta\partial\Sigma} \hat{\mathbf{x}} \cdot \nabla G(\mathbf{p}, \mathbf{x}') \cdot dS' &= \int_{y_1}^{y_2} dy \int_{x_1}^{a+by} dx \cdot \frac{x}{(x^2 + y^2 + z^2)^{\frac{3}{2}}} = \\ &= \int_{y_1}^{y_2} dy \left( \frac{-1}{\sqrt{x^2 + y^2 + z^2}} \Big|_{x_1}^{a+by} \right) = \\ &= - \left( \int_{y_1}^{y_2} \frac{dy}{\sqrt{(b^2+1)y^2 + (2ab)y + (a^2+z^2)}} - \int_{y_1}^{y_2} \frac{dy}{\sqrt{x_1^2 + y^2 + z^2}} \right) = \\ &= \frac{-z}{a' \cdot |z|} \cdot (\tilde{I}_3(a', b, u_2) - \tilde{I}_3(a', b, u_1)) - \frac{z}{|z|} \cdot (I_6(x'_1, u_2) - I_6(x'_1, u_1)). \end{aligned}$$



The y-component can be computed as follows:

$$\begin{aligned}
\int_{\Delta\partial\Sigma} \hat{\mathbf{y}} \cdot \nabla G(\mathbf{p}, \mathbf{x}') \cdot dS' &= \int_{y_1}^{y_2} dy \int_{x_1}^{a+by} dx \cdot \frac{y}{(x^2 + y^2 + z^2)^{\frac{3}{2}}} = \\
&= \int_{y_1}^{y_2} dy \left( \frac{y \cdot x}{(y^2 + z^2) \sqrt{x^2 + y^2 + z^2}} \Big|_{x_1}^{a+by} \right) = \\
&= \left( \int_{y_1}^{y_2} dy \frac{by^2 + ay}{(y^2 + z^2) \sqrt{(b^2 - 1)y^2 + 2(ab)y + (a^2 + z^2)}} - \right. \\
&\quad \left. - \int_{y_1}^{y_2} dy \frac{x_1 y}{(y^2 + z^2) \sqrt{y^2 + x_1^2 + z^2}} \right) = \\
&= \left( \int_{u_1}^{u_2} du \frac{bu^2 + a'u}{(u^2 + 1) \sqrt{(b^2 - 1)u^2 + 2(a'b)u + (a'^2 + 1)}} - \right. \\
&\quad \left. - \int_{u_1}^{u_2} du \frac{x'_1 u}{(u^2 + 1) \sqrt{u^2 + x'_1{}^2 + 1}} \right) = \\
&= (J_1(a, b, u_1, u_2) - J_2(x'_1, u_1, u_2)). \tag{A.86}
\end{aligned}$$

Solving  $J_1$ :

$$\begin{aligned}
J_1(a, b, u_1, u_2) &= \int_{u_1}^{u_2} du \frac{bu^2 + a'u}{(u^2 + 1) \sqrt{(b^2 - 1)u^2 + 2(a'b)u + (a'^2 + 1)}} \\
&= \int_{u_1}^{u_2} du \frac{b(u^2 + 1) + (a'u - b)}{(u^2 + 1) \sqrt{(b^2 - 1)u^2 + 2(a'b)u + (a'^2 + 1)}} = \\
&= b \cdot \int_{u_1}^{u_2} du \frac{1}{\sqrt{(b^2 - 1)u^2 + 2(a'b)u + (a'^2 + 1)}} + \\
&\quad + \int_{u_1}^{u_2} du \frac{a'u - b}{(u^2 + 1) \sqrt{(b^2 - 1)u^2 + 2(a'b)u + (a'^2 + 1)}}, \tag{A.87}
\end{aligned}$$

which can be recast into  $\tilde{I}_3$  and  $\tilde{I}_4$  from earlier. To solve  $J_2$ :

$$\begin{aligned}
J_2(x'_1, u_1, u_2) &= \int_{u_1}^{u_2} du \frac{x'_1 u}{(u^2 + 1) \sqrt{u^2 + x_1'^2 + 1}} \\
&= x'_1 \cdot \int_{\zeta_1}^{\zeta_2} d\zeta \frac{\zeta}{(\zeta^2 - x_1'^2 - 1 + 1) |\zeta|} = \quad (\text{where } \zeta^2 = u^2 + x_1'^2 + 1) \\
&= x'_1 \cdot \int_{\zeta_1}^{\zeta_2} \frac{d\zeta}{\zeta^2 - x_1'^2} = \\
&= \frac{x'_1}{2|x'_1|} \cdot \left( \ln \left( \frac{\zeta - |x'_1|}{\zeta + |x'_1|} \right) \right) \Big|_{\zeta_1}^{\zeta_2} = \\
&= \frac{x'_1}{2|x'_1|} \cdot \ln \left( \frac{\left( \sqrt{u_2^2 + x_1'^2 + 1} - |x'_1| \right) \left( \sqrt{u_1^2 + x_1'^2 + 1} + |x'_1| \right)}{\left( \sqrt{u_2^2 + x_1'^2 + 1} + |x'_1| \right) \left( \sqrt{u_1^2 + x_1'^2 + 1} - |x'_1| \right)} \right). \tag{A.88}
\end{aligned}$$

Finally, the z-component is

$$\begin{aligned}
\int_{\Delta\partial\Sigma} \hat{\mathbf{z}} \cdot \nabla G(\mathbf{p}, \mathbf{x}') \cdot dS' &= \int_{y_1}^{y_2} dy \int_{x_1}^{a+by} dx \cdot \frac{-z}{(x^2 + y^2 + z^2)^{\frac{3}{2}}} = \\
&= \int_{y_1}^{y_2} dy \left( \frac{-z \cdot x}{(y^2 + z^2) \sqrt{x^2 + y^2 + z^2}} \Big|_{x_1}^{a+by} \right). \tag{A.89}
\end{aligned}$$

Dividing out by  $z$  to make the integral more soluble, we get

$$\begin{aligned}
&\int_{\Delta\partial\Sigma} \hat{\mathbf{z}} \cdot \nabla G(\mathbf{p}, \mathbf{x}') \cdot dS' = \\
&= -z \cdot \int_{u_1}^{u_2} du \cdot \left( \frac{z^2 \cdot x'}{z^3 (u^2 + 1) \sqrt{u^2 + x_1'^2 + 1}} \Big|_{x_1'}^{a'+bu} = \right. \\
&= - \int_{u_1}^{u_2} du \cdot \left( \frac{x'}{(u^2 + 1) \sqrt{u^2 + x_1'^2 + 1}} \Big|_{x_1'}^{a'+bu} = \right. \\
&= \int_{u_1}^{u_2} du \cdot \left( \frac{a' + bu}{(u^2 + 1) \sqrt{(b^2 + 1)u^2 + 2(a'b)u + (a'^2 + 1)}} - \frac{x_1'}{(u^2 + 1) \sqrt{u^2 + (x_1'^2 + 1)}} \right) \\
&= -(\tilde{I}_4(a', b, u_1) - \tilde{I}_4(a', b, u_2)) - x'_1 \cdot (I_7(x'_1, u_1) - I_7(x'_1, u_2)). \tag{A.90}
\end{aligned}$$

## APPENDIX B: Analytic Integral Evaluation of Green's Functions over a Rectangular Surface

### Section B.1: Definition of Initial Parameters

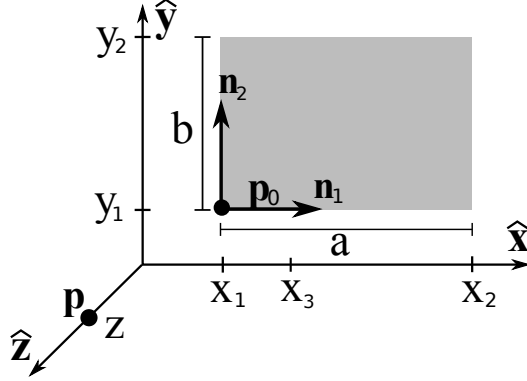


Figure B.1: A rectangular sub-element defined by the position of the corner opposite the hypotenuse  $\mathbf{p}_0$ , the lengths of the sides  $a$  and  $b$ , and the unit vectors in the directions of sides  $a$  and  $b$ , labeled  $\mathbf{n}_1$  and  $\mathbf{n}_2$ . The field point is defined as  $\mathbf{p}$ , with local coordinates  $(0, 0, z)$ . The corners of the triangle are recast into local coordinates to facilitate integration.

A rectangular surface  $\Delta\partial\Sigma$  is defined by the position of the vertex opposite the hypotenuse  $\mathbf{p}_0$ , the lengths of its sides  $a$  and  $b$ , and the unit vectors defining its sides  $\mathbf{n}_1$  and  $\mathbf{n}_2$  (see Fig. B.1). For the computation of the Green's function integrals at an observation point  $\mathbf{p}$ , it is necessary to transform into a local coordinate frame, where the triangle lies in the  $\hat{x}$ - $\hat{y}$  plane and the field point lies along the  $\hat{z}$ -axis, as depicted in Figure B.1. In the local coordinate system, the parameters necessary for the calculation are:

$$z = (\mathbf{p} - \mathbf{p}_0) \cdot \mathbf{n}_3, \quad (\text{B.1})$$

$$x_1 = (\mathbf{p}_0 - \mathbf{p}) \cdot \mathbf{n}_1, \quad (\text{B.2})$$

$$x_2 = x_1 + a, \quad (\text{B.3})$$

$$y_1 = \frac{z}{|z|} \cdot (\mathbf{p}_0 - \mathbf{p}) \cdot \mathbf{n}_2, \quad (\text{B.4})$$

$$y_2 = y_1 + \frac{z}{|z|} \cdot b, \quad (\text{B.5})$$

where  $\mathbf{n}_3 = \mathbf{n}_1 \times \mathbf{n}_2$ .

## Section B.2: Dirichlet Boundary Condition

The analytic calculation of the Dirichlet Green's function over a rectangular surface is performed as follows: the integral equation in terms of the local coordinates described in Figure B.1 is

$$\int_{\Delta\partial\Sigma} G(\mathbf{p}, \mathbf{x}') \cdot dS' = \int_{y_1}^{y_2} \int_{x_1}^{x_2} \frac{1}{\sqrt{x^2 + y^2 + z^2}} \cdot dx \cdot dy. \quad (\text{B.6})$$

We can define the indefinite integral  $I_1(x, y, z)$  as

$$I_1(x, y, z) = \int \frac{dy}{\sqrt{x^2 + y^2 + z^2}} = \ln \left( y + \sqrt{x^2 + y^2 + z^2} \right), \quad (\text{B.7})$$

and recast Equation B.6 in terms of Equation B.7 as

$$\int_{\Delta\partial\Sigma} G(\mathbf{p}, \mathbf{x}') \cdot dS' = \int_{x_1}^{x_2} (I_1(x, y_2, z) - I_1(x, y_1, z)) \cdot dx. \quad (\text{B.8})$$

By defining the indefinite integral  $I_2(x, y, z)$  as

$$\begin{aligned} I_2(x, y, z) &= \int \ln \left( y + \sqrt{x^2 + y^2 + z^2} \right) \cdot dx = \\ &= z \cdot \arctan \left( \frac{x}{\sqrt{x^2 + y^2 + z^2}} \right) - z \cdot \arctan \left( \frac{x \cdot y}{z \cdot \sqrt{x^2 + y^2 + z^2}} \right) - x + \\ &\quad + y \cdot \ln \left( x + \sqrt{x^2 + y^2 + z^2} \right) + x \cdot \ln \left( y + \sqrt{x^2 + y^2 + z^2} \right), \end{aligned} \quad (\text{B.9})$$

we arrive at our final equation:

$$\int_{\Delta\partial\Sigma} G(\mathbf{p}, \mathbf{x}') \cdot dS' = I_2(x_2, y_2, z) - I_2(x_2, y_1, z) - I_2(x_1, y_2, z) + I_2(x_1, y_1, z). \quad (\text{B.10})$$

## Section B.3: Neumann Boundary Condition

Using the same local parameters as in Section B.1, the integral equation for the Neumann boundary condition is given by

$$\int_{\Delta\partial\Sigma} \nabla G(\mathbf{p}, \mathbf{x}') \cdot dS' = \int_{y_1}^{y_2} dy \int_{x_1}^{x_2} dx \cdot \frac{x\hat{\mathbf{x}} + y\hat{\mathbf{y}} - z\hat{\mathbf{z}}}{(x^2 + y^2 + z^2)^{\frac{3}{2}}}. \quad (\text{B.11})$$

We begin by computing the  $x$ -component:

$$\begin{aligned}
\int_{\Delta\partial\Sigma} \hat{\mathbf{x}} \cdot \nabla G(\mathbf{p}, \mathbf{x}') \cdot dS' &= \int_{y_1}^{y_2} dy \int_{x_1}^{x_2} dx \cdot \frac{x}{(x^2 + y^2 + z^2)^{\frac{3}{2}}} = \\
&= \int_{y_1}^{y_2} \frac{dy}{\sqrt{x_1^2 + y^2 + z^2}} - \int_{y_1}^{y_2} \frac{dy}{\sqrt{x_2^2 + y^2 + z^2}} = \\
&= I_1(x_1, y_2, z) - I_1(x_1, y_1, z) - \\
&\quad - I_1(x_2, y_2, z) + I_1(x_2, y_1, z).
\end{aligned} \tag{B.12}$$

By the symmetry of the  $x$  and  $y$  dimensions in Equation B.11, we can immediately compute the  $y$ -component to be

$$\begin{aligned}
\int_{\Delta\partial\Sigma} \hat{\mathbf{y}} \cdot \nabla G(\mathbf{p}, \mathbf{x}') \cdot dS' &= I_1(y_1, x_2, z) - I_1(y_1, x_1, z) - \\
&\quad - I_1(y_2, x_2, z) + I_1(y_2, x_1, z).
\end{aligned} \tag{B.13}$$

Finally, the  $z$ -component evaluates to

$$\begin{aligned}
\int_{\Delta\partial\Sigma} \hat{\mathbf{z}} \cdot \nabla G(\mathbf{p}, \mathbf{x}') \cdot dS' &= \int_{y_1}^{y_2} dy \int_{x_1}^{x_2} dx \cdot \frac{-z}{(x^2 + y^2 + z^2)^{\frac{3}{2}}} = \\
&= \int_{y_1}^{y_2} dy \left( \frac{-z \cdot x}{(y^2 + z^2)\sqrt{x^2 + y^2 + z^2}} \Big|_{x_1}^{x_2} \right).
\end{aligned} \tag{B.14}$$

Dividing out by  $z$  to make the integral more soluble, we get

$$\begin{aligned}
&\int_{\Delta\partial\Sigma} \hat{\mathbf{z}} \cdot \nabla G(\mathbf{p}, \mathbf{x}') \cdot dS' = \\
&= -z \cdot \int_{u_1}^{u_2} du \cdot \left( \frac{z^2 \cdot x'}{z^3(u^2 + 1)\sqrt{u^2 + x'^2 + 1}} \Big|_{x'_1}^{x'_2} \right) = \\
&= - \int_{u_1}^{u_2} du \cdot \left( \frac{x'}{(u^2 + 1)\sqrt{u^2 + x'^2 + 1}} \Big|_{x'_1}^{x'_2} \right) = \\
&= \int_{u_1}^{u_2} du \cdot \left( \frac{x'_2}{(u^2 + 1)\sqrt{u^2 + (x'_2)^2 + 1}} - \frac{x'_1}{(u^2 + 1)\sqrt{u^2 + (x'_1)^2 + 1}} \right) \\
&= x'_2 \cdot (I_7(x'_2, u_1) - I_7(x'_2, u_2)) - x'_1 \cdot (I_7(x'_1, u_1) - I_7(x'_1, u_2)),
\end{aligned} \tag{B.15}$$

where  $I_7(a, b)$  is defined in A.

## APPENDIX C: Pseudocode for Single-Element and Multi-Element Robin Hood

### Section C.1: Single-Element Robin Hood

---

**Algorithm 1:** Single-Element Robin Hood

---

```
Input:  $A \in \mathbb{R}^N \times \mathbb{R}^N$ ;  $\mathbf{x}, \mathbf{b} \in \mathbb{R}^N$ ;  $r_{tol} \in \mathbb{R}^+$ 
Output:  $\mathbf{x} \in \mathbb{R}^N$ 
Data:  $\mathbf{b}', \mathbf{r} \in \mathbb{R}^N$ ;  $m \in \mathbb{N}$ ;  $c \in \mathbb{R}$  //  $A\mathbf{x} = \mathbf{b}'$ ,  $\mathbf{b} - \mathbf{b}' = \mathbf{r}$ 
1 /* initialization */
2 for  $i = 0$  to  $N$  do
3    $x_i = b'_i = 0$ ;  $r_i = b_i$ ;
4 end
5  $m = 0$ ;
6 /* iteration loop */
7 while  $(r_m / \|\mathbf{b}\|_\infty) > r_{tol}$  do
8   /* compute correction */
9    $c = r_m / A_{mm}$ ;
10  /* update solution */
11   $x_m = x_m + c$ ;
12  /* update vector approximation */
13  for  $i = 0$  to  $N$  do
14     $b'_i = b'_i + A_{im} \cdot c$ ;
15  end
16  /* compute residual and identify maximum residual element */
17   $m = 0$ ;
18  for  $i = 0$  to  $N$  do
19     $r_i = b_i - b'_i$ ;
20    if  $|r_i| > |r_m|$  then
21       $m = i$ ;
22    end
23  end
24 end
```

---

### Section C.2: Multiple-Element Robin Hood

---

**Algorithm 2: Multiple-Element Robin Hood**


---

```

Input:  $A \in \mathbb{R}^N \times \mathbb{R}^N$ ;  $\mathbf{x}, \mathbf{b} \in \mathbb{R}^N$ ;  $r_{tol} \in \mathbb{R}^+$ ;  $D \in \mathbb{N}$ 
Output:  $\mathbf{x} \in \mathbb{R}^N$ 
Data:  $\mathbf{b}', \mathbf{r} \in \mathbb{R}^N$ ;  $m \in \mathbb{N}^D$ ;  $\mathbf{c} \in \mathbb{R}^D$ ;  $A' \in \mathbb{R}^D \times \mathbb{R}^D$ ,  $\mathbf{r}' \in \mathbb{R}^D$  //  $A\mathbf{x} = \mathbf{b}'$ ,  $\mathbf{b} - \mathbf{b}' = \mathbf{r}$ 
1 /* initialization */
2 for  $i = 0$  to  $N$  do
3   |  $x_i = b'_i = 0$ ;  $r_i = b_i$ ;
4 end
5 for  $i = 0$  to  $D$  do
6   |  $m_i = i$ ;  $r'_i = b_i$ ;
7 end
8 /* iteration loop */
9 while ( $\|\mathbf{r}'\|_\infty / \|\mathbf{b}\|_\infty > r_{tol}$ ) do
10  /* compute corrections */
11  for  $i = 0$  to  $D$  do
12    | for  $j = 0$  to  $D$  do
13      | |  $A'_{ij} = A_{m_i m_j}$ ;
14    | end
15  end
16   $\mathbf{c} = (A')^{-1} \mathbf{r}'$ ;
17  /* update solution */
18  for  $i = 0$  to  $D$  do
19    |  $x_{m_i} = x_{m_i} + c_i$ ;
20  end
21  /* update vector approximation */
22  for  $i = 0$  to  $N$  do
23    | for  $j = 0$  to  $D$  do
24      | |  $b'_i = b'_i + A_{im_j} \cdot c_j$ ;
25    | end
26  end
27  /* compute residual and identify maximum residual elements */
28  for  $i = 0$  to  $D$  do
29    |  $m_i = i$ ;
30  end
31  for  $i = D$  to  $N$  do
32    |  $r_i = b_i - b'_i$ ;
33    | for  $j = 0$  to  $D$  do
34      | | if  $|r_i| > |r_{m_j}|$  then
35        | | | for  $k = j + 1$  to  $D$  do
36          | | | | if  $|r_{m_j}| > |r_{m_k}|$  then
37            | | | | |  $m_k = m_j$ ;
38            | | | | | break;
39          | | | | end
40        | | | end
41        | | |  $m_j = i$ ;
42        | | | break;
43      | | end
44    | end
45  end
46  for  $i = 0$  to  $D$  do
47    |  $r'_i = r_{m_i}$ ;
48  end
49 end

```

---

## APPENDIX D: Numeric Integration of Scalar and Vector Fields

The following numerical integration technique was used to compute the error 2-norm of the electrostatic potential and fields in Chapter 4.

### Section D.1: Numeric Integration by Riemann Sum

We begin with a function  $f$  defined over a  $d$ -dimensional domain and with an  $r$ -dimensional range ( $f: \mathbb{R}^d \rightarrow \mathbb{R}^r$ ), and a  $d$ -dimensional hypercube  $C$  over which the integral is performed. We define  $\mathbf{a}, \mathbf{b} \in \mathbb{R}^d$  as the extrema of  $C$ , and  $I \in \mathbb{R}^r$  as the analytic result the integration of  $f$  over  $C$ :

$$I = \int_C f(\mathbf{x}) d\mathbf{x} = \int_{a_1}^{b_1} \int_{a_2}^{b_2} \cdots \int_{a_d}^{b_d} f(\mathbf{x}) d\mathbf{x}. \quad (\text{D.1})$$

To approximate this integral, we uniformly partition our region of integration  $C$  into  $n^d$  hypercubes with equal volume  $\Delta c = \frac{|C|}{n^d}$ , and define the center of each partition as

$$\mathbf{x}_{i_1 i_2 \dots i_d} = \sum_j^d \left( a_j + \frac{i_j - \frac{1}{2}}{n(b_j - a_j)} \right) \cdot \mathbf{e}_j, \quad (\text{D.2})$$

where  $i_j \in \{1, 2, \dots, n\}$  and  $\mathbf{e}_j$  represents the  $j$ -th canonical basis vector of our domain. We then define a function  $R(f, \mathbf{a}, \mathbf{b}, n)$ ,  $n \in \mathbb{N}$ , as the cell-centered Riemann sum approximation of Equation D.1:

$$R(f, \mathbf{a}, \mathbf{b}, n) = \sum_{i_1}^n \sum_{i_2}^n \cdots \sum_{i_d}^n f(\mathbf{x}_{i_1 i_2 \dots i_d}) \Delta c, \quad (\text{D.3})$$

and we define  $I_n \equiv R(f, \mathbf{a}, \mathbf{b}, n)$ ,  $I_n \in \mathbb{R}^r$ , as the result of our integral approximation.

### Section D.2: Error Estimates

Using Richardson extrapolation, we can obtain an error estimate for  $I_n$  when  $n = 2^k$ ,  $k \in \mathbb{N}$  and  $k > 1$ . The following explanation assumes  $r = 1$ , but can easily be extended to higher dimensions of the range. We begin with the assumption that the error of  $I_n$  scales with some power of  $n$ :

$$E_n \equiv (I - I_n) \approx c_1 \cdot n^{c_2}, \quad (\text{D.4})$$



where  $c_1$  and  $c_2$  are unknown constants. We then compare successive terms of  $E_n$ :

$$\begin{aligned}
 E_n &= I - I_n \approx c_1 \cdot n^{c_2}, \\
 E_{\frac{n}{2}} &= I - I_{\frac{n}{2}} \approx c_1 \cdot \left(\frac{1}{2}\right)^{c_2} \cdot n^{c_2} \\
 E_{\frac{n}{4}} &= I - I_{\frac{n}{4}} \approx c_1 \cdot \left(\frac{1}{4}\right)^{c_2} \cdot n^{c_2}.
 \end{aligned}
 \tag{D.5}$$

These equations can be simultaneously solved for an approximation of  $I$  as

$$I \approx \frac{I_n I_{\frac{n}{4}} - \left(I_{\frac{n}{2}}\right)^2}{I_n - 2I_{\frac{n}{2}} + I_{\frac{n}{4}}},
 \tag{D.6}$$

which can be used to provide a numerical estimate for  $E_n$ :

$$E_n \approx \frac{I_n I_{\frac{n}{4}} - \left(I_{\frac{n}{2}}\right)^2}{I_n - 2I_{\frac{n}{2}} + I_{\frac{n}{4}}} - I_n.
 \tag{D.7}$$

Using this estimate, we can construct a function  $E(f, \mathbf{a}, \mathbf{b}, n)$  that returns  $E_n$ .

### Section D.3: Adaptive Integration

Now that we have the functions  $R(f, \mathbf{a}, \mathbf{b}, n)$  and  $E(f, \mathbf{a}, \mathbf{b}, n)$  to compute the numeric integral and approximate error of Equation D.1, respectively, we can construct an adaptive integrator that successively partitions  $C$  to acquire a numerical estimate of  $I$  while avoiding excessive field sampling in regions of the domain where  $f$  is well behaved. Pseudocode for this algorithm is provided in Algorithm 3, with the additional terms  $I_m$  and  $E_{tol}$  as a metric and relative accuracy tolerance, respectively.

---

#### Algorithm 3: AdaptiveIntegral( $f, \mathbf{a}, \mathbf{b}, n, I_m, E_{tol}$ )

---

```

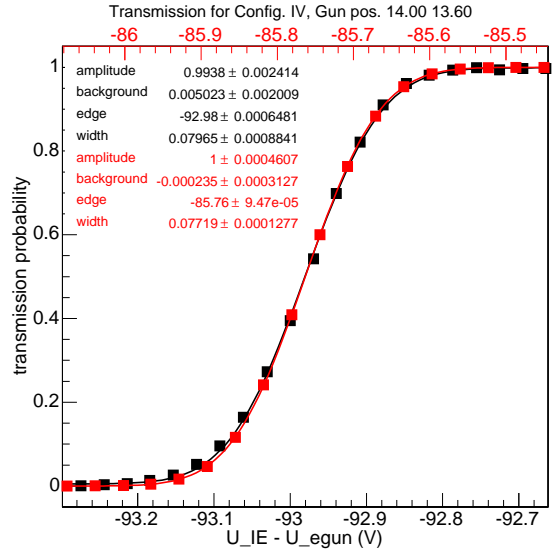
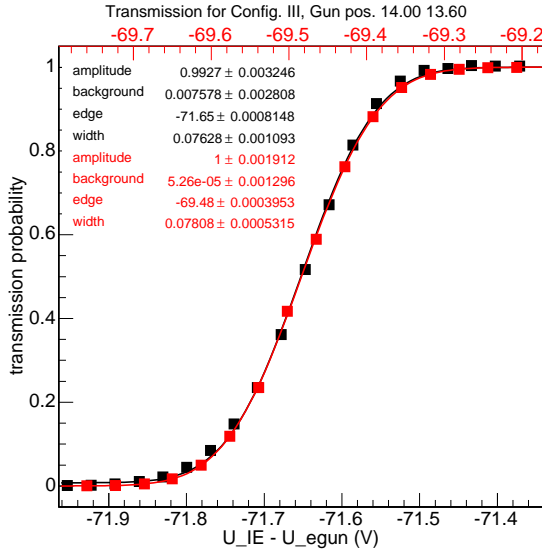
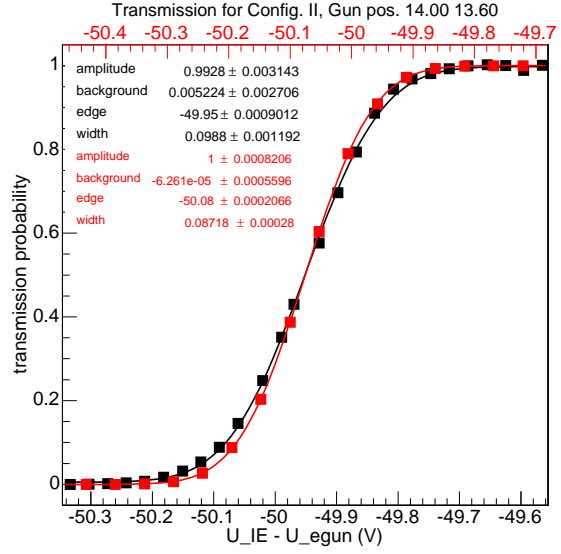
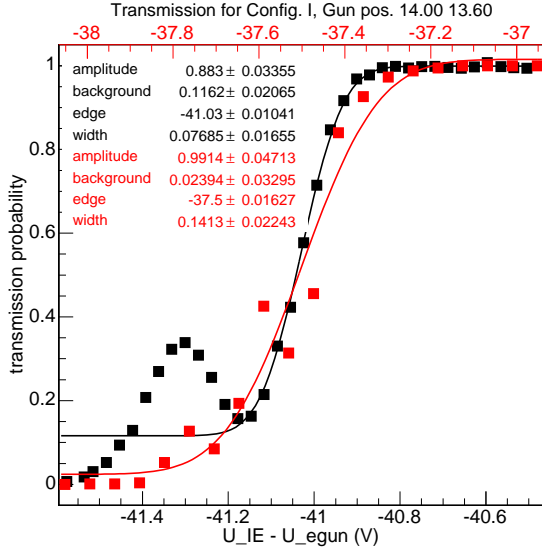
Input:  $f : \mathbb{R}^d \rightarrow \mathbb{R}^r$ ;  $a, b \in \mathbb{R}^d$ ;  $n \in \mathbb{N} > 1$ ;  $I_m \in \mathbb{R}^r$ ;  $E_{tol} \in \mathbb{R}^+$ 
Output:  $I \in \mathbb{R}^r$ 
Data:  $E_1, E_2 \in \mathbb{R}^r$ 
1  $I = R(f, a, b, n)$ ;
2  $E_1 = E(f, a, b, n)$ ;
3  $E_2 = E(f, a, b, \frac{n}{2})$ ;
4 if  $|E_2 - E_1| > |I_m| \cdot E_{tol}$  then
5    $I = 0$ ;
6   Subdivide Domain into  $2^d$  domains via bifurcation in each dimension  $d$ ;
7   for  $i = 0$  to  $2^d$  do
8      $I = I + \text{AdaptiveIntegral}(f, \mathbf{a}_i, \mathbf{b}_i, n, I_m, E_{tol})$ ;
9   end
10 end
11 return  $I$ ;

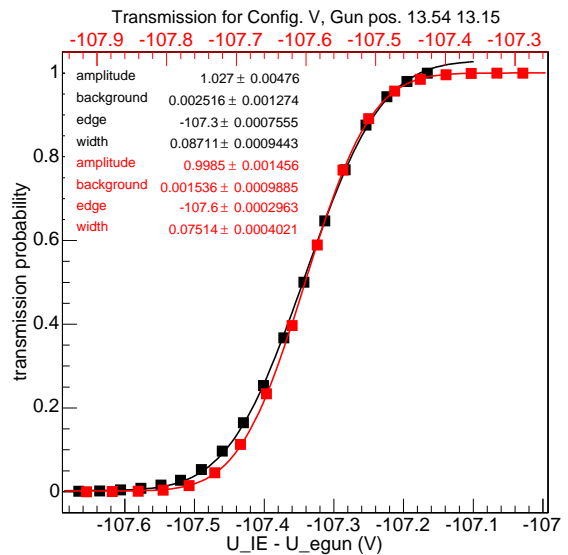
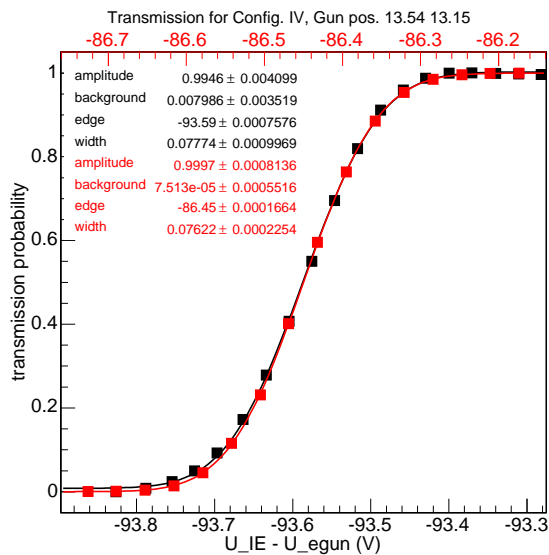
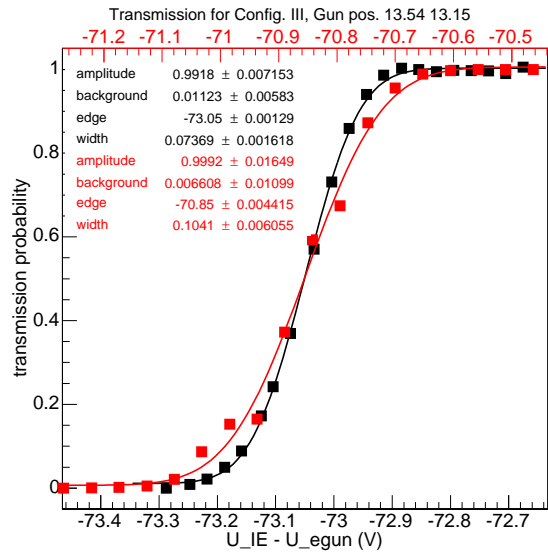
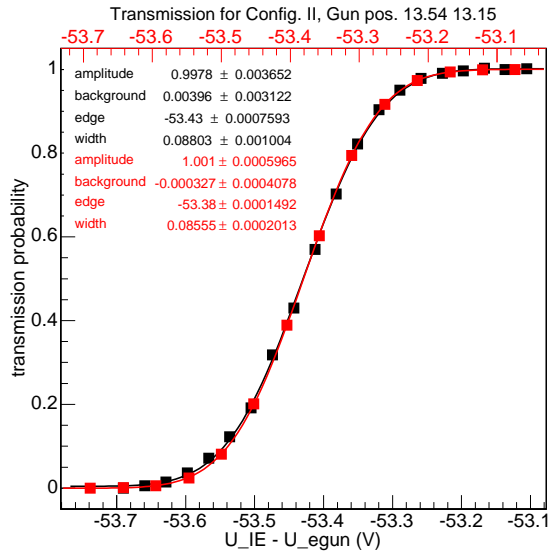
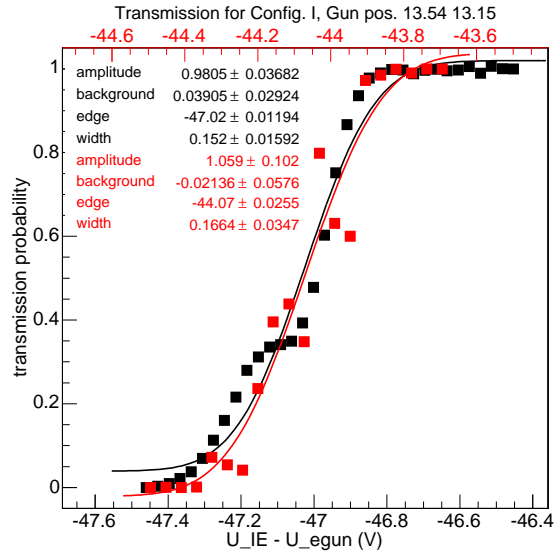
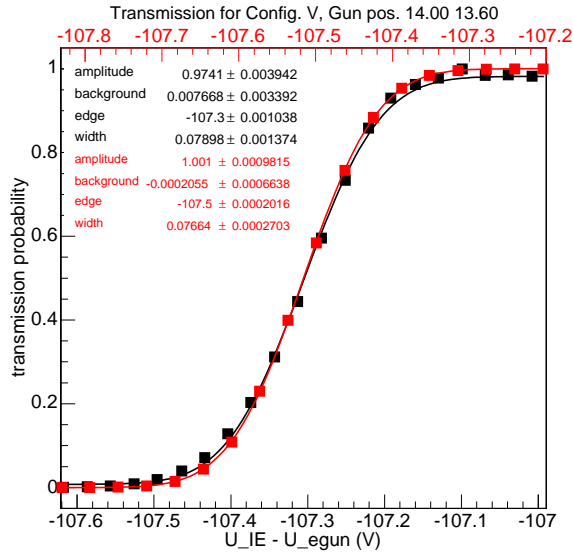
```

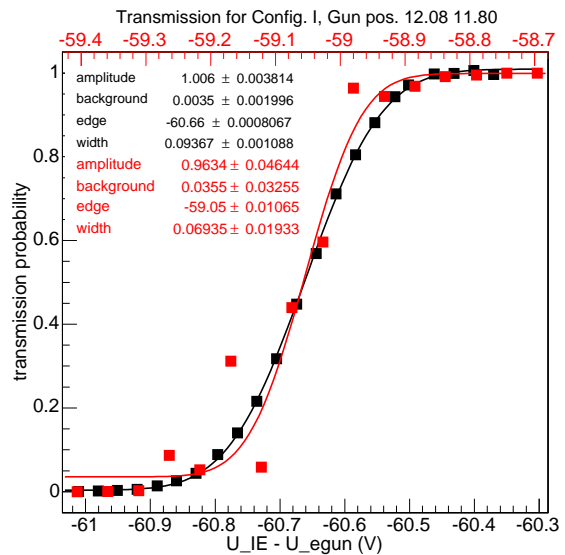
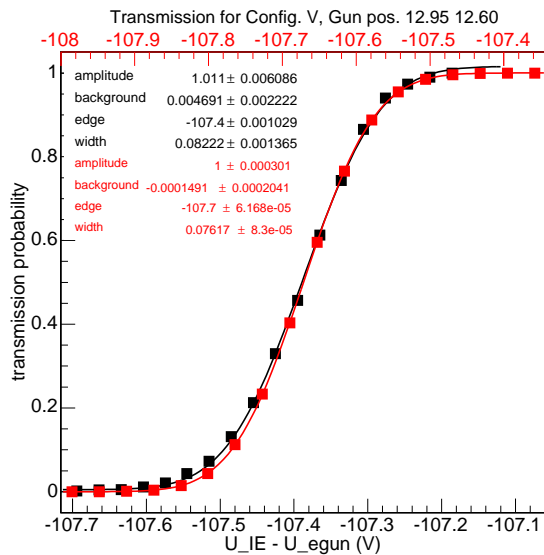
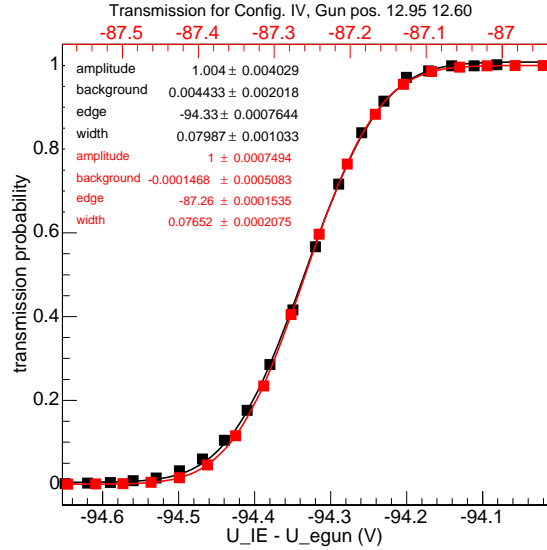
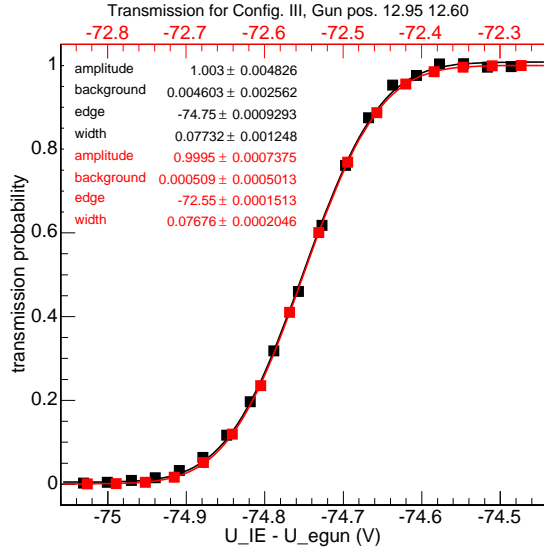
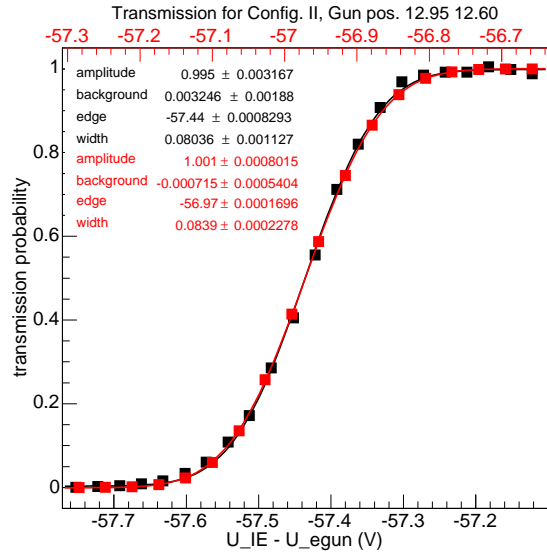
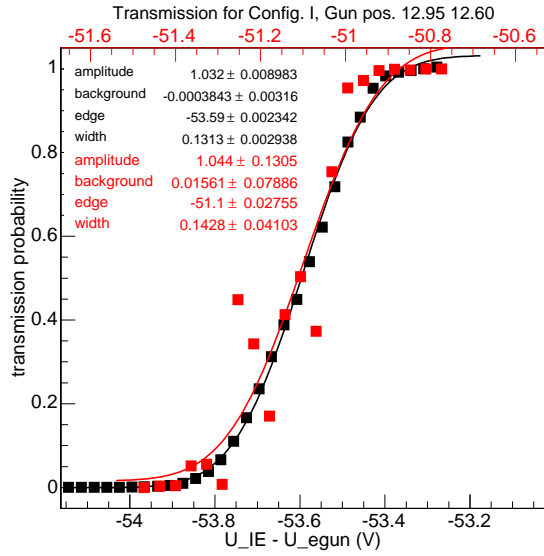
---

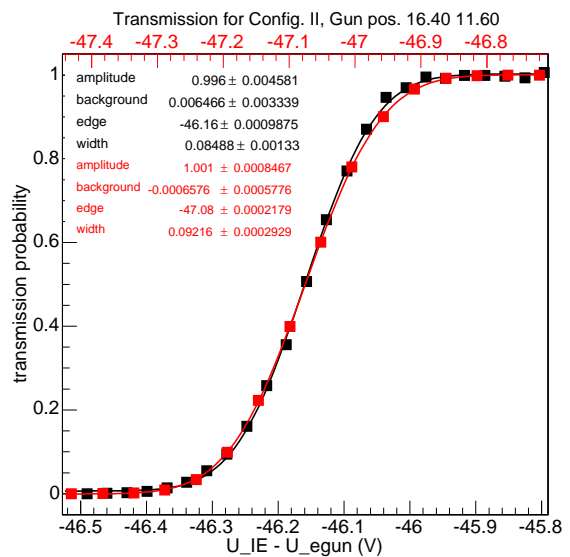
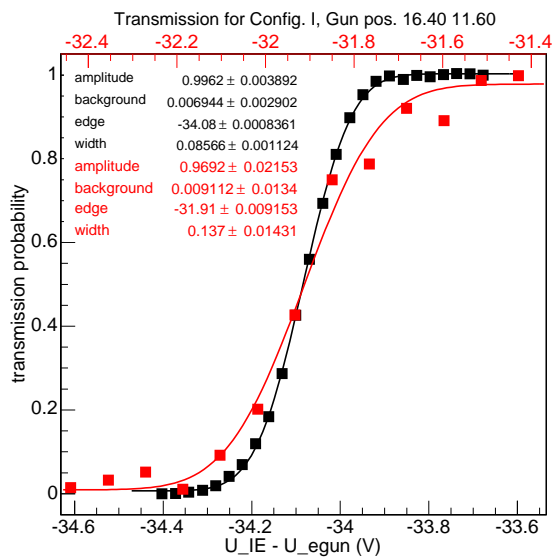
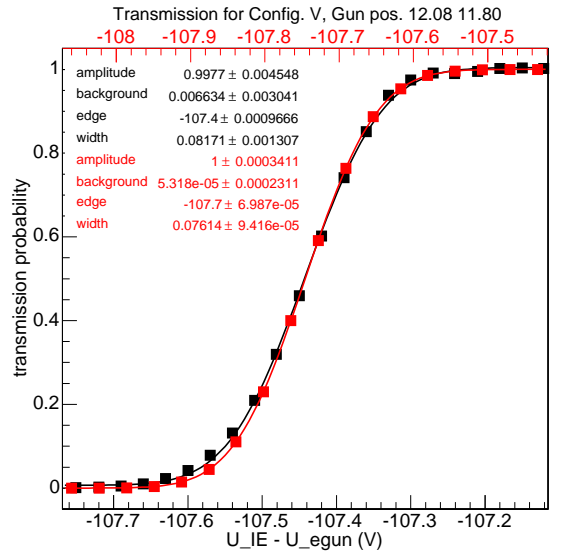
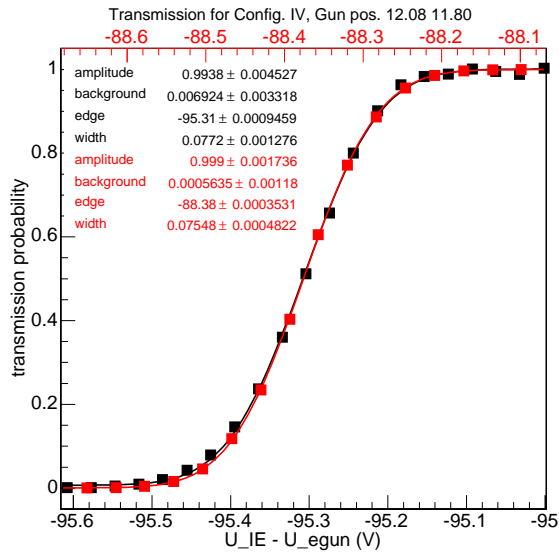
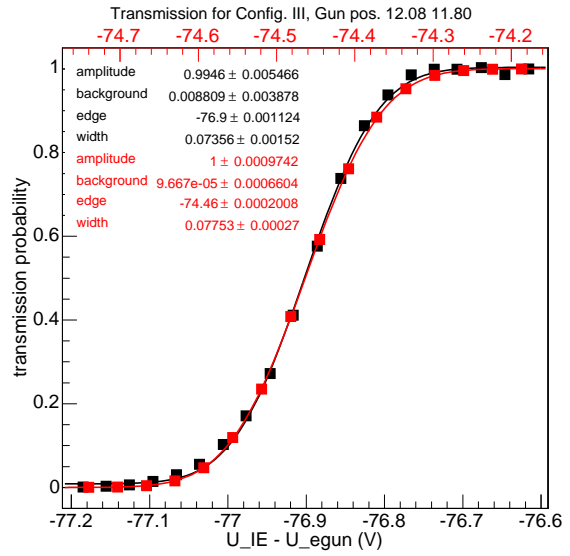
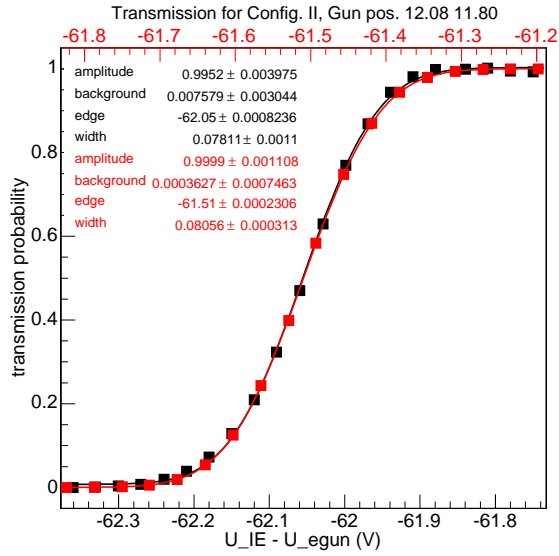
## APPENDIX E: Measured and simulated transmission function plots

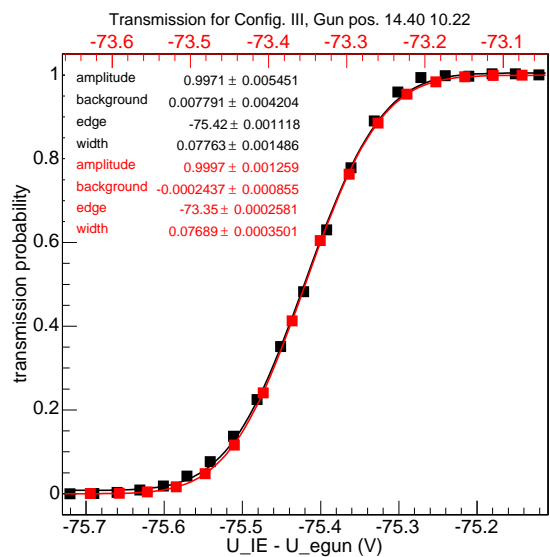
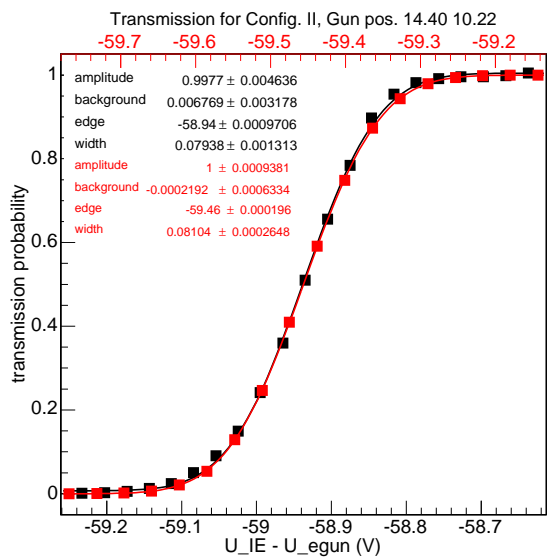
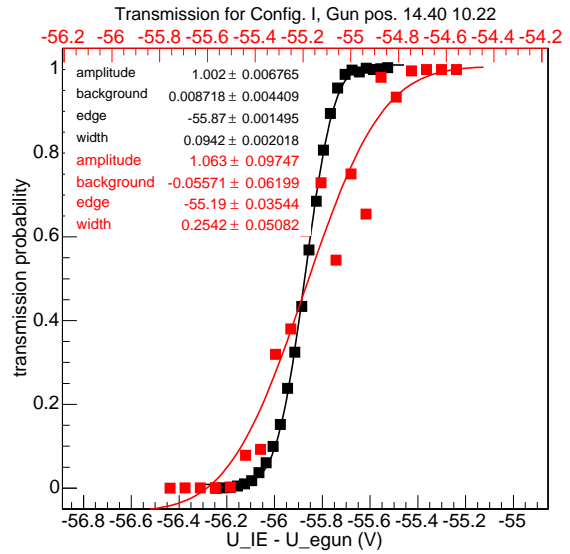
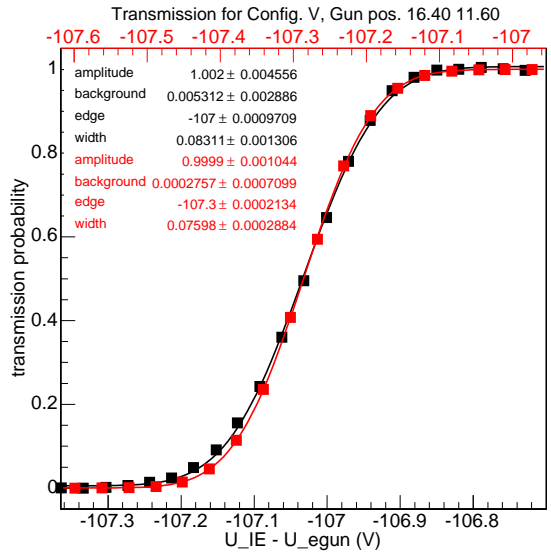
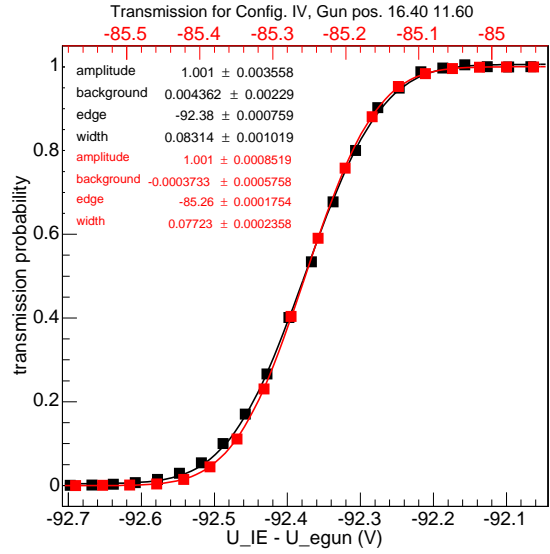
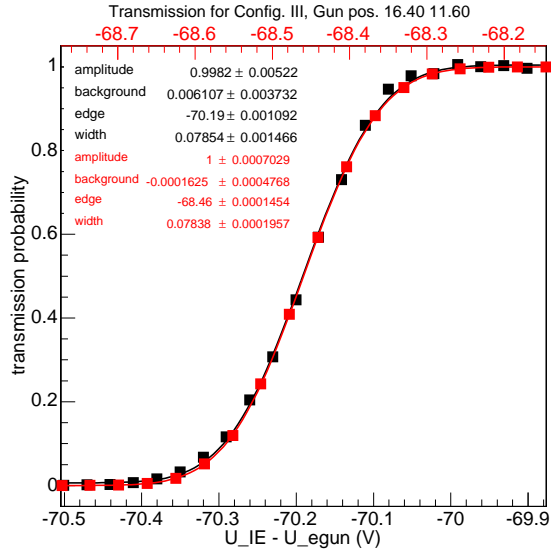
The following plots depict the measured (black) and simulated (red) transmission functions and their associated parameters from fitting to Equation 6.40. For the simulated transmission function points, the position of the electron gun was first corrected to minimize the edge offsets for the ring 12 and ring 13 measurements.

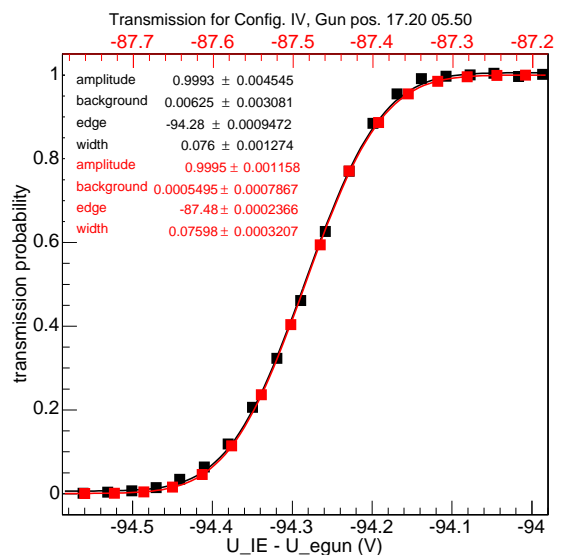
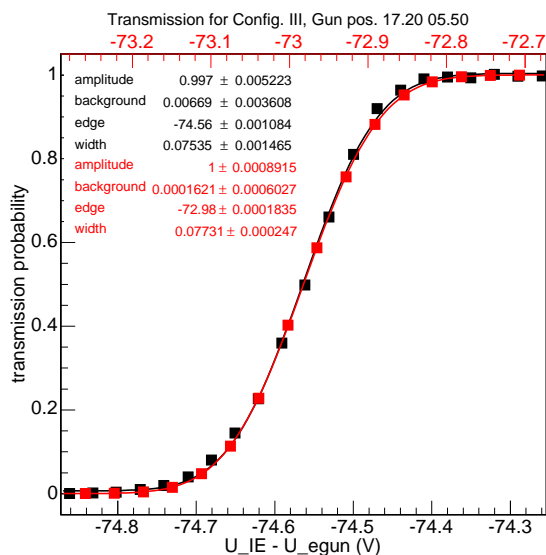
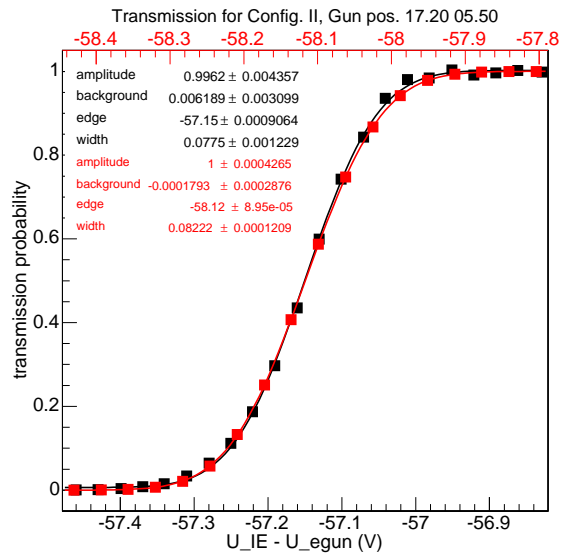
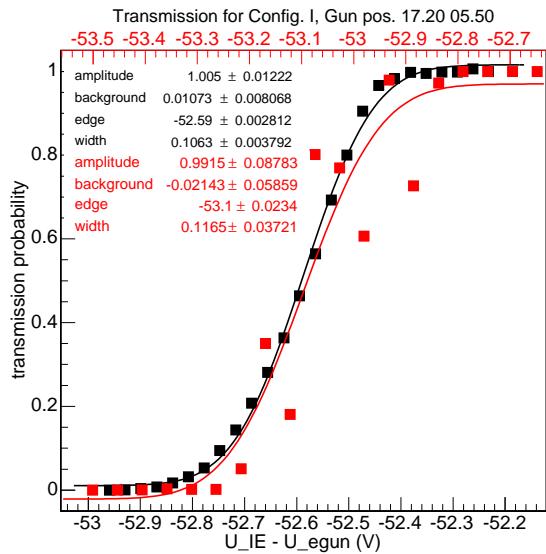
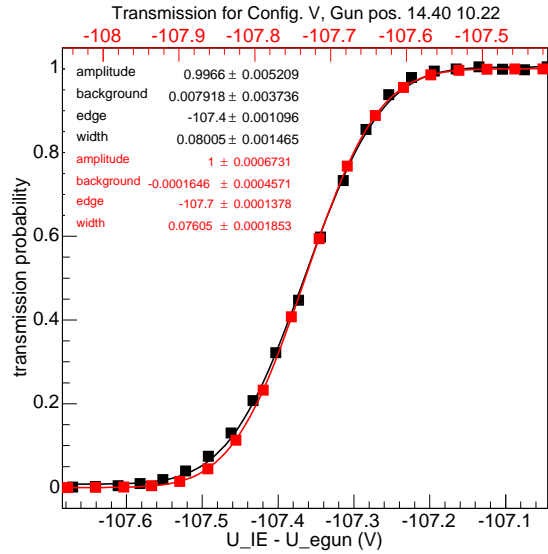
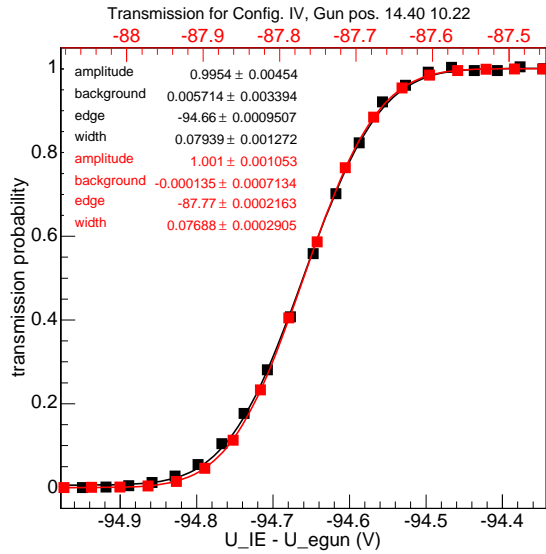


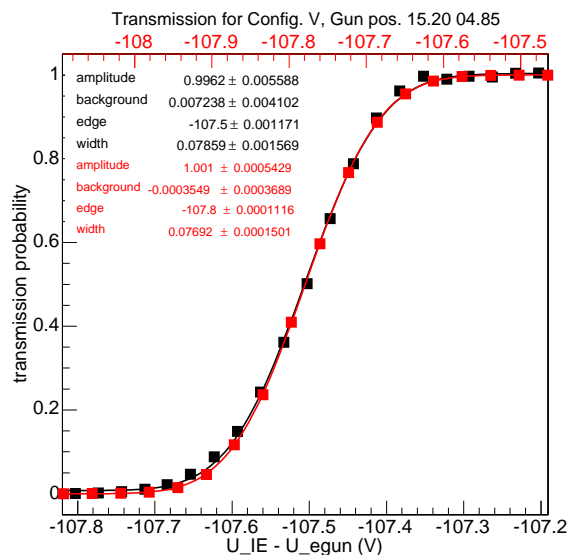
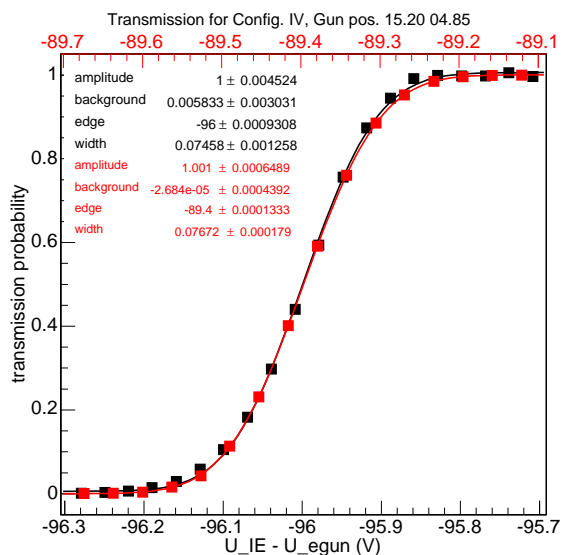
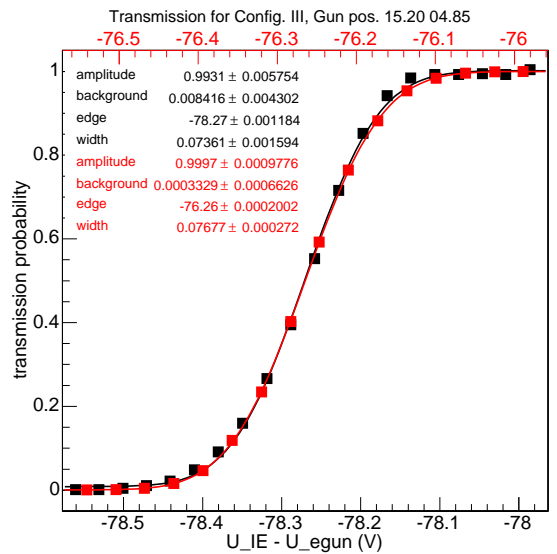
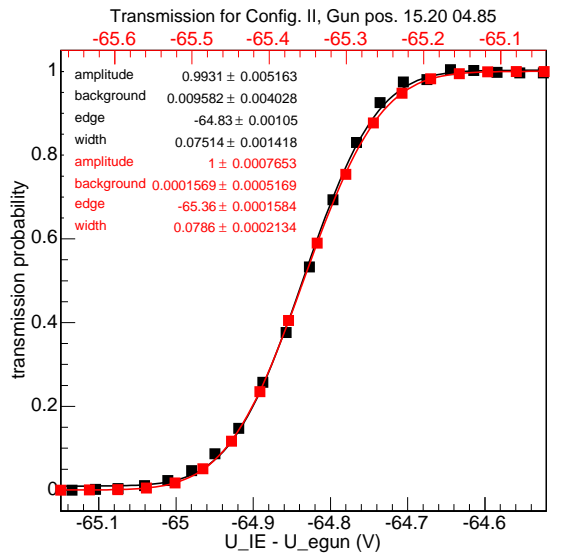
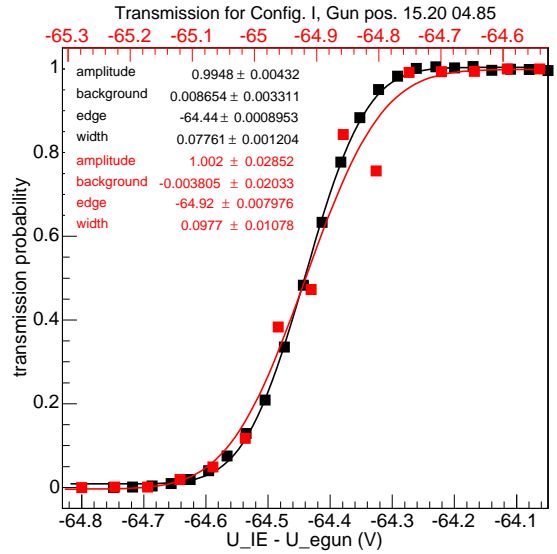
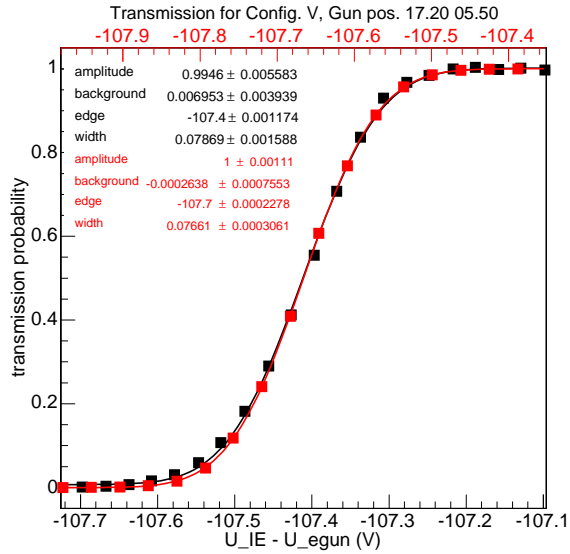














## REFERENCES

- [1] F Capozzi, G L Fogli, E Lisi, A Marrone, D Montanino, and A Palazzo. Status of three-neutrino oscillation parameters, circa 2013. *arXiv.org*, December 2013, 1312.2878v2.
- [2] J Angrik, T Armbrust, A Beglarian, U Besserer, J BLÜMER, J Bonn, R Carr, B Bornschein, L Bornschein, T BURRITT, M CHARLTON, A J DAVIES, C DAY, P J DOE, L DÖRR, O DRAGON, G Drexlin, F EICHELHARDT, K EITEL, K ESSIG, A FELDEN, B FLATT, J Formaggio, B FREUDIGER, R GEHRING, H GEMMEKE, E GERASKIN, F Gluck, M GLUGLA, S GROHMANN, R GUMBSHEIMER, F HABERMEHL, G HARPER, G HELLRIEGEL, J HERBERT, T HÖHN, M HOWE, H HUCKER, O V IVANOV, K P JÜNGST, J KASPAR, O KAZACHENKO, N KERNERT, P KOMAREK, A KOVALIK, C KRAUS, H KRAUSE, M LEBER, R LEWIS, V LOBASHEV, X LUO, K MAIER, O MALYSHEV, M MARK, I MESHKOV, K Muller, S MUTTERER, G R MYNENI, M NEUBERGER, and H NEUMANN. KATRIN Design Report 2004, 2005.
- [3] Ch Weinheimer. KATRIN, a next generation tritium  $\beta$  decay experiment in search for the absolute neutrino mass scale. *Progress in Particle and Nuclear Physics*, 48(1):141–150, January 2002.
- [4] J F Amsbaugh, J Barrett, A Beglarian, T Bergmann, H Bichsel, and others. Focal-plane detector system for the KATRIN experiment. *arXiv*, physics.ins-det, 2014.
- [5] K Valerius. The wire electrode system for the KATRIN main spectrometer. *Progress in Particle and Nuclear Physics*, 64(2):291–293, April 2010.
- [6] Ferenc Glück, Guido Drexlin, Benjamin Leiber, Susanne Mertens, Alexander Osipowicz, Jan Reich, and Nancy Wandkowsky. Electromagnetic design of the large-volume air coil system of the KATRIN experiment. *New Journal of Physics*, 15(8):083025, August 2013.
- [7] V Hannen, HW Ortjohann, M Zacher, and C Weinheimer. Electrical short circuits in the main spectrometer wire electrode. *KATRIN Internal Document*, pages 1–22, March 2013.
- [8] J D Behrens, T J Corona, Ferenc Glück, S Groh, N Steinbrink, N Wandkowsky, and C Weinheimer. EMD consequences of electrical shorts at the inner electrode system. *KATRIN Internal Document*, pages 1–72, March 2013.
- [9] M Juretzko. Studie zur geometrischen Vermessung der Modul- Befestigungsbolzen des KATRIN-Spektrometertanks. *KATRIN Internal Document*, pages 1–42, August 2008.
- [10] V Hannen, J D Behrens, S Groh, R Jöhren, N Steinbrink, C Weinheimer, M Zacher, and Miroslav Zboril. M3 Report - E-gun Characteristics. *KATRIN Internal Document*, pages 1–16, October 2013.
- [11] R N Cahn, D A Dwyer, S J Freedman, W C Haxton, R W Kadel, Yu G Kolomensky, K-B Luk, P McDonald, G D Orebi Gann, and A W P Poon. White Paper: Measuring the Neutrino Mass Hierarchy. *arXiv.org*, July 2013, 1307.5487.
- [12] Ziro Maki, Masami Nakagawa, and Shoichi Sakata. Remarks on the Unified Model of Elementary Particles. *Progress of Theoretical Physics*, 28(5):870–880, November 1962.
- [13] S Eidelman, K G Hayes, K A Olive, and M Aguilar-Benitez. Review of particle physics. *Physics Letters B*, 2004.
- [14] Planck Collaboration, P A R Ade, N Aghanim, C Armitage-Caplan, M Arnaud, M Ashdown, F Atri-Barandela, J Aumont, C Baccigalupi, A J Banday, R B Barreiro, J G Bartlett, E Battaner, K Benabed, A Benoît, A Benoit-Lévy, J P Bernard, M Bersanelli, P Bielewicz, J Bobin, J J Bock, A Bonaldi, J R Bond, J Borrill, F R Bouchet, M Bridges, M Bucher, C Burigana, R C Butler, E Calabrese,

B Cappellini, J F Cardoso, A Catalano, A Challinor, A Chamballu, R R Chary, X Chen, H C Chiang, L Y Chiang, P R Christensen, S Church, D L Clements, S Colombi, Colombo, L. P. L., F Couchot, A Coulais, B P Crill, A Curto, F Cuttaia, L Danese, R D Davies, R J Davis, P de Bernardis, A de Rosa, G de Zotti, J Delabrouille, J M Delouis, F X Désert, C Dickinson, J M Diego, K Dolag, H Dole, S Donzelli, O Doré, M Douspis, J Dunkley, X Dupac, G Efstathiou, F Elsner, T A Enßlin, H K Eriksen, F Finelli, O Forni, M Frailis, A A Fraisse, E Franceschi, T C Gaier, S Galeotta, S Galli, K Ganga, M Giard, G Giardino, Y Giraud-Héraud, E Gjerløw, J González-Nuevo, K M Górski, S Gratton, A Gregorio, A Gruppuso, J E Gudmundsson, J Haissinski, J Hamann, F K Hansen, D Hanson, D Harrison, S Henrot-Versillé, C Hernández-Monteagudo, D Herranz, S R Hildebrandt, E Hivon, M Hobson, W A Holmes, A Hornstrup, Z Hou, W Hovest, K M Huffenberger, A H Jaffe, T R Jaffe, J Jewell, W C Jones, M Juvela, E Keihänen, R Kesitalo, T S Kisner, R Kneissl, J Knoche, L Knox, M Kunz, H Kurki-Suonio, G Lagache, A Lähteenmäki, J M Lamarre, A Lasenby, M Lattanzi, R J Laureijs, C R Lawrence, S Leach, J P Leahy, R Leonardi, J León-Tavares, J Lesgourgues, A Lewis, M Liguori, P B Lilje, M Linden-Vørnle, M López-Cañiego, P M Lubin, J F Macías-Pérez, B Maffei, D Maino, N Mandolesi, M Maris, D J Marshall, P G Martin, E Martínez-González, S Masi, M Massardi, S Matarrese, F Matthai, P Mazzotta, P R Meinhold, A Melchiorri, J B Melin, L Mendes, E Menegoni, A Mennella, M Migliaccio, M Millea, S Mitra, M A Miville-Deschênes, A Moneti, L Montier, G Morgante, D Mortlock, A Moss, D Munshi, J A Murphy, P Naselsky, F Nati, P Natoli, C B Netterfield, H U Nørgaard-Nielsen, F Noviello, D Novikov, I Novikov, I J O'Dwyer, S Osborne, C A Oxborrow, F Paci, L Pagano, F Pajot, D Paoletti, B Partridge, F Pasian, G Patanchon, D Pearson, T J Pearson, H V Peiris, O Perdureau, L Perotto, F Perrotta, V Pettorino, F Piacentini, M Piat, E Pierpaoli, D Pietrobon, S Plaszczynski, P Platania, E Pointecouteau, G Polenta, N Ponthieu, L Popa, T Poutanen, G W Pratt, G Prézeau, S Prunet, J L Puget, J P Rachen, W T Reach, R Rebolo, M Reinecke, M Remazeilles, C Renault, S Ricciardi, T Riller, I Ristorcelli, G Rocha, C Rosset, G Roudier, M Rowan-Robinson, J A Rubiño-Martín, B Rusholme, M Sandri, D Santos, M Savelainen, G Savini, D Scott, M D Seiffert, E P S Shellard, L D Spencer, J L Starck, V Stolyarov, R Stompor, R Sudiwala, R Sunyaev, F Sureau, D Sutton, A S Suur-Uski, J F Sygnet, J A Tauber, D Tavagnacco, L Terenzi, L Toffolatti, M Tomasi, M Tristram, M Tucci, J Tuovinen, M Türler, G Umata, L Valenziano, J Valiviita, B Van Tent, P Vielva, F Villa, N Vittorio, L A Wade, B D Wandelt, I K Wehus, M White, S D M White, A Wilkinson, D Yvon, A Zacchei, and A Zonca. Planck 2013 results. XVI. Cosmological parameters. *arXiv.org*, March 2013, 1303.5076.

- [15] M Auger, D J Auty, P S Barbeau, E Beauchamp, V Belov, C Benitez-Medina, M Breidenbach, T Brunner, A Burenkov, B Cleveland, S Cook, T Daniels, M Danilov, C G Davis, S Delaquis, R deVoe, A Dobi, M J Dolinski, A Dolgolenko, M Dunford, W Fairbank, J Farine, W Feldmeier, P Fierlinger, D Franco, G Giroux, R Gornea, K Graham, G Gratta, C Hall, K Hall, C Hargrove, S Herrin, M Hughes, A Johnson, T N Johnson, A Karelin, L J Kaufman, A Kuchenkov, K S Kumar, D S Leonard, F Leonard, D Mackay, R MacLellan, M Marino, B Mong, M Montero Díez, A R Müller, R Neilson, R Nelson, A Odian, I Ostrovskiy, K O'Sullivan, C Ouellet, A Piepke, A Pocar, C Y Prescott, K Pushkin, P C Rowson, J J Russell, A Sabourov, D Sinclair, S Slutsky, V Stekhanov, T Tolba, D Tosi, K Twelker, P Vogel, J L Vuilleumier, A Waite, T Walton, M Weber, U Wichoski, J Wodin, J D Wright, L Yang, Y R Yen, O Ya Zeldovich, and EXO Collaboration. Search for Neutrinoless Double-Beta Decay in  $^{136}\text{Xe}$  with EXO-200. *Physical Review Letters*, 109(3):032505, July 2012.
- [16] Ch Kraus, B Bornschein, L Bornschein, J Bonn, B FLATT, A KOVALIK, B Ostrick, E W Otten, J P Schall, and Th Thümmler. Final results from phase II of the Mainz neutrino mass search in tritium decay. *The European Physical Journal C-Particles and Fields*, 40(4):447–468, 2005.
- [17] V N Aseev, A I Belev, A I Berlev, E V Geraskin, A A Golubev, N A Lihovid, V M Lobashev, A A Nozik, V S Pantuev, V I Parfenov, A K Skasyrskaya, F V Tkachov, and S V Zadorozhny. Measurement of the electron antineutrino mass in tritium beta decay in the Troitsk nu-mass experiment. *Physics of Atomic Nuclei*, 75(4):464–478, 2012.
- [18] Carlo Giunti and Chung W Kim. *Fundamentals of Neutrino Physics and Astrophysics*. Oxford University

Press, March 2007.

- [19] K Zuber. *Neutrino physics*. High energy physics, cosmology and gravitation. IOP, Bristol, 2004.
- [20] G Beamson, H Q Porter, and D W Turner. The collimating and magnifying properties of a superconducting field photoelectron spectrometer. *J. Phys. E: Sci. Instrum.*, 13(1):64–66, January 1980.
- [21] V M Lobashev and P E Spivak. A method for measuring the electron antineutrino rest mass. *Nuclear Instruments and Methods in Physics Research Section A: Accelerators, Spectrometers, Detectors and Associated Equipment*, 240(2):305–310, October 1985.
- [22] A Picard, H Backe, H Barth, J Bonn, and B Degen. A solenoid retarding spectrometer with high resolution and transmission for keV electrons. *Nuclear Instruments and Methods in Physics Research*, B63:345–358, 1992.
- [23] Guido Drexlin. KATRIN - direct measurement of a sub-eV neutrino mass. *Nuclear Physics B - Proceedings Supplements*, 145:263–267, August 2005.
- [24] Jostein R Kristiansen and Øystein Elgarøy. Cosmological implications of the KATRIN experiment. *Journal of Cosmology and Astroparticle Physics*, 2008(01):007, 2008.
- [25] Miklós Szilágyi. *Electron and ion optics*. Plenum Pub Corp, 1988.
- [26] Dragan Poljak and C A Brebbia. *Boundary Element Methods for Electrical Engineers*. WIT Press, January 2005.
- [27] Ram P Kanwal. *Linear Integral Equations*. Theory & Technique. Springer Science & Business Media, November 2012.
- [28] D J Cartwright. *Underlying Principles of the Boundary Element Method*. Computational Mechanics, 2001.
- [29] Lothar Gaul, Martin Kögl, and Marcus Wagner. *Boundary Element Methods for Engineers and Scientists*. Springer, April 2003.
- [30] C A Brebbia and Stephen Walker. *Boundary element techniques in engineering*. Butterworth-Heinemann, 1980.
- [31] C A Brebbia and R Butterfield. Formal equivalence of direct and indirect boundary element methods. *Applied Mathematical Modelling*, 2(2):132–134, 1978.
- [32] Alok Sutradhar, Glaucio H Paulino, and Leonard J Gray. *Symmetric Galerkin Boundary Element Method*. Springer Science & Business Media, September 2008.
- [33] Alexander H D Cheng and Daisy T Cheng. Heritage and early history of the boundary element method. *Engineering Analysis with Boundary Elements*, 29(3):268–302, March 2005.
- [34] Randall J LeVeque. *Finite Volume Methods for Hyperbolic Problems*. Cambridge University Press, August 2002.
- [35] Predrag Lazic, Denis Dujmić, Joseph A Formaggio, Hrvoje Abraham, and H Stefancic. New approach to 3D electrostatic calculations for micro-pattern detectors. *Journal of Instrumentation*, 6(12):P12003, 2011.
- [36] Joseph A Formaggio, Predrag Lazic, T J Corona, Hrvoje Stefancic, Hrvoje Abraham, and Ferenc Glück. Solving for micro-and macro-scale electrostatic configurations using the Robin Hood algorithm. *Progress in Electromagnetics Research B*, 39:1–37, 2012.

- [37] Jinchao Xu. Iterative Methods by Space Decomposition and Subspace Correction. *SIAM Review*, 34(4):581–613, December 1992.
- [38] William L Briggs, Van Emden Henson, and Steve F McCormick. *A Multigrid Tutorial*. Second Edition. SIAM, July 2000.
- [39] James W Demmel. *Applied Numerical Linear Algebra*. SIAM, August 1997.
- [40] C Geuzaine and J F Remacle. Gmsh: A 3 - D finite element mesh generator with built - in pre - and post - processing facilities. *International Journal for Numerical Methods in Engineering*, 2009.
- [41] Andrei Alexandrescu. *Modern C++ Design*. Generic Programming and Design Patterns Applied. Addison-Wesley Professional, 2001.
- [42] S Balay, W D Gropp, L C McInnes, and B F Smith. PETSc 2.0 users manual. 1996.
- [43] Ferenc Glück. AXISYMMETRIC ELECTRIC FIELD CALCULATION WITH ZONAL HARMONIC EXPANSION. *Progress in Electromagnetics Research B*, 32:319–350, July 2011.
- [44] John P Barrett, Joseph A Formaggio, and Thomas J Corona. The Spherical Multipole Expansion of a Triangle. *arXiv.org*, March 2014, 1403.5362v1.
- [45] Ferenc Glück and F Gluck. AXISYMMETRIC MAGNETIC FIELD CALCULATION WITH ZONAL HARMONIC EXPANSION. *Progress in Electromagnetics Research B*, 32:351–388, July 2011.
- [46] Nicolai M Josuttis. *The C++ standard library: a tutorial and reference; 2nd ed*. Addison-Wesley, Upper Saddle River, NJ, 2012.
- [47] D W Walker and J J Dongarra. MPI: a standard message passing interface. *Supercomputer*, 1996.
- [48] J E Stone, D Gohara, and G Shi. OpenCL: A parallel programming standard for heterogeneous computing systems. *Computing in science & engineering*, 2010.
- [49] Will Schroeder, Kenneth William Martin, and Bill Lorensen. *The Visualization Toolkit*. An Object-oriented Approach to 3D Graphics. Pearson P T R, January 1996.
- [50] Amy Henderson Squillacote. *The ParaView Guide*. Kitware Inc., 2007.
- [51] I Antcheva, M Ballintijn, B Bellenot, M Biskup, R Brun, and others. ROOT: A C++ framework for petabyte data storage, statistical analysis and visualization. *Computer Physics Communications*, 180(12):2499–2512, 2009.
- [52] Chi-Ok Hwang. Electrical capacitance of the unit cube. *Journal of Applied Physics*, 95(7):3798, 2004.
- [53] Andreas Fabri and Sylvain Pion. CGAL: the Computational Geometry Algorithms Library. *GIS*, pages 538–539, 2009.
- [54] F Gluck. The Penning discharge. *KATRIN Internal Document*, pages 1–20, March 2007.
- [55] Andrew Mustun. *dxflib*. Programmer’s Guide. RibbonSoft, Inc., March 2005.
- [56] N Stallkamp. Optimierung und erste Messung der Transmissionseigenschaften des KATRIN-Hauptspektrometers. *Diplomarbeit ; Karlsruhe Institute of Technology*, pages 1–119, September 2013.
- [57] Ferenc Glück. Runge-Kutta method for numerical solution of differential equation system. *KATRIN Internal Document*, pages 1–3, July 2007.

- [58] A B Birtles, B J Mayo, and A W Bennett. Computer technique for solving 3-dimensional electron-optics and capacitance problems. *Proceedings of the Institution of Electrical Engineers*, 120(2):213–220, 1973.
- [59] R G Hudson and J Lipka. *A table of integrals*. John Wiley & Sons, Boston, 1917.
- [60] F Bowman and F A Gerard. *Higher calculus*. Cambridge University Press, 1967.